DISSERTATION

CLUSTERING OF NON-CONDUCTING KV2.1 CHANNELS INDUCES ENDOPLASMIC RETICULUM/PLASMA MEMBRANE JUNCTIONS AND FORMS CELL-SURFACE TRAFFICKING HUBS

Submitted by

Philip Douglas Fox

Graduate Degree Program in Cell and Molecular Biology

In partial fulfillment of the requirements

For the Degree of Doctor of Philosophy

Colorado State University

Fort Collins, Colorado

Fall 2014

Doctoral Committee:

Advisor: Michael M. Tamkun

Gregory C. Amberg
Jozsef Vigh
Susan Tsunoda
Deborah M. Garrity

ABSTRACT

CLUSTERING OF NON-CONDUCTING KV2.1 CHANNELS INDUCES ENDOPLASMIC RETICULUM/PLASMA MEMBRANE JUNCTIONS AND FORMS CELL-SURFACE TRAFFICKING HUBS

The voltage-gated K^+ channel, Kv2.1, is expressed widely in the mammalian CNS, where it carries the majority of the delayed-rectifier current. The Kv2.1 current facilitates high-frequency action potential firing by promoting the repolarization of the membrane potential and subsequent recovery of voltage-gated Na^+ channels from inactivation. Furthermore, Kv2.1 displays a unique cell-surface localization to dense, micron-sized clusters which are sensitive to neuronal insults such as glutamate excitotoxicity. The following dissertation presents original research extending our knowledge of the Kv2.1 K^+ channel. The majority of Kv2.1 channels are held in a non-conducting state which is incapable of fluxing K^+ in response to membrane potential depolarization. These non-conducting channels tend to localize to the micron-sized clusters which distinguish Kv2.1. Non-conducting, clustered Kv2.1 channels remodel the cortical endoplasmic reticulum (cER) into tight connections with the plasma membrane (PM), likely through a direct interaction. Trafficking of membrane proteins, both exo- and endocytosis are localized to the perimeter of the Kv2.1-induced ER/PM contacts by virtue of remodeling the cER underneath the Kv2.1 clusters. Thus the clustering of Kv2.1 functions to bring protein trafficking and intermembrane signaling together at the neuronal soma.

TABLE OF CONTENTS

Chapter 1: Introduction

The human genome encodes a finite number of protein products (~23,000) which combine to make up an unimaginably complex biological organism. To accomplish such a feat, each protein must possess a multiplicity of functions, being able to perform similar or different biochemical tasks in a variety of circumstances. In eukaryotes, multiplicity of function is usually achieved by creating multiple variants of a single protein with different combinations of functional parts (splice variation, pre-translational) or by modifying a single protein dynamically to alter the function (post translational modification, or PTM). Research into the role that individual proteins play in the larger organism is dominated by the discovery of a single function, or biochemical activity which is attributable to that protein. Further research is generally initiated based on the importance of that function. However, as the body of scientific inquiry grows, the rule of multiplicity of function becomes more apparent. Thus, a general motivation for the proceeding work is that proteins possess a multiplicity of functions which are overshadowed by a dominant function.

The Plasma Membrane. All living cells possess a biological membrane barrier which separates the cell from the external environment, typically referred to as the plasma membrane (PM). The plasma membrane is composed of a lipid bilayer with an array of proteins partially or fully inserted into the bilayer. The lipid bilayer itself consists mostly of an orderly arrangement of phospholipids; containing two fatty acid tails and a phosphate head group connected by a triglyceride. Lipid bilayers self-assemble in aqueous environments, due to the polar nature of the phospholipids, into two leaflets, or layers in which the hydrophobic tails point inwards, towards one another and the hydrophilic phosphate head groups point outwards into the aqueous solution, saturated with water. The interior of the bilayer, where the hydrophobic tails reside is essentially free of water. This sets up a semi-permeable barrier that prevents bulk movement of water, charged molecules and macromolecules across the lipid bilayer (1).

In order to regulate the movement of otherwise impassible molecules across the lipid bilayer there exists an intricate system of protein-based carriers. The simplest mechanism involves the generation of an aqueous channel across the plasma membrane encapsulated from the hydrophobic tails of the lipid bilayer by similarly hydrophobic amino acid residues within the protein-based carrier. Proteins which operate by this mechanism are called channels. Due to the requirement of an unbroken aqueous environment in the interior of the protein, channels are limited to passing small, charged molecules. The movement of a molecule through a channel is dependent on the concentration of that molecule on either side of the membrane, and the electrical potential across the membrane (1).

Generation of concentration gradients and membrane potential. In an open system, the concentration of all molecules tends towards equilibrium through the process of diffusion from areas of higher concentration to areas of lower concentration. In order to alter the composition of the interior of the cell, relative to the external environment, cells must expend energy to move molecules away from equilibrium. A different class of protein carriers called transporters and pumps use biochemical energy to move molecules against the concentration gradient. Pumps use energy released from adenosine triphosphate (ATP) hydrolysis to move molecules into or out of the cell. The most active pump in the PM is the Na^+/K^+ ATPase. By pumping 3 Na^+ ions out of the cell and 2 K^+ ions into the cell with each cycle, the Na^+/K^+ ATPase sets up a high concentration of K^+, and a low concentration of Na^+ inside the cell. It also results in a net negative charge movement into the cell, which creates a negative membrane potential or voltage. Thus the interior of the cell is negatively charged relative to the exterior, like a biochemical battery. Transporters use the potential energy stored in the concentration gradients by coupling the movement of one molecule down the concentration gradient to the movement of another against the concentration gradient. Channels on the other hand only allow molecules to pass the membrane according to the chemical and electrical potentials that exist between the

cell and the external environment (1).

Diffusion within the lipid bilayer. The molecules embedded within the PM are not static, as once thought, but instead are fluid and diffuse laterally (in 2-dimensions) through the PM. The first model to describe the organization of the PM was the fluid mosaic model where molecules within the membrane generally proceed toward equilibrium due to diffusion (2). This model has largely been abandoned in favor of evidence that the PM is actually quite heterogeneous, with molecules distributed non-uniformly within the PM (3). Thus, the location of molecules in the PM is not random, but instead carefully controlled to optimize function.

Ion channels and the action potential. All cells expend large amounts of energy to set up ionic gradients and a membrane potential (MP), which in turn are used to drive the accumulation of other nutrients. Excitable cells are capable of rapidly manipulating the MP from the negative resting potential (polarized) to more neutral potentials (depolarized) and back again to the resting potential. Excitable cells include neurons, muscle cells and secretory cell such as such as the insulin-releasing β-cells of the pancreatic islets. These rapid fluctuations in MP are implemented by ion flux through ion channels. Although tremendous energy is expended setting up the ion gradients, ion flux through channels requires no direct energy consumption. Perhaps the most notable example of MP fluctuation is the neuronal action potential (AP). APs consist generally of a rising, depolarizing phase and falling repolarization phase. In the depolarizing phase, inward Na^+ flux through Na^+ channels adds positive charge to the cell, neutralizing the negative resting MP. In the repolarizing phase, outward K^+ flux through K^+ channels removes positive charges, bringing the MP back to the negative resting state. The process, collectively termed the action potential (AP), underlies secretion, muscle contraction and communication in the nervous system (4).

Potassium selective ion channels. Potassium (K^+) selective ion channels comprise the largest family of ion channels with 78 members in mammals. Accordingly, K^+ channels have the broadest structural diversity among ion channel families. The largest sub-family of K^+ channels are the voltage-gated K^+ channels (K_V) with 40 members. K_V channels are homo or heterotetramers assembled from α-subunits with six transmembrane domains and one pore (6TM/1P) or ion conduction pathway. K_V channels have both the N- and C-termini on the intracellular side of the membrane (5). As the name suggests, K_V channels open and close the conduction pathway in response to changes in membrane potential. Typically, Kv channels are in the closed state at the resting membrane potential of the cell, and switch to the open state in response to depolarizing changes to the membrane potential. The Kv channels are classically broken down into four groups, based on homology to four Kv channel subunits expressed in drosophila, Shaker, Shab, Shaw and Shal, which correspond to Kv families 1-4, respectively (5). Kv channels can also be separated based on the type of inactivation displayed by the currents they carry. Following channel opening in response to depolarizing MP changes, some voltage-gated channels enter a third state called inactivation, distinct from the open or closed states, in which the conduction pathway is closed, but the channel cannot switch into the open state. Once the MP returns to the resting potential, inactivated channels can recover by entering the closed state. Kv channels which display no inactivation of currents or slow inactivation of currents (over a period of seconds) fall into the category of delayed-rectifiers (DR). The name delayed-rectifier refers to the late onset of the DR current in the action potential waveform, and the outward-rectification of the K^+ current due to the voltage-dependent gating of the channel. Kv channels which display fast inactivation of currents (over a period of milliseconds) are called A-type channels. Kv channels utilize the strong K^+ gradient between the interior and exterior of the cell, established by the Na^+/K^+ ATPase, to efflux K^+ ions, adding a net negative charge to the membrane potential. K^+ efflux is required to return the MP to negative values following the depolarizing phase of the action potential. A-

type K^+ currents activate and inactivate on timescales similar to the voltage-gated Na^+ channels so that they modulate the initiation and rising phase of the AP. DR-type currents activate more slowly and govern the repolarizing phase of the action potential. The more slowly a K^+ channel activates, the less it shapes the waveform of a single AP. Although both types of Kv channels are indispensable, there is functional overlap among many of the Kv channels in each group, such that genetic deletion of one Kv α-subunit is potentially compensated by another. The necessity of such functional overlap may be explained by tissue specific expression or distinct sub-cellular localization of functionally similar α-subunits (4).

The Kv2 Family. The Kv2 family is homologous to the Shab channel in drosophila and has only two members, Kv2.1 and Kv2.2, which have very similar currents and subcellular localization, and only seem to be delineated by their tissue specific expression (6). An error in the initial cloning of Kv2.2 resulted in a premature stop codon in the C-terminus which in turn led to the generation of antibodies which poorly recognized the wild-type (WT) channel. This error has only recently been corrected, and is largely responsible for the current focus of research on Kv2.1 instead of Kv2.2 (6). The current carried by Kv2 subunits is not present at the time of birth in rodents, but develops over the first three week postnatal in the cortex (7). Kv2.1 is the major delayed-rectifier in the mammalian brain and is responsible for the majority (up to 80%) of the delayed-rectifier current (IK_{DR}) in principal neurons of the cortex and hippocampus (8-10). In the absence of Kv2.1, action potential waveform is normal at low frequency (0.2 Hz), while at higher frequencies (1.0 Hz) action potential repolarization quickly decays and action potential firing is terminated due to a failure to repolarize (11). The Kv2.1 current is active in between AP spikes, and works to keep the MP negative enough for Nav channels to recover from inactivation. Thus the channel enables high frequency AP firing by promoting the recovery of inactivated Nav channels (8).

Subcellular localization of Kv2.1. Kv2.1 displays a somato-dendritic localization, where channels are restricted to the neuronal soma and the proximal dendrites (~10 microns) (12). Paradoxically, Kv2.1 also localizes to the axon initial segment, but does not project further down the axon (13). The somato-dendritic localization is likely due to trafficking of vesicles to these region and exclusion of vesicles from other neuronal compartments (14). The nature of the AIS localization is poorly understood, especially considering the presence of an AIS membrane diffusion barrier which should prevent diffusion of ion channels into this region (15).

Within the AIS and somato-dendritic regions, there are two distinct populations of Kv2.1 channels. One population localizes to micron-sized clusters within the somato-dendritic and AIS regions, while the second population is relatively free to diffuse within these regions (16, 17). The pattern of Kv2.1 localization i.e. large somato-dendritic/AIS clusters is unique among Kv channels, and ion channels in general. Electron microscopy of Kv2.1 clusters indicates that in the intact hippocampus, clusters generally lie in between astrocyte process on the extracellular side and projections of the endoplasmic reticulum called sub-surface cisterns (SSCs) on the intracellular side (18). Thus the PM where the clusters reside is surrounded on both sides by other lipid bilayers. Light microscopy supports this observation, showing partial co-localization between Kv2.1 clusters and ryanodine receptors (19, 20). Similarly, in α-motor neurons of the spinal cord, Kv2.1 clusters reside atop SSCs and co-localize with cholinergic terminals (21). Interestingly, Kv2.1 clusters cannot be extracted by common non-ionic detergents such as triton X-100 and are considered detergent insoluble (22). For this reason, studies of Kv2.1 protein interactions use only the non-clustered channels.

Functional domains of Kv2.1. Like other members of the Kv channel family, Kv2.1 has six transmembrane domains and a single re-entrant pore loop between transmembrane domains five (S5) and six (S6). Like other voltage-gated channels, Kv2.1 has a positively charged fourth

transmembrane domain (S4) which functions as a voltage sensor and participates in voltage-dependent gating of the channels. Kv2.1 also contain a tetramerization domain on the N-terminus that restricts which α-subunits Kv2.1 can heterotetramerize with. The Kv2 family is notable in that it can heterotetramerize to form functional channels with α-subunits of the silent Kv channels (Kv5, Kv6, Kv8 and Kv9) which cannot form functional channels by themselves (5). In the case of Kv9.3, three Kv2 subunits typically heterotetramerize with one silent subunit to form a channel with different characteristics than a Kv2 homotetramer, making the silent Kv subunits modulatory in nature (23). Specific regions in the N- and C- termini interact with one another, presumably from one α-subunit to another within the tetramer. These interactions are critical for channel trafficking out of the endoplasmic reticulum (24). The most notable functional domains lie within the cytoplasmic C-terminus of Kv2.1, which is over 400 amino acids long and makes up over half the mass of the channel. The length of the C-terminus is unique among Kv channels, as is the fact that it contains little in the way of recognizable protein motifs. The proximal C-terminus contains a syntaxin1a binding domain (SBD) from residues 411-522 (25), which plays a role in facilitating exocytosis. Perhaps the most interesting functional motif is the 26 amino-acid domain named the proximal regulation of clustering (PRC) domain between residues 573-598, which is required for cluster localization of Kv2.1 (26). Transfer of this domain to other Kv channels is sufficient to endow the clustered phenotype (27). The PRC shows no homology to any known functional protein motif, suggesting that both the Kv2.1 clusters the mechanism for localization are unique in biology.

Modulation of Kv2.1 channel function. Despite the lack of well described functional domains within the C-terminus, this region of the channel contains targets for a large number of post-translational modifications (PTM). Within the amino acid sequence of Kv2.1 there are up to 60 consensus phosphorylation sites (28). 16 of these sites have been shown to be phosphorylated in HEK cells, while several other are likely phosphorylated based on the results of mutational

analysis (26). In the intact adult brain, the majority of these serine residues are phosphorylated (29). Chemical dephosphorylation of the channel causes all of the different MW species to collapse to a single smaller MW band, indicating a fully dephosphorylated channel subunit. The phosphorylation state of the channel is closely connected to both the voltage-dependence of channel gating and the sub-cellular localization to clusters. Large scale Ca^{2+} influx in neurons leads to activation of a Ca^{2+} activated phosphatase called calcineurin, which in turn leads to dephosphorylation of many of the serine residues on the C-terminus of Kv2.1 (29). This dephosphorylation is inexorably linked to a 10-15 mV leftward shift in the voltage-dependence of channel gating, causing Kv2.1 to open at more negative potentials (30). This effectively increases the activity of the channel and subsequently reduces the intrinsic activity of the neuron by providing a constant K^+ flux and pushing the MP towards more negative potentials. Dephosphorylation of Kv2.1 is also linked to a loss of channel clustering. While the leftward shift in voltage dependence of activation and channel declustering occur simultaneously in experimental conditions, they appear to be distinct, separable processes which both rely on channel phosphorylation.

Aside from the plethora of phosphorylation sites on the C-terminus of Kv2.1 there are also two phosphorylation sites on the N-terminus which regulate channel trafficking and surface expression (28, 31). Another type of PTM, called sumoylation, consists of the attachment of a small ubiquitin-like modifier (SUMO) to lysine 470 of Kv2.1. The Kv2.1 tetramer can be maximally sumoylated on only two of the four K470 residues and each sumo modification results in a 15-mv leftward shift in the voltage dependence of activation, which is similar in scale to full dephosphorylation (32). The single channel conductance of Kv2.1 is modulated by the concentration of extracellular K^+. A two-fold increase in the extracellular K^+ concentration results in a roughly two-fold increase in the single channel conductance of Kv2.1. The decrease in the concentration gradient for K^+ is effectively offset by the increased single channel conductance which allows the same number of

ion to flux, thus allowing the Kv2.1 current to remain constant even under heavy firing conditions which might elevate extracellular K^+ (33, 34). Kv2.1 is sensitive to oxidation at a single specific residue, cysteine 73, which results in oligmerization of channel subunits by sulfhydryle bonds, and an acute decrease in Kv2.1 current. This type of oxidation is significantly increased in the brain of aged mice (35). Kv2.1 currents are also acutely inhibited by carbon monoxide and hypoxia, although this does not appear to be direct effect on the channel (36, 37).

Expression of Kv2.1 in mammalian tissues. Abundant Kv2.1 expression and current has been detected in a number of brain regions including the hippocampus, cortex, globus pallidus, hypothalamus and substantia nigra (9, 11, 38-40). Peripheral to the brain, Kv2.1 expression has also been observed in α-motor neurons in the spinal cord, and superior cervical ganglion in the peripheral nervous system (21) (8). Beyond neurons, Kv2.1 expression and currents are found in smooth muscle cells and pancreatic β-cells (41, 42). Kv2.1 is expressed in both glutamtergic and gabaergic neurons of the hippocampus and cortex, while in the hypothalamus and substantia nigra Kv2.1 is expressed in agouti-related protein/neuropeptide Y (AgRP/NPY) neurons and dopaminergic neurons respectively.

Kv2.1 Pathophysiology. In the intact brain, Kv2.1 is exquisitely sensitive to stroke-like insults such as hypoxia and ischemia. Exposure to hypoxia for two minutes is sufficient to completely de-cluster Kv2.1 in the hippocampus and cortex (29). Similarly, glutamate excitotoxicity and chemical ischemia with oxygen-glucose deprivation (OGD) can acutely shift the voltage-dependence of channel gating leftward by 10-15 mV (29). Both effects are mediated by Ca^{2+} dependent activation of the protein phosphatase Calcineurin, and subsequent dephosphorylation of the Kv2.1 C-terminus. The leftward shift in activation midpoint has the expected effect of decreasing neuronal excitability and, in conditions of ischemia, this dampening of neuronal

excitability is neuroprotective (30, 43). Conversely, the Kv2.1 de-clustering which accompanies the leftward shift in activation midpoint serves no known protective function.

Kv2.1 also plays a critical role in the unfolding of the apoptotic cascade in neurons. Apoptosis is punctuated by a series of biochemical checkpoints including an efflux of intracellular K^+ which collapses the normal K^+ gradient. In neurons of the cortex and hippocampus, apoptosis induced by oxidative stress relies on a 3-fold increase in surface expression of Kv2.1 to carry the K^+ flux (44). Preventing the K^+ efflux, either by blocking channel function with tetraethylammonium (TEA) or by mutating a single tyrosine residue which controls the increased Kv2.1 trafficking, prevents the completion of the apoptosis program (31). The upregulation of Kv2.1 current can also be blocked by disrupting the interaction of syntaxin1a with the SBD of Kv2.1 using a competitive peptide (45). Thus, it appears that Kv2.1 plays an active role in the trafficking of the vesicles in which it resides by recruiting syntaxin1a. Even exposure to CO, which inhibits the Kv2.1 current is sufficient to block K^+ efflux and stop apoptosis (36). Regardless of how the upregulation of the Kv2.1 current is blocked, the end result is greater neuron survival.

Mice with a genetic deletion of the Kv2.1 gene appear to be normal, with no glaring defects, aside from a reduction in body weight. Closer observation reveals that deletion of the Kv2.1 gene results in several behavior abnormalities. Kv2.1$^{-/-}$ mice are hyperactive and less anxious than their wild-type littermates. The Kv2.1$^{-/-}$ mice exhibit some defects is special learning and have decreased long-term potentiation at the Schaffer collateral/CA1 synapse. The Kv2.1 knock-out mice are hypersensitive to chemical-induced seizures although they are not prone to spontaneous seizures. The genetic deletion of Kv2.1 appears to occur without major compensation by other Kv channels (46).

Non-channel function of Kv2.1. The vast majority of the research into the physiological function of Kv2.1 has focused on the current carried by the channel and the modulation of that

current. However, research into the interaction between Kv2.1 and sytaxin1a has shown that Kv2.1 expression facilitates exocytosis in PC-12 cells. The facilitation of exocytosis is dependent on the Kv2.1 SBD, but surprisingly does not require a functional ion conduction pathway (25, 47). Thus, a non-channel function of Kv2.1 is to promote vesicle exocytosis through interaction with syntaxin1a.

Mechanism of Kv2.1 clustering. The sensitivity of Kv2.1 clusters to various types of neuronal insults such as glutamate excitotoxicity, chemical ischemia and hypoxia would suggest that the localization of Kv2.1 in clusters is a physiologically important adaptation of the channel. It was initially postulated that phosphorylated channels were localized to clusters through tethering to a sub-membranous scaffolding protein, like those found at post-synaptic densities (48). Localization to the cluster exposed Kv2.1 channels to further phosphorylation by kinases which also localize to the clusters, thus reinforcing channel tethering to the sub-membranous scaffold. In this model, Ca^{2+} influx due to neuronal insults would cause an initial dephosphrylation of the channel within the clusters, which would cause Kv2.1 to unbind the sub-membranous scaffold. Once free of the scaffold, Kv2.1 channels would be free to diffuse out of the cluster, removing them from the influence of the kinases localized to the cluster. Gradually the channel would undergo more dephosphorylation leading to a neuroprotective leftward shift in activation midpoint (29, 48, 49). This model led to two testable hypotheses. Kv2.1 channels localized to clusters should experience long-term (tens of seconds) static tethering which would drastically decrease the normal diffusion of the channel within the PM, and Kv2.1 channels localized to clusters would have a rightward shifted voltage dependence of gating compared to non-clustered channels.

Measurement of the diffusion of Kv2.1 channels inside and outside of clusters revealed that the two populations diffuse at almost the same rate, with clustered channels diffusing at about half the rate of non-clustered channels (17). Furthermore, single particle tracking (SPT) of Kv2.1 channels revealed that the diffusion of individual channels was essentially unhindered within the

cluster, but at the cluster perimeter, there was a diffusion limiting barrier that clustered channel could not cross. Non-clustered channels could diffuse freely past the barrier, through the cluster and out again (16). Thus the clustered channels had some modificaition which trapped them within the diffusion limiting barrier, while non-clustered channel lacked this modification. A non-clustered channel did not become clustered by virtue of passing through the cluster, arguing against a localization of cluster-maintaining kinases within the cluster. These finding did not fit the initial Kv2.1 cluster model, and argue for an uncommon localization mechanism.

Location-dependent function of Kv2.1. As discussed in the previous section, the initial model describing Kv2.1 clustering led the hypothesis that clustered Kv2.1 channel would have a rightward shifted voltage-dependence relative to non-clustered channels. This hypothesis was tested directly by cell-attached patch clamp of Kv2.1 clusters and non-clustered cell regions. Surprisingly, channels outside of clusters produced currents identical to those measure in whole-cell voltage clamp, while channels within clusters produced no current or single-channel currents, indicating that out of the 100s of channels within the clusters only one, or at most, a few were fluxing K^+. Based on whole-cell gating current measurements, is appeared that clustered channels were still generating gating currents in response to depolarization, but not opening to flux K^+. Release of channels from clusters by actin depolymerization failed to increase whole cell currents, indicating that non-conducing, clustered channels did not begin conducting K^+ following release from the cluster. Thus, the non-conducting, clustered channels do not behave like a silent reservoir of channel awaiting release from clusters in order to activate.

Trafficking of Kv2.1 Channels. Kv2.1, like all integral membrane proteins, is synthesized by ribosomes on the endoplasmic reticulum (ER) directly into the ER membrane. Kv2.1 proceeds through the trans-golgi apparatus where it undergoes N-linked glycosylation (50). Post-golgi vesicles containing Kv2.1 are trafficked to the cell surface by Myosin IIB motors on actin filaments.

This trafficking route may underlie the somato-dendritic localization of Kv2.1, since a different microtubule-based system was employed by Kv4.2 which is expressed in more distal dendrites. A single serine point mutation (S586A) within the proximal restriction and clustering domain (PRC) which abrogates Kv2.1 clustering also alters the behavior of vesicles containing Kv2.1 to become more like those carrying Kv4.2, which traffic to the distal dendrites (14). Interestingly, vesicles containing Kv2.1 approach and fuse with the plasma membrane at the periphery of Kv2.1 clusters, delivering channels directly to the cluster. Another Kv channel from a different family, Kv1.4 is also delivered in this manner; however the channels diffuse freely away from the site of vesicle fusion, unlike Kv2.1 (51). Thus Kv2.1 channels appears to regulate the trafficking route of the vesicles in which they are carried, while clustering of Kv2.1 on the cell-surface localizes Kv channel traffic around the periphery of the cluster. Both processes are dependent upon the actin cytoskeleton as both are disrupted with actin inhbitors such as Latrunculin A, Cytochalasin D and Swinholide A (14, 51).

Recycling of Kv2.1 channels from the cell surface. Once synthesized in the ER, Kv2.1 channels traffic efficiently to the cell surface (17). This is in contrast to some other Kv channels which are retained within the ER until an interaction with an accessory protein or β-subunit allow the channel to be released from the ER (52). Once on the cell surface, a percentage of Kv2.1 channels are internalized into recycling endosomes, which frequently re-deliver channels to the cell surface. This ongoing cycle of endo- and exocytosis occurs almost exclusively at the perimeter of Kv2.1 clusters (51). Single particle tracking of Kv2.1 shows that channels become trapped within clathrin-coated pits around the periphery of the Kv2.1 clusters prior to endocytosis (53). Kv1.4 channels are also internalized at the perimeter of the Kv2.1 clusters, indicating that the clusters are sites of localized endo- and exocytosis (51). Thus Kv2.1 seems to play a role in the patterning of the PM into functional domains.

Kv2.1 expression in heterologous cells. Like most ion channels, Kv2.1 was first studied in isolation by ectopic expression in heterologous cells. The Kv2.1 current in isolation appears very similar to the currents ascribed to Kv2.1 in native cells (22). Interestingly, the midpoint of voltage-dependent activation, which is regulated by phosphorylation state of the channel, is very different among different cell lines, suggesting that the endogenous kinases in these cells are able to phosphorylate Kv2.1 to different degrees (27). Similarly, only some of the cell lines are capable of recapitulating the Kv2.1 cluster pattern as it appears in hippocampal neurons. Expression of Kv2.1 in human embryonic kidney (HEK) 293 cells results in micron-sized Kv2.1 cluster reminiscent of those found endogenously in hippocampal neurons (16). In HEK cells, the activation midpoint of Kv2.1 is very close to that measure from endogenous channels in cultured neurons. Kv2.1 expression in Cercopithecus aethiops (COS-1) kidney cells results in an activation midpoint that is leftward-shifted compared to hippocampal neurons, as if the channel was already partially dephosphorylated. COS-1 cells also fail to form Kv2.1 surface clusters (27).

The endoplasmic reticulum. The endoplasmic reticulum is a membranous organelle which includes the nuclear envelope and stretches out to the cell periphery in a system of cisterns (sheets) and tubules (54). Of the major cellular organelles (nucleus, cytoskeleton, golgi apparatus) the endoplasmic reticulum was the last to be discovered, due to the extensive articulation of the ER throughout the cell. It was not until the advent of electron microscopy of fixed and negatively contrasted eukaryotic cells that the ER, described as a “lace-like reticulum” was apparent (55). The ER has several functions which are critical in cell biology. The ER is first and foremost the site of protein synthesis for all integral membrane and secreted proteins (56). The ER lumen, which is continuous throughout the cell, supports the proper folding of proteins and is the first checkpoint for quality control along the trafficking pathway (57). The ER lumen is also a Ca^{2+} store, with a roughly 1000-fold higher concentration than the cytoplasm which is maintained by Ca^{2+} selective ATPases (Sarco-Endoplasmic Reticulum ATPase, or SERCA) in the

ER membrane (56). Furthermore, several important metabolic processes are localized to the ER membrane including those involved in *de novo* lipid and cholesterol synthesis (58). In neurons, ER Ca^{2+} signaling is participates in synaptic transmission by regulating synaptic vesicle release, highlighting the extensive involvement of this organelle in all parts of the cell (59).

Endoplasmic reticulum membrane contact sites. The ER is notable in that it participates in direct connections with almost every other membranous organelle, in part due to the expansive nature of the organelle (60). These connections between membranes organelles, called membrane contact sites (MCS), are facilitated by interactions between proteins and sometimes lipids across the two membranes (61). The first MCS was discovered in skeletal muscle between the sarcoplasmic reticulum (a specialized outgrowth of the ER) and t-tubules (specialized extensions of the PM). This MCS, also called an endoplasmic reticulum/plasma membrane (ER/PM) junction, allows voltage-gated Ca^{2+} (Cav) channels on the PM to interact directly with ER Ca^{2+} release channels (ryanodine receptors, RYRs) to transform an electrical potential in muscle contraction in a process called excitation-contraction (EC) coupling(62). The second observation of ER/PM junctions was in neurons where they were referred to as sub-surface cisterns (SSCs). SSCs are abundant in a variety of vertebrate neuronal cell types in the peripheral and central nervous systems (63). Unlike skeletal muscle, where the form and function of the ER/PM junctions is clear, the function of neuronal ER/PM junctions remains elusive (60, 61, 64). Recently, there has been a resurgence of interest in ER/PM junctions in a variety of cell types due to the discovery of a protein named stromal interaction molecule 1 (STIM1), which forms and localizes to ER/PM junctions in response to depletion of high ER Ca^{2+} concentrations (65). STIM1 is a single transmembrane ER resident protein with a Ca^{2+} sensing EF-hand motif in the ER lumen, and cytoplasmic domains which allow STIM1 to bind to phospholipids in the PM, and activate PM ion channels in response to ER Ca^{2+} depletion (66). STIM1 and a PM Ca^{2+} channel Orai1 were discovered in lymphocytes where genetic disruption of either protein leads to a severe

combined immunodeficiency. Ca^{2+} flux through Orai1, which is gated by activated STIM1, is critical for the activation of lymphocytes into mature effector cells (67). A newly discovered family of proteins called the extended synaptotagmins (E-Syt) also induce ER/PM junction via C2 domains which bind to phosphatidyl inositol triphosphate 2 (PIP_2) (68). There is evidence that the E-Syts function to shuttle lipids between the two membranes, adding another potential function of ER/PM junctions (45).

Overview of this Dissertation. This thesis focuses on the relationship between the sub-cellular localization of the Kv2.1 K^+ channel and the functional properties of the channel. The research presented here builds on previous work demonstrating that the subcellular localization of Kv2.1 into clusters is a dynamic process that is related to changes in channel function (16, 69). The clustering of Kv2.1 occurs through an uncommon and poorly understood mechanism that is closely related to a non-conducting state of the channel. The Kv2.1 clusters themselves are uniquely involved in membrane protein trafficking and recycling (51). The goal if this work is to answer the following questions. What is the relationship between Kv2.1 clustering and the non-conducting state? What is the purpose of the non-conducting state? What is the purpose of clustering? How do the clusters localize protein traffic at the PM? Together, the data presented here shed light on all of these questions and are broken into the following sections.

Chapter 2: Regulation of Kv2.1 K+ conductance by cell surface channel density. Here I developed a single channel counting technique to quantify the number of Kv2.1 channels expressed in HEK cells and in cultured neurons to address the relationship between clustered localization and the non-conducting state.

Chapter 3: Induction of stable endoplasmic reticulum/plasma membrane junctions by Kv2.1 potassium channels. Here I used light and electron microscopy to show that Kv2.1 clusters induce

close contact between the PM and cortical ER (cER). This interaction likely underlies the mechanism of Kv2.1 clustering, and sheds more light on the purpose of Kv2.1 clustering.

Chapter 4: Plasma membrane domains enriched in cortical endoplasmic reticulum function as membrane protein trafficking hubs. Here I showed that Kv2.1 clusters localize above projections of the cER and I used light microscopy to observe the location of vesicle fusion relative to the cER to map the relationship between the two.

Chapter 2: Regulation of Kv2.1 K^+ conductance by cell surface channel density

Introduction

Voltage-gated K^+ channels (Kv) are expressed in most excitable cells where they regulate membrane potential. Kv2.1 is among the most ubiquitously expressed Kv channel subunits in the mammalian brain where it mediates the majority of the delayed rectifier current (Ik_{DR}) in principal neurons of the hippocampus and cortex and regulates the action potential waveform during repetitive stimulation (9-11, 70). Unique to Kv2.1 is its localization to high density cell-surface clusters in intact brain, cultured neurons and transfected HEK cells (26, 29, 71). In addition, there is a second population of non-clustered Kv2.1 channels which are spread diffusely over the cell surface (17). Kv2.1 clusters are dynamic structures that disperse and release channels in response to noxious stimuli such as ischemia, hypoxia and glutamate excitotoxicity (30, 43). Associated with the release of Kv2.1 from clusters is a leftward shift in activation midpoint, likely induced by dephosphorylation within the intracellular carboxyl terminu (28, 49). It was postulated that channels residing within clusters have a high threshold for activation, whereas non-clustered channels have a lower activation threshold.

Recently, we discovered using cell-attached patch clamp that channels residing within clusters are almost exclusively held in a non-conducting state, contradicting the hypothesis that clustered Kv2.1 are high threshold channels with respect to their voltage-sensitivity (69). However, cell-attached patch clamp recordings can underestimate the number of voltage-gated sodium channels in the axon initial segment due to interference of the actin cytoskeleton (72) raising the possibility that the non-conducting Kv2.1 was an artifact of the cell-attached patch clamp technique. In addition, it was possible that the non-conducting state is specific to Kv2.1 channels

expressed in HEK cells and does not apply to the endogenous channel in hippocampal neurons even though the neuronal machinery affecting Kv2.1 localization and function is present in HEK cells (27), which is perhaps not surprising since HEK cells express many neuronal markers and may be of neuronal origin (73).

To address the first issue we performed whole-cell voltage-clamp recordings on HEK cells in conjunction with TIRF-based quantitation of cell-surface Kv2.1 channel density to relate channel number to channel conductance. This approach also identified a large non-conducting population of channels. The second issue was addressed by standardizing anti-Kv2.1 immunolabeling to Kv2.1 surface density in the HEK cell system and then determining the expression levels of the endogenous Kv2.1 in cultured hippocampal neurons via immunofluorescence. We find that the non-conducting state depends more on surface density than on location within a cluster and that this non-conducting state also exists for the native Kv2.1 found in cultured hippocampal neurons.

Materials and Methods

Plasmid constructs, cell culture and transfections. Fluorescent protein tagged Kv channel constructs, based on the Living Colors vector system (Clontech), have been described previously (12, 16, 17, 71). The N-terminal fusion of Kv1.4 with GFP blocks the fast inactivation normally seen with this channel (74). HEK 293 cells (American Type Culture Collection, passage 38-45) cells were transfected with 0.5-3 µg of Kv expressing DNA using a BioRad Genepulser Xcell (BioRad Laboratories, Hercules, CA) with a 0.2 cm gap cuvette and a single 110 V 25 msec pulse. Transfected cells were then plated on glass-bottom 35 mm dishes (Matek, Ashland, MA) that had been coated previously with Matrigel (BD Biosciences) and covered in DMEM + 10% fetal bovine serum. HEK cells were imaged within 24 hours of electroporation in HEK physiological saline consisting of (in mM): 146 NaCl, 4.7 KCl, 2.5 $CaCl_2$, 1 $MgCl_2$, 10 glucose and 10 Hepes, pH 7.4. Neurons from cryo-preserved E18 rat hippocampal dissociations of both sexes were plated at a

density of ~15,000 - 30,000 cells/cm^2 on poly-D-lysine coated glass-bottom dishes (Mattek) and cultured in glial-cell conditioned neurobasal medium (GCM) containing B27 supplement (Invitrogen) as previously described (17). Every 3–4 days after plating, one-half of the culture medium was replaced with GCM. Animals were deeply anesthetized with isoflurane and euthanized by decapitation according to a protocol approved by the Institutional Animal Care and Use Committee (IACUC) of Colorado State University.

Immunocytochemistry. Neurons and HEK cells were fixed with 4% formaldehyde, in phosphate buffered saline (PBS) for 15 min at 37°C, incubated in 0.5% 3-[(3-Cholamidopropyl)dimethylammonio]-1-propanesulfonate (CHAPS) in PBS, blocked in 10% goat serum in PBS, and labeled with the indicated antibody diluted in PBS containing 1% BSA. A mouse monoclonal anti-Kv2.1 antibody (NeuroMabs, Davis, CA, 1:1000 dilution) was used in conjunction with a goat anti-mouse secondary antibody conjugated to Alexa 594 (Molecular Probes) diluted 1:1000 in 1% BSA PBS (Misonou et al., 2005). For live-cell labeling, HEK cells expressing GFP-Kv2.1-HA were labeled for 15 min at 37°C with a 1:1000 dilution of an anti-HA antibody conjugated to AlexaFluor594 (Invitrogen, Carlsbad, CA) in physiological saline containing 1% BSA.

3D quantification of clustered membrane area. HEK cells transfected with GFP-Kv2.1 were labeled with DiI at 37°C for 5 minutes and washed 3x with imaging saline prior to imaging. Cultured hippocampal neurons were labeled with wheat-germ agglutinin (WGA) at 37°C for 5 minutes and washed 3x with imaging saline prior to fixation and subsequent immunolabeling for endogenous Kv2.1. Confocal z-steps (0.3μm) were acquired for 3D reconstruction and the intensities of all fluorophores were adjusted so the fluorescent volume would be similar and could be used as a relative measure of surface area. Either Kv2.1 clusters or the entire membrane were measured in 3-dimentions using an automated object finding protocol in Volocity 6.0 (PerkinElmer, Waltham,

MA). Occasionally, intracellular fluorescence was aberrantly selected by the object finding protocol. To avoid this potential artifact, intracellular fluorescence was removed in Adobe Photoshop to within 1μm of the PM as determined by the DiI or WGA. In neurons, this analysis was restricted to the soma and the most proximal portions of the neurites where Kv2.1 clusters typically form.

Measurement of single channel GFP intensity. HEK cells transfected with GFP-Kv2.1 were photobleached during TIRF imaging and single GFP molecule fluorescence intensity determined by quantitating the bleach step magnitude. The fluorescence intensity of a single channel was divided by the mean bleach-step magnitude and the data placed into bins of 0.5-1.5, 1.5-2.5, 2.5-3.5 and 3.5-4.5. Any puncta greater than 4.5-fold the mean single GFP bleach-step magnitude were excluded from the analysis since these could represent multiple channels. The binned data were fit to a binomial distribution of four fluorescent GFP molecules with an independent folding efficiency for GFP of 74% (see Figure 2C), (32, 75, 76).

In the electrophysiology experiments it was impractical to obtain individual bleach-steps since the majority of cell recordings were discarded for voltage-clamp quality control issues, such as increasing series resistance, increasing membrane leak, etc. Instead, the fluorescent intensity of discrete puncta from a nearby cell was measured from a single frame where the intensity was greatest. The brightest puncta correspond to single channels with four functional GFP molecules. These measurements were divided by four and averaged to give us the single GFP fluorescence intensity. This intensity was plugged into a binomial distribution of four fluorescent GFP molecules with a folding efficiency of 74% to get the representative single channel fluorescence intensity. The GFP intensity of clustered and non-clustered regions of the TIRF footprint were measured and divided by the single channel fluorescence intensity to obtain the Kv2.1 channel density in these regions. Channel density was multiplied by whole-cell C_M, based on voltage-clamp recordings, to extrapolate measurements from the TIRF footprint to the whole cell. The TIRF

imaging conditions were carefully optimized to maximize the signal-to-noise of single GFP-Kv2.1 channels while minimizing the total internal reflection (TIR) penetration depth and 488nm laser intensity to remain within the linear range of the EM-CCD camera (roughly 100 to 10000). A calculated penetration depth of 144nm and 10% 488nm laser intensity satisfied these criteria.

Confocal and TIRF microscopy. HEK cells and neurons expressing fluorescent protein tagged constructs or immunolabeled with fluorophores were imaged with one of two microscope systems depending on the experiment performed. Standard 3D imaging, 0.3 μm z-steps, was performed with an Olympus FV1000 confocal microscope equipped with spectral detectors and the SIM scanner. GFP was excited using the 488 nm line of an argon laser and emission was collected using the variable bandpass filter set at 500-530 nm. Alexa 594 fluorophores were detected using a 543 nm HeNe laser with the variable bandpass filter set at 600-700 nm. A 60X, 1.4NA oil immersion objective was used for imaging and the pinhole diameter set for the appropriate Airy unit when using one laser. A comprised pinhole diameter was used when two fluorophores were being detected simultaneously. For quantitative imaging, the detector voltage and laser power were kept constant at levels that avoided signal saturation. The second system is a Nikon Eclipse Ti Perfect-Focus equipped TIRF/widefield fluorescence microscope equipped with AOTF controlled 405, 488, 561nm diode lasers, 100 mW each, and an Intensilight wide-field light source. A 100X PlanApo TIRF, 1.49 NA, objective was used for image acquisition. Emission was collected through a Sutter Lambda 10-3 filter wheel containing the appropriate band pass filters. This microscope is equipped with the Andor iXon EMCCD DU-897 camera, 512x512. For TIRF image acquisition we used an incident angle of 63.3°, calculated using the following equation: $\sin\theta = 2 \times R \times M / (200{,}000 \times n_1)$, where R is the distance of the laser illumination position from the center (1,360μm), M is the magnification of the objective (100x), n_1 is the refractive index of the cover glass (1.522). From the incident angle the penetration depth was calculated to be 144nm based on the equation: $d = \lambda / 4\pi \times [n_1^2 \times \sin^2\theta - n_2^2]^{1/2}$], where λ is the laser wavelength (488nm), θ is

the incident light angle to the boundary surface between the cover glass and the culture fluid where $\theta > \theta_c$ (θ_c is the critical angle, $\mathrm{Sin}\theta_c = n_2 / n_1$), n_1 is the refractive index of the cover glass and n_2 is the refractive index of the culture fluid (1.333). At this penetration depth we rarely observed out-of-focus fluorescence from intracellular sources however it is impossible to exclude fluorescence from intracellular organelles near the PM such as trafficking vesicles and endoplasmic reticulum (ER). To confirm that our imaging conditions did not typically illuminate intracellular structures we labeled HEK cells expressing GFP-Kv2.1-HA, containing an engineered extracellular HA epitope in the S1-S2 loop (71), with an anti-HA antibody conjugated to AlexaFluor-594. The ratio of GFP:Alexa594 fluorescence was stable at ~5:1 over a range of penetration depths (91nm to 182nm) but quickly increased to 10:1 when TIR was lost after passing the critical angle (61.1°, data not shown). Furthermore, the relationship between GFP and Alexa594 fluorescence was linear over two orders of magnitude of GFP intensity, within the range of measurements used for quantification of Kv2.1 channel number (Figure 5B). Previous studies have demonstrated that GFP-Kv2.1 traffics well to the cell-surface and does not accumulate in the ER (16, 17). While a recycling population of Kv2.1 is present near the PM in endosomal vesicles, these represent <2% of the fluorescence observed under our standard TIRF parameters (51).

Whole-Cell Ionic Current Measurements. HEK cells transfected with fluorescent Kv constructs were trypsinized 24 h after electroporation and replated on 35-mm glass bottom dishes coated with ECL cell attachment matrix (Millipore). After 2 h, cells were washed extensively with whole-cell external recording solution, containing (in mM) 140 NaCl, 5 KCl, 10 $CaCl_2$, 2 $MgCl_2$, 10 glucose, and 10 Hepes, pH 7.4. When 20 mM TEA-Cl was added to the external solution to reduce Kv2.1 currents by ~80% NaCl was reduced to maintain isotonic conditions. Pipettes were pulled from thin-walled borosilicate glass and had a resistance of 1.4–2.2 MΩ when filled with intracellular solution (150 KCl, 1 $MgCl_2$, 4 NaCl, 0.5 EGTA, and 10 Hepes, pH 7.4). For Kv1.4

current measurements, whole-cell external solution was modified to have 150 mM KCl instead of NaCl, and the intracellular solution was modified to have 100 mM KCl, and 50 mM NMDG in order to reduce the current magnitude.

For measurements in cultured hippocampal neurons, tetrodotoxin (100 nM) was included in the neuronal recording solution (126 NaCl, 2.5 KCl, 1.2 $MgCl_2$, 2.5 $CaCl_2$, 1.2 NaH_2PO_4, 10 HEPES, and 11.1 glucose, pH 7.4) to block voltage dependent sodium currents. Neuronal intracellular recording solution contained 115 KCl, 20 NaCl, 1.5 $MgCl_2$, 5 HEPES, 0.5 EGTA and 1.6 K_2ATP, pH7.4. To determine the contribution of Kv2.1 to the Ik_{DR} in our preparation, we applied the Kv2 family-specific Stromatoxin (ScTx) (Alomone Labs, Jerusalem, Israel), a gating modifier which shifts the activation midpoint of Kv2.1 by +60mV in HEK cells. At +40mV, 600nM ScTx, a concentration reported to block ~75-80% of endogenous Kv2 in neurons (7, 70), blocked Ik_{DR} 125ms after depolarization by ~47% at 14-15 DIV and by ~46% at 20-21 DIV, indicating at least half of Ik_{DR} is mediated by Kv2 subunits at both maturity points. Since the dosage of ScTx used here does not fully block Kv2 channels we increased the contribution of Kv2 to Ik_{DR} to 60% for both timepoints (47% + (47% x .25) = 58.75%). Since Kv2.2 is not significantly expressed in hippocampal neurons we can exclude the contribution of this channel (6). ScTx also blocks Kv4.3 with a similar affinity as Kv2 subunits; however this channel is rapidly inactivating and should be largely excluded from Ik_{DR}.

Whole-cell K^+ currents were recorded at room temperature using an Axopatch 200B amplifier (Axon Instruments). Ionic currents were capacitance and series-resistance compensated by 80-90%, sampled at 10 kHz (Digidata 1440; Axon Instruments), and filtered at 2 kHz. Leak subtraction was performed online using the P/4 method in pClamp10 but non-subtracted records were used to assess data quality. Cells were held at −80 mV and depolarized to potentials between -60 and +60 mV in 10-mV steps with an interpulse interval of 10 s. Peak ionic currents were converted to conductance using the equation G = I/(V – EK). EK was calculated to be −85

mV. Voltage-activation curves were obtained by plotting peak tail currents obtained at −40 mV against the previous command potential. A standard Boltzmann fit was used to determine the voltage for half-maximal activation ($y=A2 + (A1-A2) / (1+e^{(x-x0)/dx})$). C_M was automatically calculated from a 10mV test pulse in pClamp10, and was measured 5 minutes after break-in to allow cell parameters to stabilize. Current density was calculated by dividing peak current by C_M. When needed, C_M was converted to membrane surface area with the specific capacitance for HEK cells (1.11 μF/cm^2) and cultured hippocampal neurons (0.92 μF/cm^2) (77).

One of the inherent drawbacks of measuring large (>10 nA) currents typical of Kv2.1 and Kv1.4 is the potential for voltage error. There is an intrinsic error in the ability of the amplifier to maintain a set voltage where $V_{error} = R_{series} \times I_{clamp}$. Thus a 1 nA current measured in a cell with 5 MΩ series resistance will produce a voltage error of 5 mV. While all our recordings were performed with series reisitance < 5 MΩ and series resistance compensation of at least 80%, in a worst-case scenario, a 10 nA current still produces up to 10 mV of voltage error. We minimized voltage-error in two additional ways: First, the majority of recordings of Kv2.1 or Kv2.1ΔC current were done in the presence of 20 mM external TEA, which blocks ~80% of the current through Kv2.1 (34). Secondly, we calculated the number of conducting channels from the peak tail currents at -40 mV where the last several tail current tracings had saturated due to complete activation in the previous depolarizing voltage steps from +40 to +60 mV. Relying on tail currents under conditions of maximal activation avoided the need to depend on a determined voltage-activation midpoint, which could be susceptible to voltage error. Together, these approaches allowed us to avoid currents greater than 3.4 nA while measuring conducting channel numbers > 78,000. It should be noted that despite the potential for voltage-error we have no evidence for such error in the cells used for our analysis. For example, activation mid-points determined by plotting peak tail currents against the previous step depolarization were +3.4 ±1.4 mV, n=21, while the midpoint calculated

from traditional G/Gmax plots was +13.5 ±1.4 mV, n=21. Both values are in close agreement with previously published values (22).

Calculation of endogenous Kv2.1 channel density in cultured hippocampal neurons. We began by calculating Kv2.1 channel density in non-clustered regions of GFP-Kv2.1 transfected HEK cells. Both the transfected HEK cells and cultured hippocampal neurons 14 or 20 DIV were fixed and immunolabeled simultaneously using the same carboxyl terminal monoclonal antibody (NeuroMabs). HEK cells for which channel densities had been calculated from the GFP fluorescence were re-imaged on a confocal microscope by capturing a single confocal section through the basal membrane. A ROI was drawn in precisely the same region as had been used to calculate channel density, and the average intensity per μm^2 was divided by the channel density to obtain the single channel immunofluorescence in arbitrary fluorescent units (A.U.). Immunolabeled neurons were imaged in the same manner, using the same parameters as with the transfected HEK cells. Neurons cultured for 14 and 20 DIV were handled separately and on different days, so each group was paired with a different set of HEK cells. Confocal sections through the basal membrane of each neuron were used to measure the immunofluorescence intensity of clusters and non-cluster regions. Clusters are defined as local accumulations of fluorescence at least 3-fold greater than the surrounding fluorescence (cluster fluorescence ranges from 3- to 10-fold brighter than non-clustered fluorescence, on a cell-to-cell basis). Automated object finding software (Volocity v6.0) was used to select and measure clusters. Five ROIs were drawn away from the clusters and averaged to measure non-clustered intensity and a single ROI drawn around the perimeter of the basal membrane was used to measure total intensity. Cells immunolabeled without the primary antibody were used to subtract non-specific fluorescence from labeled cells. Each of these measurements was divided first by the area each occupied in μm^2 and then by the single channel immunofluorescence to obtain endogenous Kv2.1 density (channels/μm^2). C_M was used to define the plasma membrane surface

area such that our comparison of current density and total channel number relies on the assumption that the measured C_M is an accurate measurement of membrane surface area. The mean C_M for DIV 14 neurons was 56.5±2.6 pF which is in agreement with other C_M measurement for pyramidal hippocampal neurons in culture (78). However, a rat postnatal day 14 (P14) freshly dissociated neuron cell body has a C_M of 14.3±3.8 pF (7), suggesting that much of the C_M can be attributed to the neurites and it is unclear how much electrical access exists into these compartments. Our assumption is that we can measure currents over the same membrane surface that the C_M measurement is derived from.

Our findings also rely on the assumption that immunolabeling performed at the same time with the same solutions will generate the same efficiency of antibody binding to Kv2.1 channels whether they are expressed in a HEK cell or a neuron. While we cannot be positive that the antibody binding efficiency is identical in HEK cells and neurons we can make other assumptions about the labeling efficiency. HEK cells have a simple geometry lacking extensive compartmentalization and are plated at low density providing space between each cell. Neurons instead have an extremely complex morphology and typically grow in dense networks of neuropil which could obstruct antibody access or lower the relative concentration of antibody. Thus if a difference in antibody labeling efficiency exists it is most likely to be in favor of labeling in HEK cells. This sort of a discrepancy would underestimate the number of Kv2.1 channels expressed endogenously in cultured hippocampal neurons and would only further support our conclusion that a significant non-conducting Kv2.1 population exists in neurons.

Image presentation and data analysis. Images were imported into Volocity 6.0 software for contrast enhancement, 3D reconstruction, object detection and quantitative analysis. Numerical data were exported into Origin Pro 8.5 for further analysis, curve fitting and figure preparation. Compilation of images was performed using Adobe Illustrator and contrast and brightness

adjustments were made. Both compressed (maximum projection) and single Z-section images are displayed as indicated.

Statistics. Data are presented as mean ± SEM. Statistical analysis was performed using an unpaired or paired t-test, with $p < 0.05$ considered statistically significant, as indicated in the figure legends.

Results

Kv2.1 partitions equally between clustered and non-clustered cell-surface domains in HEK cells. Using a combination of TIRF microscopy and laser scanning confocal microscopy we first determined the whole cell distribution of GFP-Kv2.1 in transfected HEK cells. Figure 1A shows a maximum projection confocal z-stack of an HEK cell transfected with an N-terminal GFP fusion of Kv2.1. These clusters are indistinguishable from endogenous Kv2.1 clusters in neurons (17). The mean intensity from the basal membrane of a randomly selected population of immunolabeled HEK cells transfected with Kv2.1 (497±26.4 A.U./pixel, n=15, data not shown) was only about 2-fold greater than that of endogenous Kv2.1 (255.4±36.3 A.U./pixel, n=11, data not shown) in DIV 20-22 neurons. Thus, Kv2.1 localization in HEK cells does not represent an over expression artifact. Figure 1B shows a TIRF image of the basal surface of a GFP-Kv2.1 expressing HEK cell where both clustered and non-clustered Kv2.1 expression is observed. We define clusters as having at least >3-fold fluorescence than the surrounding area although this ranges from 3- to 10-fold from cell-to-cell. In this particular cell the Kv2.1 clusters occupied 15% of the total footprint surface area and contained 5.4-fold greater fluorescence intensity than non-clustered membrane with 48% of the total fluorescence restricted to clusters. The average cluster intensity in this cell was 4938±123 A.U./pixel. The small standard error indicates that the density of channels within clusters is very consistent. Overall, the GFP-Kv2.1 clusters accounted for 20% of the basal surface area and 52±3.8% of the total fluorescence, while non-clustered GFP-Kv2.1

accounted for 45.6±3.3% of the total fluorescence (n=21). Thus the Kv2.1 clusters on the basal surface contain approximately an equal number of channels as compared to the non-clustered membrane.

The quantitation thus far considers only the basal surface of the cell directly in contact with the coverslip. Whether the clusters have a preference for the top or the bottom of the HEK cell was not known. To address this question, HEK cells expressing GFP-Kv2.1 were labeled with DiI to provide an unbiased measure of total membrane surface area following confocal imaging and 3D reconstruction. A representative 3D reconstruction from confocal z-sections illustrating the top and bottom of the same cell is shown in Figure 1C and 1D, respectively. Here the GFP-Kv2.1 clusters (green) are shown against total membrane labeled with DiI (red). Automated object finding (Volocity 6.0, Waltham, MA) was used to measure the volume of either the total membrane (DiI) or just the Kv2.1 clusters (GFP). The percent of membrane volume occupied by clusters in this cell was 14%. Overall, 19±1.7%, n=5, of the cell surface was cluster-occupied and there was no difference between the bottom of the cell and the whole cell (Figure 1E). Furthermore, the density of cluster GFP in Figure 1C&D was similar between clusters within the same cell and averaged 6.2±0.7-fold, n=5, greater than the density in the surrounding cluster-free membrane. The cluster intensity on the bottom of the cell (1524±250 A.U./pixel) tended to be greater than the whole cell (1136±78 A.U./pixel), but this difference was not significant (paired t-test, p=0.14, n=5) (Figure 1F). Thus, the TIRF image of the basal membrane shown in Figure 1B is representative of the entire cell surface.

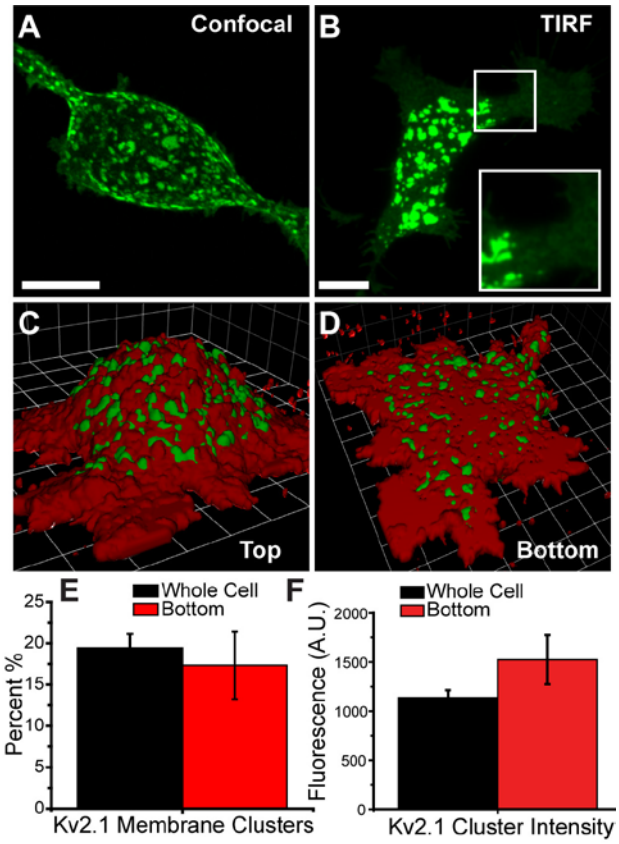

Figure 1. GFP-Kv2.1 localizes to dense cell-surface clusters in transfected HEK cells. A) Compressed (maximum projection) confocal z-stack of an HEK cell transfected with an N-terminal GFP fusion of Kv2.1. These clusters are indistinguishable from endogenous Kv2.1 clusters in neurons. B) HEK cell transfected with GFP-Kv2.1 and imaged using TIRF microscopy. The non-clustered population of Kv2.1, which is evenly distributed on the membrane, is more readily visible in TIRF (Inset: magnified and enhanced contrast of the white boxed ROI). Scale bar = 10 µm. C & D) Three-dimensional reconstruction of a HEK cell transfected with GFP-Kv2.1 and the plasma membrane stained with DiI as seen from the top (C) and bottom (D). Confocal z-stacks were reconstructed using Volocity software. Each grid = 5.29 µm. E) Graph comparing the percentage of basal membrane occupied by Kv2.1 clusters (19±2%, Red) to the percentage of membrane cluster-occupied at the whole cell level (17±3%, n=5, Black). Percentage of membrane occupied by Kv2.1 clusters was determined using an automated analysis in Volocity where total membrane volume was obtained from DiI labeling and Kv2.1 clusters were detected based on GFP fluorescence. F) Graph comparing the intensity of Kv2.1 clusters on the bottom of the cell (1520±250, Red) to those present over the cell as a whole (1140±80, Black), (paired t-test, p = 0.14).

Detection of individual GFP-tagged Kv2.1 channels in HEK cells. Our previous findings with on-cluster cell-attached patch clamp experiments indicate that Kv2.1 channels retained within clusters do not open in response to positive voltage steps in contrast to the non-clustered channels that behave like the archetypal Kv2.1 delayed-rectifier (69). However, there remains the question of whether a sub-population of non-conducting channels exists outside the Kv2.1 clusters. To address this issue we determined the number of Kv2.1 molecules within and outside the surface clusters and compared this Kv2.1 channel number to whole-cell current magnitude.

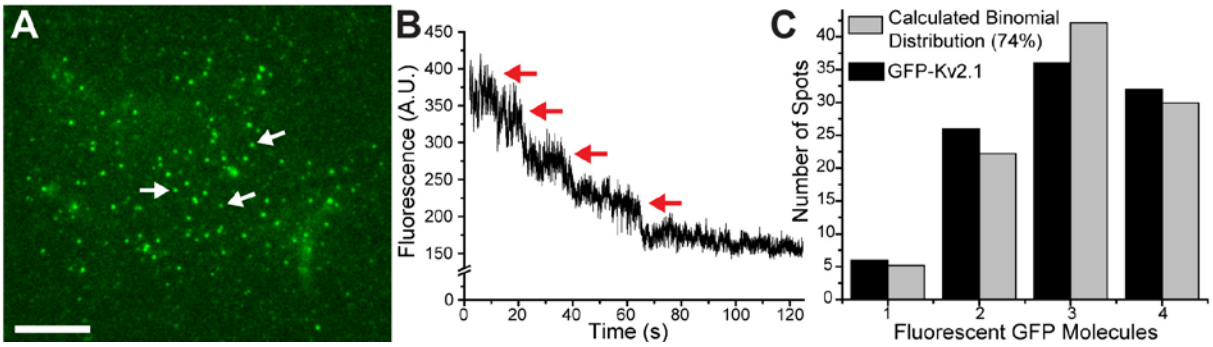

Figure 2. Step-wise bleach of individual GFP-Kv2.1 channels. HEK cells transfected with GFP-Kv2.1 were imaged using TIRF microscopy and captured with an EM-CCD camera. A) HEK cell expressing low numbers of GFP-Kv2.1 channels. White arrows point to discrete eGFP puncta associated with a single Kv2.1 channel. B) Graph of the fluorescence of a single GFP-Kv2.1 puncta over time. Photo-bleaching occurs in four discrete steps as indicated by the red arrows. C) Graph of the distribution of fluorescent GFP molecules per discrete fluorescent puncta (n=100) (Black Bars). The distribution of a binomial distribution (Grey Bars) assuming a GFP folding efficiency of 74% is presented for comparison. Scale bar = 10 μm.

Channel number can be calculated from the TIRF footprint of a GFP-Kv2.1 expressing HEK cell if the intensity of a single tetrameric GFP-Kv2.1 channel is known. TIRF-based photo-bleach was used to monitor the step-wise bleach of discrete fluorescent puncta during continuous illumination in the same manner used to determine subunit stoichiometry (75, 79). Since the tetrameric Kv2.1 contains up to four functional GFP molecules, the fluorescence should bleach over time in up to four distinct steps if a single channel molecule is imaged. We reduced the expression level of GFP-Kv2.1 to the point where only a small number of discrete spots were visible in TIRF illumination as illustrated in Figure 2A. The mobility of these puncta matched the single Kv2.1 channel diffusion characteristics previously reported (16, 80). To confirm that these spots represent single Kv2.1 channels, we plotted the fluorescence intensity of a single spot during constant high power illumination. The data show a clear four step decrease in intensity indicating that four GFP molecules are present in this diffraction limited spot (Figure 2B). Thus, the mean bleach step magnitude provides an estimate of the single GFP fluorescence under these imaging conditions. Comparison of single GFP fluorescence to the total fluorescence of 100 discrete GFP-Kv2.1 channels provided an estimate of the number of properly folded, and thus fluorescent, GFP molecules per channel. Single GFP-Kv2.1 channels frequently had either four (32%) or three (36%) functional GFP molecules. Less frequently two (26%) or one (6%) GFP molecules were detected as summarized in Figure 2C. This is consistent with an independent GFP folding efficiency of approximately 74%, and is in agreement with the measured folding efficiency in other fluorescent protein fusions (32, 75, 76). Thus, we can readily determine the fluorescence intensity of both single GFP molecules and tetrameric GFP-Kv2.1 channels in addition to the efficiency of GFP folding in the GFP-Kv2.1 fusion.

Measurement of GFP-Kv2.1 channel cell surface density using single channel fluorescence and TIRF microscopy. The single molecule fluorescence intensity values discussed above were next used to calculate Kv2.1 molecule density from the membrane GFP

fluorescence measured during TIRF imaging. However, in HEK cells expressing sufficient Kv2.1 channels to visualize the formation of clusters it was impossible to identify discrete GFP-Kv2.1 channels, necessitating the measurement of the single channel or single GFP intensity in a different cell. The intensity of the TIRF evanescent wave decays exponentially as the distance from the coverslip increases, meaning very small deviations in the distance between the cell and the coverslip are magnified into large differences in illumination and subsequent emission intensity (81). To control for variations in illumination intensity, we transfected cells with either high (3 μg) or low (0.5 μg) quantities of plasmid DNA and then plated these cells together in the glass bottom culture dishes used for TIRF imaging (Figure 3A). Assuming that adjacent cells have minimal variations in distance from the coverslip they will receive equivalent illumination. Single channel fluorescence measurements were made from cells expressing low numbers of GFP-Kv2.1 channels and the single channel fluorescence (white arrows, Figure 3A), was used to calculate channel density (channels/μm^2) in an adjacent cell expressing a much greater number of channels (red arrow, Figure 3A). In this manner every Kv2.1 surface density determination had its own internal standard. Cells were selected based on fluorescence intensity to encompass the entire spectrum of expression levels. This quantitation was performed in conjunction with K^+ current density measurements via whole cell voltage-clamp of the same cell being imaged for the fluorescence-based channel density determination.

Estimation of GFP-Kv2.1 conducting channel number using whole-cell K+ current amplitude. Calculating the absolute number of conducting Kv2.1 channels in transfected HEK cells requires an accurate measurement of the total whole-cell current, the single channel conductance and the opening probability (P_O) at the membrane potential used. The single channel conductance of Kv2.1 has been extensively studied (82) and was calculated to be 6.15 pS in 5 mM external K^+, while the maximum P_O was 0.7 (83).

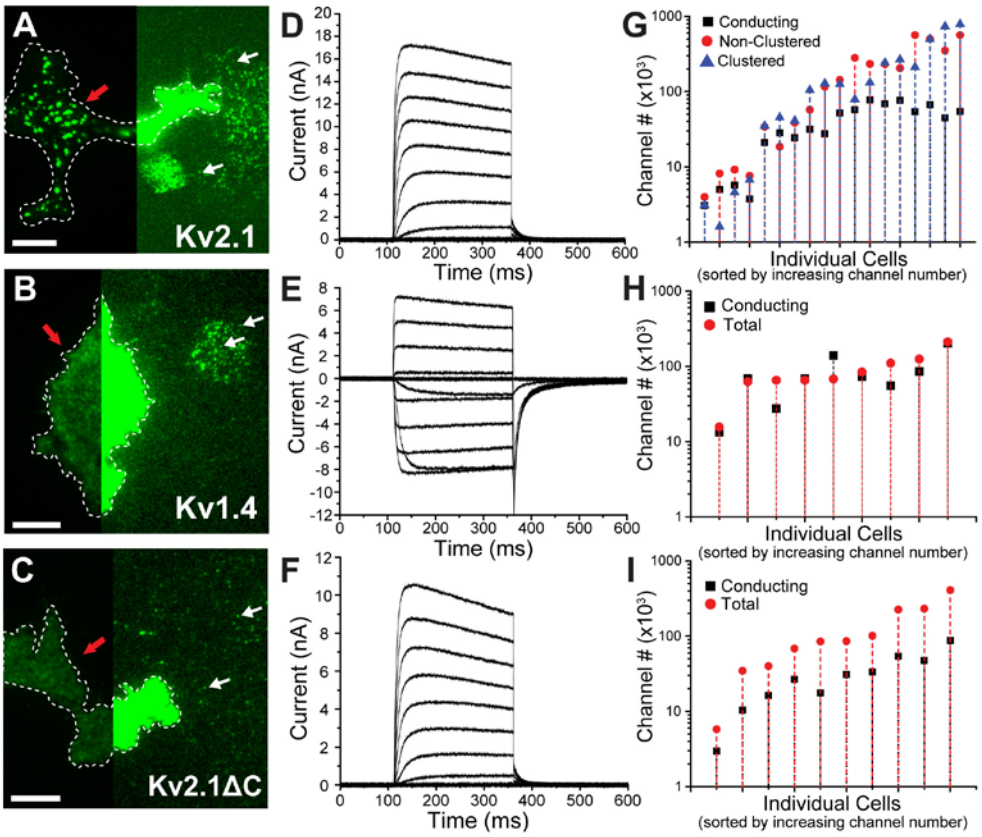

Figure 3. Simultaneous TIRF imaging and whole-cell voltage clamp. A-C) HEK cells were transfected with high and low concentrations of Kv2.1 (A), Kv1.4 (B) or Kv2.1ΔC (C) GFP fusions and plated together to achieve both expression levels in one field of view (each panel has two transfected cells, side by side). Cells used for voltage-clamp (Red Arrows) were too bright to discern single GFP-tagged channels. The contrast in the right half of each image was enhanced so single GFP-tagged channels (White arrows) from an adjacent cell expressing a low number of channels were visible. D-F) Whole-cell voltage clamp recordings of Kv2.1 (D), Kv1.4 (E) and Kv2.1ΔC (F) in response to 250 ms voltage steps ranging from +60 to -60mV (+40 to -80 mV for Kv1.4) in 10 mV increments. Following each voltage step, tail currents were measured at -40mV (Kv2.1 & Kv2.1ΔC) and -60 mV (Kv1.4) to assess channel activation. The high external K^+ solution used to record Kv1.4 currents causes the reversal potential to shift to ~+7 mV. G) Quantification of non-clustered (circle), clustered (triangle), and conducting (square) Kv2.1 channel number for individual cells sorted by increasing channel number. Note the log scale for the Y-axis. H & I) Quantification of total (circle) and conducting (square) channel number for Kv1.4 (H) and Kv2.1ΔC (I). Individual cells are sorted by increasing channel number. Note that the number of total and conducting channels are consistently similar (1.24±0.16, n=9) for Kv1.4, while total channel number is in excess relative to conducting Kv2.1 and Kv2.1 ΔC number. Scale bar = 10 μm.

Whole-cell currents in voltage clamp were measured during 250 ms step depolarizations from a holding potential of -80 mV to +60 mV in 10 mV increments (Figure 3D). Deactivating tail currents were recorded at -40 mV. The level of expression required to visualize cluster formation in HEK cells that mimics that of the endogenous channel in hippocampal neurons results in whole cell K^+ currents >10 nA in amplitude. Therefore, recording accurate whole cell currents for Kv2.1 under conditions favoring cluster formation is difficult due to high peak current levels in addition to the series resistance/voltage error concerns. The primary concern is that these current levels can result in a loss of voltage control since the active outward flow of K^+ ions at depolarized potentials tends to hyperpolarize the actual membrane potential relative to the command potential. Collapsing the transmembrane K^+ gradient by elevating extracellular K^+, and thus reducing the driving force and current magnitude, was not a viable option since Kv2.1 single channel conductance increases with increasing extracellular K^+ (82). Voltage error was minimized by using only cells with a total access resistance < 5 MΩ and by careful use of 80-90% series resistance compensation. We further reduced potential voltage clamp error in two ways. First, the vast majority of recordings were made in the presence of 20 mM TEA to block 78±4% (n=4, data not shown) of the whole cell current, consistent with previous reports (34). Second, in our data analysis to calculate conducting channel number we used the peak tail current measured at -40mV, a potential where the K^+ currents are smaller due to reduced driving force and variations in activation midpoint are not significant as maximal activation has been achieved. Using these approaches allowed us to detect up to 78,000 conducting channels per cell without relying on whole-cell K^+ current amplitudes over 3.4 nA. Thus, for a given cell we were able to measure the Kv2.1 channel density within clusters and outside clusters based on GFP fluorescence while in the same cell simultaneously calculating total conducting channel number based on current measurements under whole-cell voltage clamp. For each cell, channel densities obtained from the TIRF-derived basal membrane GFP fluorescence were extrapolated to account for the entire cell membrane using the membrane capacitance measurements (C_M) obtained during voltage

clamp in conjunction with the measurements of the Kv2.1 cluster distribution obtained in Figure 1.

The percentage of non-conducting Kv2.1 channels is highly variable. Figure 3G compares the number of Kv2.1 channels on individual HEK cell surfaces in either clusters (triangle) or non-cluster membrane (circle) (as obtained from the GFP fluorescence illustrated in Figure 3A) to the whole cell currents (square) (shown in Figure 3D). Individual cells (n=21) are sorted by increasing total channel number and symbols along each vertical line represent measurements from the same cell. Overall, the average number of conducting channels was 39,000±6,000 while there were 187,000±46,000 non-clustered and 191,500±57,000 clustered Kv2.1 surface molecules (n=21). These data indicate that the majority of Kv2.1 channels are held in a non-conducting state. As illustrated in Figure 3G this trend does not hold for every cell since at the lower expression levels there is closer agreement between the number of non-clustered channels and the K^+ current. However, as the expression level increases, only a fraction of the non-clustered channels can be conducting. At the highest expression levels the number of conducting channels appears to saturate, perhaps indicating an absolute limit of channel conductance (Figure 3G). There was no relationship between the levels of GFP-Kv2.1 expression and the activation midpoint measured from tail currents (mean = +3.4±1.4 mV, n=21, data not shown). Our original hypothesis predicted a good agreement between non-clustered and conducting channel values whereas clustered channel numbers were expected to have no relationship to either. Instead, we found that high expression levels decreased the percentage of non-clustered channels conducting K^+.

Non-conducting state of GFP-Kv2.1 is density dependent. Figure 4A summarizes the relationship between expression density and channel conductance for the wild-type Kv2.1. Here the conducting ratio, obtained by dividing the number of total Kv2.1 channels by the number of

conducting channels, is plotted against Kv2.1 plasma membrane expression density in the same cell. A ratio of one indicates that all expressed channels are functional, while a ratio of two indicates that half of the expressed channels are non-conducting. Figure 4A illustrates that as the total density of channels increases there is a clear trend toward greater ratios, indicating that there is indeed an effect of expression level on the non-conducting state. Figure 4B plots the conducting ratio for only non-clustered channels against the expression density of those channels. The trend here again indicates that the density of non-clustered channels determines what fraction of these channels is non-conducting. Since the conducting ratio approaches one at the lower expression levels, most of the non-clustered channels are conducting. In summary, the non-conducting state of Kv2.1 is dependent on the density of channel expression regardless of whether or not the channels are located within a cluster microdomain.

Kv1.4 conductance is not affected by channel density. To assure that the density dependent non-conducting state observed for GFP-Kv2.1 was not related to unknown error in our channel counting technique we performed the same analysis on HEK cells transfected with GFP-Kv1.4. Unlike Kv2.1, GFP-Kv1.4 has unrestricted mobility on the cell surface and a homogeneous surface localization (16). Therefore, we measured the GFP density from a ROI encompassing the entire TIRF footprint (Figure 3B). Since Kv1.4 is insensitive to TEA (IC_{50} > 100 mM), we altered the potassium gradient (150 mM K^+ outside/100 mM K^+ inside) to minimize whole-cell current amplitude (Figure 3E) and ensure proper voltage control (84). Much like Kv2.1, Kv1.4 is modulated by external potassium. However, unlike Kv2.1, increasing external potassium increases the open probability (P_O) of the Kv1.4 channel and not the single channel conductance with P_O reaching a maximum of 0.8 in the presence of 100mM external K^+ (85). The voltage-step protocol to generate currents was similar to that used for Kv2.1, and the peak tail current amplitude measured at -60 mV was used to calculate conducting channel number.

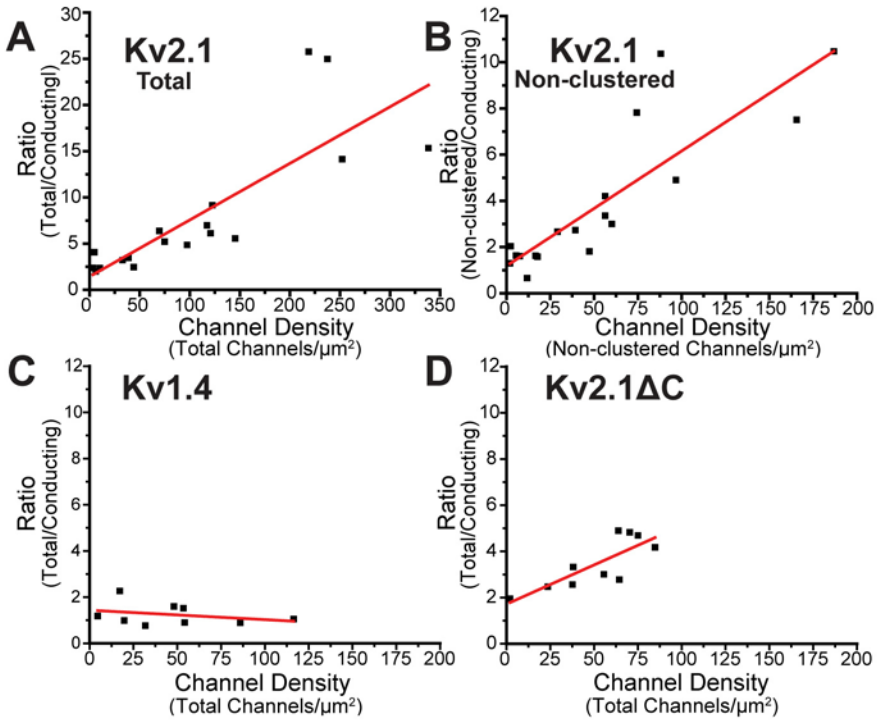

Figure 4. The fraction of Kv2.1 non-conducting channels increases as channel density increases. A) Ratio of total Kv2.1 channel molecules (calculated from single channel fluorescence) to conducting channels (calculated from whole-cell currents) plotted as a function of total channel density (Intercept = 1.44, R^2=0.65). B) Ratio of non-clustered channel number to conducting channels plotted as a function of non-clustered channel density (Intercept = 1.18, R^2=0.72). C&D) Ratio of total Kv1.4 (C; Intercept = 1.72, R^2=0.6) and Kv2.1ΔC (D; Intercept = 1.43, R^2=-0.04) channel number to conducting channels plotted as a function of total channel density. For Kv2.1 (A&B) and Kv2.1ΔC (D) the ratio increases as density increases, while for Kv1.4 (B) the ratio remains roughly 1:1 at all densities measured. Red lines are linear fits using the equation y = a + b*x.

Nearly identical conducting channel numbers were also calculated when using the slightly smaller outward currents generated at either +30 or +40 mV, potentials where channel activation is maximal. The relationship between Kv1.4 channel number and conductance is summarized in Figure 3H which shows consistent agreement between channel number based on GFP fluorescence and channel number based on current. The mean conducting ratio for Kv1.4 was 1.24±0.16 (n=9) indicating there is no significant non-conducting population of Kv1.4 channels. The plot of conducting ratio against channel density shown in Figure 4C demonstrates that for all individual cells the conducting ratio is approximately one, regardless of the expression level. In summary, when we apply the channel counting technique to a Kv subunit for which there is no previous evidence of a large non-conducting population we obtain nearly perfect agreement between conducting channel number and expressed channel number.

Kv2.1 non-conducting state is independent of both clustered localization and the channel carboxyl terminus. While the Kv2.1 non-conducting state originally appeared related to cluster localization (69), the summary shown in Figure 4B suggests this localization per se is not responsible for the lack of channel activity. Domains in both the amino and carboxyl termini of Kv2.1 are necessary for its localization to clusters (Lim et al., 2000; Mohapatra et al., 2008). While the most critical residues have been mapped to the proximal regulation of clustering domain (PRC) on the carboxyl terminus, removal of the entire carboxyl terminus is a simple way to eliminate cluster localization (26). As illustrated in Figure 3C, a mutant Kv2.1 in which the last 318 amino acids were deleted (GFP-Kv2.1ΔC) fails to form the classic Kv2.1 clusters. Since GFP-Kv2.1ΔC is localized diffusely over the membrane surface we measured channel density from a single ROI encompassing the entire TIRF footprint as was done for GFP-Kv1.4. Figures 3I and 4D summarize the relationship between channel number and current. Even at the lowest expression level only half of the GFP-Kv2.1ΔC channels are conducting, much like the total population of wild-type GFP-Kv2.1. As the expression of GFP-Kv2.1ΔC increases there is a

concomitant increase in the percentage of non-conducting channels, however, the slope of this relationship (0.034±0.01, n=9) is roughly half that of wild-type GFP-Kv2.1 (0.061±0.01, n=21). Aside from the absence of clusters with the GFP-Kv2.1ΔC channel, the most notable difference from the wild-type channel is the maximum channel density. The highest channel density measured for the GFP-Kv2.1ΔC channel was 85 channels/um^2, less than half the highest density of non-clustered GFP-Kv2.1 (187 channels/um^2). It is not surprising that GFP-Kv2.1ΔC was unable to achieve surface expression levels equal to GFP-Kv2.1 given the role of the carboxyl terminus in efficient trafficking (Mohapatra et al., 2008). The lower cell-surface expression of GFP-Kv2.1 ΔC may explain why the percentage of non-conducting channels is less than in cells expressing the wild-type GFP-Kv2.1. Furthermore, this is consistent with a density-dependent mechanism underlying generation of the non-conducting state. These data obtained with the GFP-Kv2.1ΔC channel suggest that neither retention within a cluster nor the carboxyl terminal tail of Kv2.1 is required for the non-conducting state. This is consistent with a recent report which demonstrates that while the carboxyl terminus of Kv2.1 is necessary for clustered localization it is dispensable with respect to modulation of channel function (86). Together the data summarized in Figures 3 and 4, argue that 1) the functional state of Kv2.1 is related to the membrane density, 2) the non-conducting state of Kv2.1 is not a direct consequence of cluster residence and 3) density dependent regulation of Kv2.1 does not involve the C-terminal 318 amino acids.

Non-conducting Kv2.1 channels reside on the cell surface. While TIRF microscopy is an excellent method for observing fluorescence at or near the PM it does not exclude intracellular sources of fluorescence from near-membrane organelles, such as docked trafficking vesicles and cortical endoplasmic reticulum. Although TIRF measurements of GFP-Kv2.1 channel density were carefully made to avoid intracellular fluorescence as discussed in the methods section, we sought to confirm our previous results using a true cell-surface fluorophore. We expressed GFP-Kv2.1-HA, which contains a hemaglutinin (HA) epitope engineered into the S1-S2 extracellular

loop (71), in HEK cells and labeled with an anti-HA antibody conjugated to AlexaFluor594. In Figure 5A there is excellent overlap between GFP and Alexa594 and this is especially noticeable in the clusters. Upon closer examination, there are a few GFP spots which do not label with Alexa594 (Fig. 5A, white arrows). These spots are very likely mobile trafficking vesicles which we have observed previously (51) and importantly only account for ~0.4% of the total GFP fluorescence of the TIRF footprint in this cell (data not shown). In Figure 5B, the fluorescence intensity of GFP and Alexa594 from the TIRF footprint of 147 HEK cells transfected with GFP-Kv2.1-HA is shown. While there is significant spread of the intensities, indicating variability in the labeling efficiency from cell to cell, there is a consistent linear trend over the entire range of GFP intensities used in the previous experiments. This rules out the possibility of an intracellular buildup of GFP-Kv2.1-HA at higher expression levels, since this would cause an increase in GFP intensity without a concomitant increase in Alexa594 intensity, causing the scatter plot to plateau.

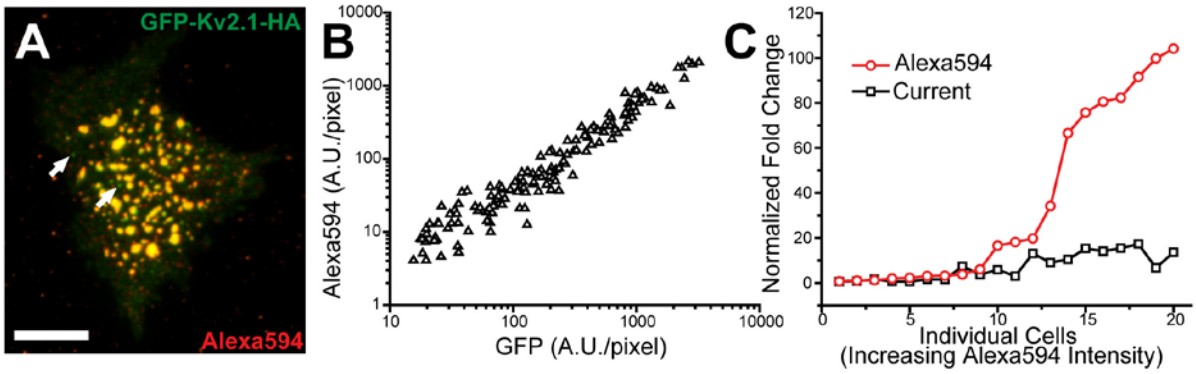

Figure 5. Non-conducting Kv2.1 channels reside on the cell surface. A) HEK cell expressing GFP-Kv2.1-HA and labeled with an anti-HA antibody conjugated to AlexaFluor594 (1:1000). White arrows point to unlabeled GFP spots which are likely intracellular vesicles and account for ~0.4% of the total GFP fluorescence from the TIRF footprint. Scale bar = 10μm. B) The GFP and Alexa594 intensity from 147 cells is plotted. The relationship is linear over the range of GFP intensities used in this study. C) Whole-cell current and Alexa594 intensity were measured for 20 cells spanning a large range of expression levels and normalized to the average of the three lowest expressing cells. At higher expression levels there is a much greater fold-increase in Alexa594 than whole-cell current.

Since there is a linear relationship between GFP-Kv2.1-HA expression and Alexa594 labeling, we used the Alexa594 intensity alone to corroborate our previous results. It is unlikely that Alexa594 labels GFP-Kv2.1-HA channels with 100% efficiency, so we cannot use this fluorophore to directly calculate channel density. Instead we preformed paired TIRF imaging and voltage-clamp of individual cells spanning a large range of expression levels and then normalized each cell to the average of the three cells with the lowest expression levels. In Figure 5C, normalized whole-cell current and normalized Alexa594 increase concomitantly at the lower expression levels (cells sorted left to right based on Alexa594 intensity). At higher expression levels, very large Alexa594 fold intensity increases are contrasted by very small fold increases in whole-cell current. These data agree with the trend shown in Figures 3 & 4, that at high expression levels an increasing proportion of Kv2.1 channel are non-conducting.

Calculation of endogenous Kv2.1 channel density in cultured hippocampal neurons. HEK cells provide an ideal expression system in which to study Kv2.1 due to the neuron-like cell-surface expression pattern after Kv2.1 transfection and the lack of endogenous Kv2.1. However, a HEK cell cannot replicate the entire milieu of neuronal proteins or the complex regulation a neuron exerts over those proteins. Therefore, it was important to determine whether the endogenous neuronal Kv2.1 channels also possess the non-conducting state. In order to characterize the cell surface distribution of the endogenous Kv2.1 channel in cultured hippocampal neurons the plasma membrane was first labeled with FITC-conjugated wheat-germ agglutinin to provide an unbiased measure of the soma and proximal dendrites over which Kv2.1 clusters were detected. Following fixation and detergent permeabilization Kv2.1 was detected using a monoclonal antibody directed against an epitope within the C-terminus and an AlexaFluor-594-conjugated secondary antibody. 3D reconstructions from confocal z-sections are shown in Figures 6A and 6B. The endogenous Kv2.1 clusters occupied 19.5% of the soma membrane in this particular neuron, and the immunolabeling within the clusters was 3.95-fold greater than the

surrounding membrane. Overall, in the five cells examined 19.0±2.5% of the soma was cluster occupied with an average density 3.7±0.5-fold greater than the adjacent membrane (n=5). While the clusters did occupy a significantly smaller percentage of the basal cell membrane as compared to the rest of the soma (Figure 6C), the intensity of the clusters was the same over the entire cell surface (Figure 6D). These data clearly demonstrate that HEK cells faithfully reproduce the localization of endogenous Kv2.1 in cultured neurons.

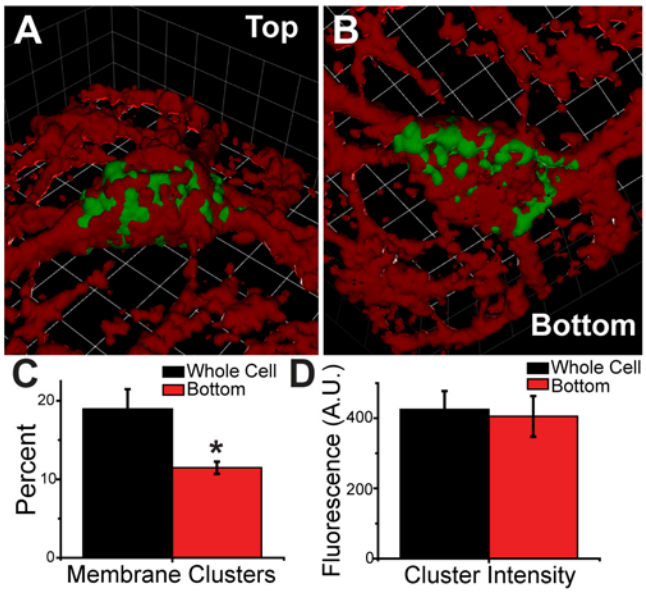

Figure 6. Three-dimensional reconstruction of Kv2.1 plasma membrane distribution in cultured hippocampal neurons. A & B) 14 Days in Vitro (DIV) embryonic day 18 (E18) rat hippocampal neuron stained with wheat germ agglutinin (WGA) (Red), fixed and immunostained for Kv2.1 (Green). Confocal z-sections were reconstructed in three dimensions using Volocity software. Each grid = 4.21 µm. C) Comparison of the percentage of membrane occupied by Kv2.1 clusters from the bottom of the cell (12±1%, n=5, Red) to the whole cell (19±3%, Black, ***** = $p<0.05$). Percentage of membrane occupied by Kv2.1 clusters was determined using an automated analysis in Volocity where total membrane volume was obtained from WGA labeling and Kv2.1 clusters were detected based on antibody fluorescence. Intracellular fluorescence was removed to within 1 µm of the membrane for both labels prior to automated analysis. D) Comparison of the intensity of Kv2.1 clusters on the bottom of the cell (410±60, Red) to the whole cell (420±50, Black).

Next, we developed a method to quantify the endogenous expression of Kv2.1 in cultured hippocampal neurons (Figure 7A). We began by using TIRF microscopy to measure the single channel fluorescence intensity of GFP-Kv2.1 in HEK cells and used this to calculate channel density (channels/μm^2) essentially as described in previous sections (Figure 7B). These HEK cells were fixed and immunolabeled for Kv2.1 alongside cultured hippocampal neurons either 14 or 20 days *in vitro*. A confocal microscope was used to image anti-Kv2.1 immunolabeling of HEK cells which had previously been imaged using TIRF microscopy (Figure 7C). The immunofluorescence density (A.U. /μm^2) of a non-clustered region was divided by the Kv2.1 channel density (channels/ μm^2) from the same region to calculate the equivalent of single channel immunofluorescence (A.U./channel). Transfected HEK cells handled in this way were processed and imaged alongside groups of neurons, either 14 or 20 DIV, so that each neuron group had an internal HEK-based control for Kv2.1 immunofluorescence. In cultured hippocampal neurons, a single z-section through the bottom of the cell was used to measure Kv2.1 immunofluorescence from both clustered and non-clustered regions, as well as a single ROI encompassing the entire footprint of the cell to measure total immunofluorescence (Figure 7D). Each measurement was divided by the equivalent of single channel immunofluorescence to calculate the density of endogenous Kv2.1. The values for the endogenous Kv2.1 density obtained in the manner described above are summarized in Table 1. Thus, by comparing relative Kv2.1 immunofluorescence intensity between transfected HEK cells and cultured hippocampal neurons we obtain a reasonable estimate of the endogenous Kv2.1 membrane density inside and outside the cluster perimeter.

Endogenous Kv2.1 in hippocampal neurons demonstrates the non-conducting state.

Whole-cell electrophysiology was used to measure endogenous K^+ currents from neurons in culture for 14 and 20 days prior to the immunolabeling described above.

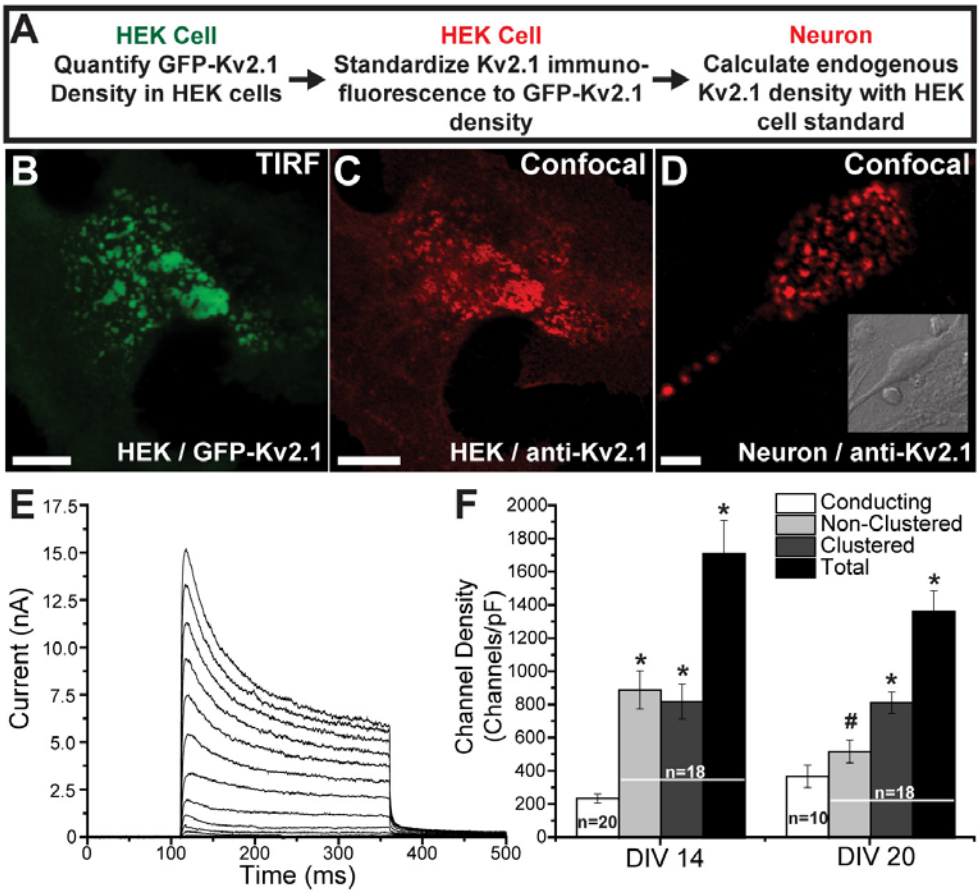

Figure 7. Calculation of endogenous Kv2.1 channel number in rat hippocampal neurons and comparison to Kv2.1 channel number estimated by voltage clamp. A) A flowchart of the protocol used to measure endogenous Kv2.1 channel number in neurons. B) HEK cell transfected with GFP-Kv2.1 was imaged in TIRF and the single channel GFP intensity was used to calculate channel density within a non-clustered region. C) The same cell following fixation and immuno-labeling for Kv2.1 (Red) then re-imaged with a confocal microscope. Antibody-derived fluorescent intensity was measured and divided by channel density determined in (A) to calibrate the immuno-staining to Kv2.1 channel number. D) DIV 14 rat hippocampal neuron immunolabeled for Kv2.1 alongside transfected HEK cells with a DIC image inset. Endogenous Kv2.1 density of clustered, non-clustered and total regions was calculated using transfected HEK cells (B & C) as a standard. E) Whole-cell voltage clamp recording from an embryonic day 18 rat hippocampal neuron, 14 days *in vitro* in response to 250ms depolarizing voltage steps from +60 to -60 mV in 10 mV increments. Ik_{DR} was measured 125 ms after the depolarization to +40mV to eliminate fast inactivating potassium currents and to avoid any Kv2.1 inactivation. (F) Kv2.1 channel density on DIV 14 and DIV 20 as estimated using both immunofluorescence (Non-clustered, Clustered and Total channel density) and whole cell current magnitude (Conducting channel density). ***** = $p<0.05$ compared to Conducting Kv2.1 channel density; # = $p<0.05$ compared to DIV 14. Scale bar = 10µm.

Kv2.1 is reported to mediate between 50-80% of the delayed rectifier current in principal neurons of the hippocampus and cortex (9, 10, 70). Both cell ages showed inactivating A-type current superimposed on the delayed rectifier as illustrated in Figure 7E. Stromatoxin (ScTx), a gating modifier which shifts the activation midpoint of Kv2.1 by +60 mV (7), blocked the Ik_{DR} at +40 mV by ~47% at 14-15DIV and by ~46% at 20-21DIV, indicating at least half of Ik_{DR} was mediated by Kv2 subunits under our culture conditions. Since the dose of ScTx used here only blocks 75-80% of Kv2 channel at +40mV (70), for our calculations we conservatively increased of the contribution of Kv2 to Ik_{DR} to 60% for both timepoints. Peak Ik_{DR} was measured 125 ms after the beginning of a +40 mV step depolarization to eliminate rapidly inactivating K^+ currents and tail currents were monitored to ensure that the delayed rectifier Kv currents had attained maximum activation. We then estimated the number of conducting Kv2.1 channels by dividing 60% of the Ik_{DR} by the single channel current. Finally, we divided the number of conducting channels by the measured whole cell capacitance (C_M) to estimate conducting channel surface density.

As summarized in Figure 7F, the density of conducting Kv2.1 channels was 228±27 channels/pF at 14 DIV, and 361±67 channels/pF at 20 DIV. The apparent increase in conducting channel density between DIV 14 and 20 was not significant (p=0.09). In contrast, there were 1,708±200 and 1,360±120 total Kv2.1 channels/pF based on the standardized immunolabeling at 14 and 20 DIV, respectively. Thus, the data suggest that at both maturity levels there was a large population of expressed channels that were not conducting K^+. If we assume all clustered channels to be non-conducting, on 14 DIV only one in three non-clustered channels would need to be conducting in order to generate the observed currents. On 20 DIV roughly two-thirds of the non-clustered channels would need to be conducting since at this age a greater percentage of the Kv2.1 resides within the cluster microdomains. Regardless, there is a clear overabundance of total Kv2.1 surface channel in relation to current at both neuronal ages. These data also suggest that in

neurons a portion of non-clustered channels are held in a non-conducting state, which is consistent with our findings in transfected HEK cells at the higher expression levels.

Table 1. Quantification of endogenous conducting and non-conducting channel number in cultured hippocampal neurons.

	DIV 14	DIV 20
Current Ik_{DR} @ +40mV (pA)	10,890±1,224 (n=20)	16,308±1,761 (n=10) #
Conducting Kv2.1 Channels	12,965±1,457 (n=20)	19,414±2,096 (n=10) #
Surface Area (μM^2)	5,200±250 (n=20)	5,665±714 (n=10)
Clustered Channels	48,313±4,847 (n=18) *	50,712±4,122 (n=18) *
Non-Clustered Channels	50,265± 6,469 (n=18) *	33,059±5,058 (n=18) *, #
Total Channels	96,578±11,317 (n=18) *	85,891±8,815 (n=18) *
Conducting Channel Density (#/pF)	228±27 (n=20)	361±67 (n=10)
Clustered Channel Density (#/pF)	819±104 (n=18) *	813±63. (n=18) *
Non-clustered Channel Density (#/pF)	889±114 (n=18) *	519±69 (n=18) #
Total Channel Density (#/pF)	1709±200 (n=18) *	1360±125 (n=18) *

Kv2.1 immunofluorescence was measured in cells fixed and immunolabeled using a C-terminal Kv2.1 primary antibody (K99/14, NeuroMabs, Davis, CA) and a Alexa 594 conjugated secondary antibody (Invitrogen, Carlsbad, CA). Alexa 594 fluorescence was converted to channel density using immunolabeled GFP-Kv2.1 expressing HEK cells as a standard. Whole-cell electrophysiology was used to measure Ik_{DR} 125 ms after step depolarizations to +40 mV. 60% of the delayed rectifier current (Ik_{DR}) was attributed to Kv2.1 and this was converted to channel number using the single channel conductance. Channel density was calculated by dividing channel number by the average whole-cell capacitance (C_m). Neuronal surface area was derived from whole cell capacitance. (* = $p<0.05$ compared to Conducting Kv2.1, # = $p<0.05$ compared to DIV 14).

Discussion

This study further examines the relationship between cluster localization and channel function, specifically asking whether non-conducting channels also exist outside the cluster microdomains. Previous work showed that the Kv2.1 channels restricted to clusters do not conduct K^+ in response to even excessive depolarization and that whole-cell currents were derived from the non-clustered, freely diffusing channels (69). A second goal was to determine whether a percentage of the endogenous Kv2.1 in cultured hippocampal neurons also exists in a non-conducting state. We report here that both transfected HEK cells and neurons typically express up to 6-fold more Kv2.1 channels than measured by whole cell voltage-clamp and that non-conducting channels are present outside of cluster microdomains. Because the number of clustered and non-clustered channels is similar, up to 66% of the non-clustered channels must be non-conducting. Importantly, since the endogenous Kv2.1 channel number in cultured hippocampal neurons far exceeds the number predicted by the whole cell ionic current, the non-conducting state is not an artifact of heterologous expression in HEK cells. It is important to keep in mind that the calculations of channel number are based on a number of assumptions and accordingly should be viewed as a best possible estimate. Detailed discussions of the assumptions and limitations are included in the methods section.

Density dependence of the non-conducting state. In HEK cells the proportion of non-clustered channels held in the non-conducting state was strongly associated with channel membrane density. At low densities (1-20 channels/μm^2) virtually every non-clustered channel conducted K^+. As non-clustered densities increased, the fraction of non-clustered channels that were non-conducting grew steadily to 83%. Furthermore, we see the same trend with the mutant Kv2.1ΔC which does not form classic clusters. These data strongly suggest that cluster residence itself is not the cause of the non-conducting state, but rather the high concentration of channels

in this restricted space where there is a 5-10-fold greater density than outside the clusters. Interestingly, a relationship between membrane density and function is not restricted to Kv2.1, for Kv1.2 and Kv3.1 channels show altered biophysical properties with increasing expression levels in *Xenopus* oocytes (87, 88). Density-dependent function has also been reported for ligand-gated channels such as the $P2X_2$ receptor (89).

Mechanism underlying the non-conducting state. The mechanism for the establishment of the non-conducting state remains unknown. Interestingly, carbon monoxide and hypoxia rapidly down-regulate Kv2.1 currents without affecting the voltage-dependence of activation and these interventions could be enhancing the non-conducting population (36, 37). The extensive regulation of Kv2.1 voltage-dependence by serine and threonine phosphorylation primarily in the carboxyl cytoplasmic termini has been well studied by Trimmer and coworkers (28). More recently, Kv2.1 has been reported to be sumoylated, with sumoylation inducing a leftward shift of activation midpoint (32). While there is no evidence that these post-translational modifications induce a non-conducting state, they are nonetheless excellent candidates, for it is easy to imagine that the proper combination of phosphorylation or dephosphorylation events could uncouple membrane depolarization and channel activation. Why does channel conductance decrease as expression density increases? Perhaps with increasing expression a channel component or modification becomes rate-limiting at the cell surface.

The non-conducting state in HEK cells versus neurons. Whatever the mechanism inducing the non-conducting state, it appears to be, not surprisingly, more efficient in the cultured hippocampal neurons as compared to HEK cells. The K^+ current density in a randomly selected population of transfected HEK cells (2144±343 pA/pF, n=13, data not shown) was roughly 10-fold greater than DIV 20-22 neurons (204.7±22.9 pA/pF) even though the density of Kv2.1 in transfected HEK cells (497±26.4 A.U./pixel, n=15, data not shown) is only 2-fold greater than DIV

20-22 neurons (255.4±36.3 A.U./pixel, n=11, data not shown) based on immmunolabeling. In addition, while DIV 7 neurons transfected with Kv2.1 express almost 3-fold more channel (1217±214 A.U., n=4, data not shown) than transfected HEK cells, the K^+ current density is less in the transfected neurons (1377±239 pA/pF, n=6, data not shown) as compared to HEK cells (2144±343 pA/pF, n=13, data not shown). This difference in the relationship between channel expression and current in HEK cells versus neurons, namely that with similar levels of expression HEK cells produce more K^+ current, suggests that HEK cells are not as efficient as neurons with respect to induction of the non-conducting state.

Further evidence for non-conducting Kv2.1 channels. Past research has indirectly argued for a significant percentage of Kv2.1 to be playing a non-conducting role. Abundant expression of endogenous Kv2.1 is found in vascular smooth muscle where it provides a hyperpolarizing influence on the resting membrane potential (41). However, while Kv2.1 is the easiest Kv channel to detect in the vasculature via western blot analysis (90), Kv2.1 currents in vascular smooth muscle myocytes are only 100-200 pA in magnitude (41). Kv2.1 cDNA expresses well and traffics efficiently to the cell surface in heterologous expression systems and neurons as you would expect for a structure protein but not a K^+ channel. By comparison many Kv channels are poorly delivered to the cell surface with up to 90% of the protein remaining trapped within the cell, most likely in the ER (52). This low surface expression is understandable given that too high a membrane density will electrically silence the cell. In contrast, perhaps high levels of Kv2.1 are allowed to reach the surface considering most of the channel will be non-conducting.

Physiological significance of the non-conducting state. Why is Kv2.1 expressed at high membrane densities where the majority of channels are non-conducting? While it is indeed plausible that the non-conducting channels serve as a channel reservoir waiting to be activated by some stimulus, that stimulus has remained elusive (69). Instead it appears that Kv2.1 has

developed an accessory function which requires an abundant supply of channel protein. Because normal neuronal function would be hindered unless there was a mechanism to silence channel conduction the evolution of the non-conducting state was essential. Recent work by ourselves and others has demonstrated that non-conducting Kv2.1 likely plays a role in SNARE protein-based vesicular trafficking (25, 47), and that Kv2.1 clusters are sites for delivery of Kv channels, and perhaps other membrane proteins, to the cell surface (51). Thus, it appears that Kv2.1 has taken on functions independent of a role in controlling membrane potential. This atypical, non-channel function likely requires a high level of expression as might be expected of a structural or scaffolding protein. Thus, the Kv2.1 non-conducting state may be a necessary property of the channel, allowing it to serve multiple functions at the cell surface without compromising electrical signaling.

Chapter 3: Induction of stable endoplasmic reticulum/plasma membrane junctions by Kv2.1 potassium channels.

Introduction

The endoplasmic reticulum (ER) is the most extensive membranous organelle, containing a single, continuous lumen and stretching from the nuclear envelope to the cell cortex in a system of tubules and sheets (cisterns) (54). The ER participates in close connections, or membrane contact sites (MCS), with nearly every other membranous organelle (61). MCS between the ER and plasma membrane (PM), i.e., ER/PM junctions, are particularly important for signal transduction, since most intercellular signals originate at the PM and the ER is a Ca^{2+} store involved in both the initiation and termination of intracellular signaling (66). The ER membrane is also a site of lipid synthesis and other enzymatic activity that can act across the membrane junction, and potentially transfer lipids between membranes (91, 92). ER/PM junctions were first discovered in skeletal muscle (55), where they are indispensable for excitation-contraction (EC) coupling (62). More recently, it was found that the interaction of an ER Ca^{2+} sensor, stromal interaction molecule 1 (STIM1), with a PM Ca^{2+} channel, Orai1, at ER/PM junctions is critical for Ca^{2+}-dependent lymphocyte activation (93). Despite the observation of neuronal ER/PM junctions, or sub-surface cisterns (SSCs), by electron microscopy since 1962 (63), little is known about the molecular components involved in neuronal ER/PM junction formation, maintenance and function (60).

Although numerous proteins are postulated to localize to ER/PM junctions (61, 64), those that stabilize the connection between the two membranes are especially important since they facilitate the interaction of other proteins which localize there. One such protein shown to localize to ER/PM junctions (or SSCs) is the primary delayed-rectifier K^+ channel in the mammalian brain,

Kv2.1. Kv2.1 regulates the action potential frequency in a wide variety of neuronal cell types in the mammalian brain, but it also displays an intriguing membrane localization pattern of micron-sized cell-surface clusters over the soma, proximal dendrites and axon initial segment (AIS) in the intact brain and in cultured neurons (13, 26). The clustered phenotype can be recapitulated heterologously in transfected HEK cells (16, 17). Electron microscopy of Kv2.1 immuno-gold labeling in the hippocampus indicated that Kv2.1 clusters localize above SSCs that are juxtaposed to astrocytic processes (18) and fluorescence microscopy in live cultured cells shows that Kv2.1 clusters reside atop projections of the ER which terminate near the PM, i.e., cortical ER (cER) (94). Consistent with these observations, Kv2.1 clusters on the soma and AIS partially co-localize with ryanodine receptors (RyR) in culture and in the intact brain (19, 20, 26). Additionally, somatic Kv2.1 clusters on α-motor neurons localize to cholinergic terminals with underlying SSCs (95) (96).

Although the localization of Kv2.1 to ER/PM junctions is well documented, no logical hypothesis as to the purpose of its localization to this specialized structure exists. We have previously demonstrated that the vast majority of clustered Kv2.1 channels are non-conducting with the majority of the K^+ flux coming from a sub-population of channels which are diffusely localized over the cell surface (69, 97). Kv2.1 is expressed abundantly in the neuronal soma, suggesting the channel takes on a non-traditional function, not related to the regulation of action potentials, which requires a high level of expression as expected of a structural or scaffolding protein. Indeed, there is a growing list of ion channels which possess discrete functions, independent of ion conduction (98). Consistent with this idea, we recently discovered that in both HEK 293 cells and hippocampal neurons, multiple types of membrane proteins are preferentially delivered and retrieved from the perimeter of Kv2.1 clusters, suggesting the clusters define cell surface trafficking hubs (51).

In this report we use fluorescence and electron microscopy to show that Kv2.1 not only localizes to ER/PM junctions but in fact induces the formation of these structures by drastically remodeling

the cER. We find that excitotoxic glutamate treatment of neurons results in a loss of Kv2.1 clusters followed by the retraction of cER from the PM. To the best of our knowledge, Kv2.1 is the first plasma membrane protein identified to govern the formation of ER/PM junctions under resting conditions. This structural role for Kv2.1 explains why a large percentage of the channels are held in a non-conducting state. This channel expression is needed to allow their accumulation without compromising electrical signaling. Given the well accepted role of ER/PM junctions in Ca^{2+} homeostasis in immune cells (93) and our previous work demonstrating that Kv2.1 clusters serve as sites for endo- and exocytosis (51), the Kv2.1-induced ER/PM junctions are proposed to represent a macromolecular complex that functions as a scaffolding site for coupling membrane trafficking to Ca^{2+} signaling.

Materials and Methods

Plasmid constructs, cell culture and transfections. Fluorescent protein, HA epitope and biotin acceptor domain (BAD) tagged Kv channel constructs have been described previously (16, 17, 69, 71) and are based on the Living Colors vector system (Clontech). The HA epitope or BAD sequence is contained within the extracellular domain between the first and second transmembrane domains of Kv2.1 (16). When necessary the BirA biotin ligase in the pSec vector was cotransfected with Kv2.1 to achieve biotinylation during channel biosynthesis, presumably within the ER lumen (16). YFP-STIM1 and Cerulean3-Orai1 were a gift from Dr. Albert Gonzales. GFP-CB5 was a gift from Gia Voeltz. YFP-Cav1.2 was a gift from Dr. Kurt Beam. The luminal ER marker pDsRed2-ER was obtained from Clontech.

HEK 293 cells (American Type Culture Collection, passage 38-45) cells were transfected using a BioRad Genepulser Xcell (BioRad Laboratories, Hercules, CA) with a 0.2 cm gap cuvette and a single 110 V 25 ms pulse. The amount of plasmid DNA used in transfection is as follows: 2 µg of Kv2.1 DNA, 200 ng of DsRed2-ER, 300 ng YFP-STIM1, 1.5 µg of Cer3-Orai1, 1 µg of GFP-CB5,

750 ng YFP-Cav1.2, 200 ng of paGFP-Actin and 1 µg of pSec Bir A. Transfected cells were plated on glass-bottom 35 mm dishes (Matek, Ashland, MA) that had been previously Matrigel-coated (BD Biosciences, San Jose, CA) and covered in DMEM + 10% fetal bovine serum. HEK cells were imaged within 24 h of electroporation in HEK physiological imaging saline consisting of (in mM): 146 NaCl, 4.7 KCl, 2.5 $CaCl_2$, 0.6 $MgSO_4$, 1.6 $NaHCO_3$, 0.15 NaH_2PO_4, 0.1 ascorbic acid, 8 glucose and 20 Hepes, pH 7.4.

Neurons from cryo-preserved E18 rat hippocampal dissociations were plated at a density of ~15,000 - 30,000 cells/cm^2 on poly-D-lysine coated glass-bottom dishes (Matek, Ashland, MA) and cultured in glial-cell conditioned neurobasal medium containing B27 supplement (Life Tech, Carlsbad, CA) as previously described (17). Animals were deeply anesthetized with isoflurane and euthanized by decapitation according to a protocol approved by the Institutional Animal Care and Use Committee (IACUC) of Colorado State University. Transfections were performed after 6-10 days in culture with 2.0 µl of Lipofectamine 2000 (Life Tech) using pin 100 µl OptiMem (Life Tech) according to the manufacturer's directions. Two-hours after transfection, the culture medium was replaced with fresh Neurobasal/B27 media. Neurons were imaged 24-48 hours post-transfection in neuronal imaging saline consisting of (in mM) 126 NaCl, 4.7 KCl, 2.5 $CaCl_2$, 0.6 $MgSO_4$, 0.15 NaH_2PO_4, 0.1 ascorbic acid, 8 glucose, and 20 HEPES, pH7.4.

TIRF microscopy. The majority of experiments utilizing light microscopy were performed using total internal reflection fluorescence (TIRF) microscopy to restrict illumination to within ~100nm of the basal surface of the cell in order to visualize the cortical ER (94). Transfected HEK cells and neurons were imaged with a Nikon Eclipse Ti Perfect-Focus equipped TIRF/widefield fluorescence microscope equipped with AOTF controlled 405, 488, 543 nm diode lasers, 100 mW each, and an Intensilight wide-field light source. A 100X PlanApo TIRF, 1.49 NA, objective was used for image acquisition. Emission was collected through a Sutter Lambda 10-3 filter wheel containing the appropriate band pass filters. The stage and objective are temperature controlled

via a Zeiss/Pecon stage heating insert and objective heater at 37°C. This microscope is equipped with the Andor iXon EMCCD DU-897 camera, 512x512. For all imaging experiments, the cells were on the microscope stage for less than one hour. Perfusion during imaging experiments was gravity fed into a culture dish insert (Wheaton, Millville, NJ) and aspirated by a peristaltic pump to achieve even flow.

Immunocytochemsity. For immunolabeling endogenous Kv2.1 in developing neurons we fixed cells with 4% formaldehyde in neuronal imaging saline (NIS) and labeled with a mouse monoclonal anti-Kv2.1 antibody (NeuroMab, Irvine, CA, K89/34) diluted 1:1000 in NIS w/ 5% goat serum. Secondary labeling was with a goat anti-mouse AlexaFluor594 (1:5000, Life Tech, Carlsbad,CA). Standard 3D imaging of fixed, immunolabeled cells was performed with an Olympus FV1000 confocal microscope equipped with spectral detectors and the SIM scanner. GFP was excited using the 488 nm line of an argon laser and emission was collected using the variable bandpass filter set at 500-530 nm. AlexaFluor 594 fluorophores were detected using a 543 nm HeNe laser with the variable bandpass filter set at 600-630 nm. A 60X, 1.4NA oil immersion objective was used for imaging and the pinhole diameter set for the appropriate Airy unit when using one laser. An intermediate pinhole diameter was used when two fluorophores were being detected simultaneously.

Kv2.1 reclustering.. HEK cells transfected with GFP-Kv2.1 and DsRed2-ER were removed from the incubator, washed once with HEK imaging saline and immediately placed on the room temperature TIRF microscope stage. The stage and objective heaters were then turned on to slowly return the cells to 37°C. Quickly, a cell was found that expressed both GFP and DsRed2, but lacked apparent Kv2.1 clusters. Cells were imaged in both red and green for 20-30 minutes at 0.3 Hz while Kv2.1 clusters reformed.

Actin depolymerization. HEK cells transfected with GFP-Kv2.1 and DsRed2-ER were imaged in TIRF at 0.3 Hz and either 10 µM of Latrunculin A (LatA) or 200 nM Swinholide A (SwinA) was added to the bath by pipette (Sigma-Aldrich, St. Louis, MO).

Particle image velocimetry analysis. HEK cells were transfected with either DsRed2-ER alone or GFP-Kv2.1 and DsRed2-ER, and the DsRed2_ER signal was imaged in TIRF at 10 Hz.

Glutamate induced Kv2.1 declustering. Rat hippocampal neurons were transfected between day *in vitro* (DIV) 6-10 with GFP-Kv2.1 and DsRed2-ER and imaged 24-48 hours later. Neurons expressing both plasmids were imaged in TIRF for 5 to 10 minutes prior to perfusion of 20 µM glutamate in neuron imaging saline at room temperature. Glutamate perfusion lasted 30 to 60 seconds and then the glutamate solution was allowed to sit in the bath for the remainder of imaging. For intensity measurements the locations of Kv2.1 clusters were automatically tracked using a centroid-based algorithm implemented in LabView (National Instruments, Austin, TX). Intensity measurements were normalized by subtracting the minimum and dividing by the maximum value. Normalized intensities were plotted in Log_{10} scale, and the fluorescence decrease was fit with equation (1): $I(t) = \exp[-(t-T)/\tau]$, where T is the lag time and τ the characteristic fluorescence decay time. The lag time between glutamate perfusion and fluorescence loss was measured by hand as the point where the linear fit described in equation (1) crosses the baseline fluorescence level (dashed lines, Figure 14E). Pearson's coorelations and p-values were calculated as described (99).

Image presentation and data analysis. Images were imported into Volocity 6.1.1 software for object detection/tracking and quantitative analysis. Numerical data were exported into Origin Pro 8.5 for further analysis and curve fitting.

Statisitics. Data are presented as the mean± sd unless otherwise indicated.

Electron Microscopy. HEK 293 cells (ATCC, Manassas, VA) at low passage (p37-p44) were transfected with Kv2.1-HA or no plasmid, fixed in 2.5% glutaraldehyde in 0.15M Sorensen's phosphate buffer (SPB), pH7.4, and free aldehydes were quenched with 1% sodium borohydride. Primary antibody was a monoclonal anti-HA conjugated to biotin (Pierce, Rockford, IL) diluted 1:100 in SPB with 1% IgG and Fatty-acid free BSA (Sigma-Aldrich, St. Louis, MO). Goat anti-mouse 10 nm and 20 nm gold conjugated antibodies were diluted 1:50 (Ted Pella, Redding, CA). Following labeling, cells were postfixed in osmium tetroxide, en bloc-stained with uranyl acetate and embedded in alradite/epon. Following thin sectioning, samples were observed on a JEOL 1400 TEM. Quantification of gold labeling and ER/PM junctions was performed using the ImageJ plugin TrakEM2(100) (101).

TIRF Microscopy. Fluorescent light microscopy was performed using a Nikon TE2000, objective-based TIRF system equipped with an electron multiplied charged coupled device (EMCCD iXon 897, Andor, Belfast, Northern Ireland) camera. The incident angle was calculated based on an empirically determined critical angle for total internal reflection, to limit the penetration depth to less than 100 nm from the coverslip as previously described (97).

Tracking of cER/Kv2.1 clusters. Kv2.1 clusters and associated cER were automatically tracked using a centroid-based algorithm implemented in LabView (National Instruments, Austin, TX). The images were manually thresholded in order to eliminate background effects and then the centroid of the structure (X_c,Y_c) was determined from its fluorescence intensity profile, $Xc = \sum_x \sum_y xI(x,y) / \sum_x \sum_y I(x,y)$ and similarly for Y_c, where $I(x, y)$ is the intensity of the image at point (x, y) (102).

Results

Kv2.1 expression remodels the cER in HEK 293 cells. After transfecting HEK cells with GFP-Kv2.1 and the luminal ER marker, DsRed2-ER, we observed that in cells expressing only DsRed2-ER, the cER in the TIR illumination field, i.e., within 100 nm of the coverslip, had a very different structure relative to that observed in cells where Kv2.1 was also expressed. Fig. 25A shows the cER pattern in two distinct HEK cells outlined in white that were transfected with both GFP-Kv2.1 and DsRed2-ER and then imaged with total internal reflection fluorescence (TIRF) microscopy. Fig. 25B shows that the top cell received only the DsRed2-ER marker while the bottom left cell received both plasmids, and has large GFP-Kv2.1 clusters. Without Kv2.1, the cER appears as either small puncta (Figure 8C, yellow arrow) or tubules. In the presence of Kv2.1 the cER is dramatically remodeled (Figure 8D), as most of the cER now appears as large planar structures (white arrow) immediately beneath the Kv2.1 clusters. The Kv2.1-induced cER remodeling was also observed in day *in vitro* (DIV) 7 cultured rat hippocampal neurons (rHNs), when endogenous Kv2.1 clusters are not yet expressed (103), as illustrated in Figure 9. The remodeled cER pattern in both cell types is reminiscent of the pattern induced by expression of STIM1 (104), which forms ER/PM junctions in response to ER Ca^{2+} depletion. However, the axial resolution of TIRF imaging is too low to demonstrate that Kv2.1 induces a true ER/PM junction, i.e. a < 20nm gap between the two membranes (66). Thus, in order to examine the spatial relationship between Kv2.1 clusters on the PM and the underlying cER at high resolution we used thin-section immuno-electron microscopy. HEK 293 cells were either mock transfected (no plasmid DNA) or transfected with Kv2.1-HA and labeled with biotinylated anti-HA- antibody, followed by streptavidin conjugated to 10-nm and 20-nm gold particles. As we previously reported (94), the cER in Kv2.1-free HEK cells typically appeared as tubular structures which approach the PM but fail to make close (less than 20 nm) and continuous structures characteristic of ER/PM junctions.

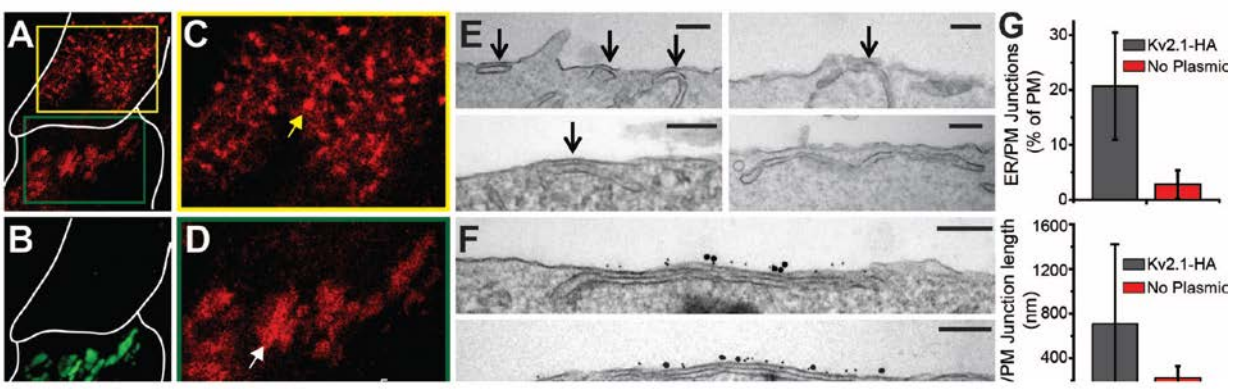

Figure 8: Clustering of Kv2.1 induces the formation of ER/PM junctions. Three HEK cells, outlined in white, transfected with the luminal ER marker, DsRed2-ER (A) and GFP-Kv2.1 (B) imaged using TIRF microscopy. The bottom cell has large GFP-Kv2.1 clusters, while the top left cell has no Kv2.1 expression. Both cells express similar intensities of DsRed2-ER. C. Enlargement of the region in the yellow box from A. Note the mesh-like pattern of the cortical ER (cER) which consists of tubules and bright puncta (yellow arrow). D. Enlargement of the green box in A. Note the absence of mesh-like tubules in favor of large planar cER structures (white arrow). Immuno-gold labeling and electron microscopy were used to visualize the ultrastructural features of Kv2.1-remodeled cER. E. EM micrographs of cER from mock transfected HEK cells. Black arrows point to endogenous ER/PM junctions, which tended to be ~200nm in length. Bottom right panel shows a long stretch of cER which fails to make the consistent close contact which is a hallmark of ER/PM junctions. F. Two EM micrographs of long ER/PM junction (~1 micron) in a Kv2.1-HA transfected HEK cell. 10nm & 20nm gold label Kv2.1-HA channels on the cell surface (Scale bars for EM micrographs are 200 nm). G. Bar graphs summarizing the effect of Kv2.1 expression on ER/PM junctions in HEK cells. Top graph illustrates the average length of ER/PM junctions in cells positive for Kv2.1 immunogold labeling versus mock transfected cells. Bottom graph shows the percent of the PM with associated ER junctions in cells positive for Kv2.1 immunogold labeling versus mock transfected cells (mean±SD).

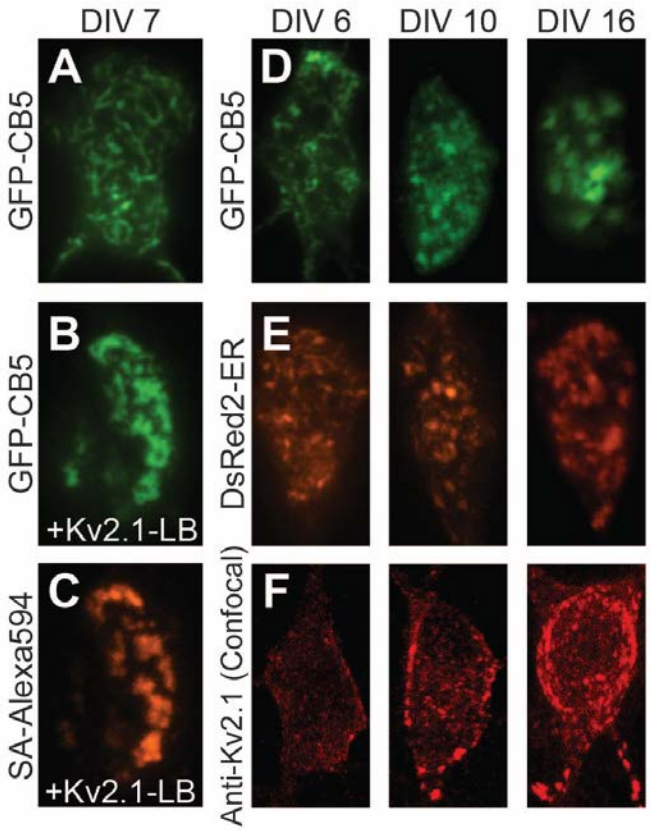

Figure 9. Kv2.1 expression remodels the cortical ER in cultured rat hippocampal neurons. A. Representative day in vitro (DIV) 7 rHN transfected with GFP-CB5 and imaged in TIRF. The majority of neurons imaged at this timepoint had clear tubular cER and small punctate cER, but lacked larger cER structures. B-C. A representative DIV 7 rHN tranfected with GFP-CB5 (B) and Kv2.1-LoopBAD (C, surface labeled w/ streptavidin-Alexa594) imaged in TIRF. The large, Kv2.1-associated cER structures (B, GFP-CB5) were strikingly different than anything present in DIV 7 neurons without ectopic expression of Kv2.1. D-F. To observe how the cortical ER changes during the maturation of rat hippocampal neurons in culture, we expressed the ER markers GFP-CB5 (D) and DsRed2-ER (E) in 6, 10, and 16 DIV neurons and imaged them in TIRF. We compared the cER pattern to untransfected cultures immunolabeled for Kv2.1 and imaged by confocal microscopy (F, merged z-stacks). At DIV 6, the cER was almost exclusively tubular in appearance with some bright puncta visible. Kv2.1 immunolabeling is visible above background, but no clusters are apparent. At DIV 10, many neurons had small, round cER structures instead of tubules. Kv2.1 immunolabeling was more apparent on the PM where neurons typically had numerous small clusters. At DIV 16, tubules and small rounded cER structures were still apparent in most cells. Less frequently, larger cER structures reminiscent of Kv2.1 clusters in HEK cells were observed. Most large neurons had bright Kv2.1 immunolabeling with a variety of cluster sizes over the majority of the soma surface.

Figure 8E shows a fragment of cER which maintains some proximity to the PM but lacks the close, even gap typical of ER/PM junctions (105). These organelles likely correspond to the tubular structures observed in TIRF in Figure 8C. Less frequently, we also observed small endogenous ER/PM junctions (black arrows, Figure 8E which displayed the even, tight contact characteristic of ER/PM junctions and likely correspond to the bright puncta seen with TIRF microscopy. In contrast, when Kv2.1-HA was expressed in the HEK cells we frequently observed larger ER/PM contacts where the two membranes were within 10-15 nm of each other over long distances. Figure 8F illustrates two such junctions, where the cER makes consistent contact with the PM over almost a micron before turning back into the cytoplasm. Several 10 and 20 nm gold particles are visible directly over junctional membrane, which confirmed the clustering of Kv2.1 on the PM. Figure 8G summarizes the effect of Kv2.1 expression on ER/PM junctions in HEK cells. The average length of junctions in cells with positive Kv2.1 labeling was 708±714 nm (n=17 cells, mean±SD, number of junctions) compared to endogenous junctions in mock transfected cells which were 222±107 nm (n=36). The fraction of PM area involving ER junctions in cells positive for Kv2.1 labeling was 20.7±9.8% versus only 2.8±2.6% in mock transfected cells. The mean distance between the cER and PM in Kv2.1 positive cells was 13±3 nm (n=10). This distance is small enough to postulate that the cytoplasmic domains of Kv2.1 directly interact with either ER membrane protein or lipid components. Taken together the images presented in Figure 8 indicate that in HEK cells Kv2.1 expression significantly remodels the cortical ER and greatly enhances the surface area of ER/PM junctions.

Kv2.1 cluster formation and cER remodeling occur simultaneously. In HEK cells expressing GFP-Kv2.1, cell surface clusters are often lost when the cell culture dish is removed from the incubator, media replaced with imaging saline and the dish placed on the heated TIRF microscope stage. However, after a few minutes the clusters reform as the dish returns to physiological temperature (37^{o}C).

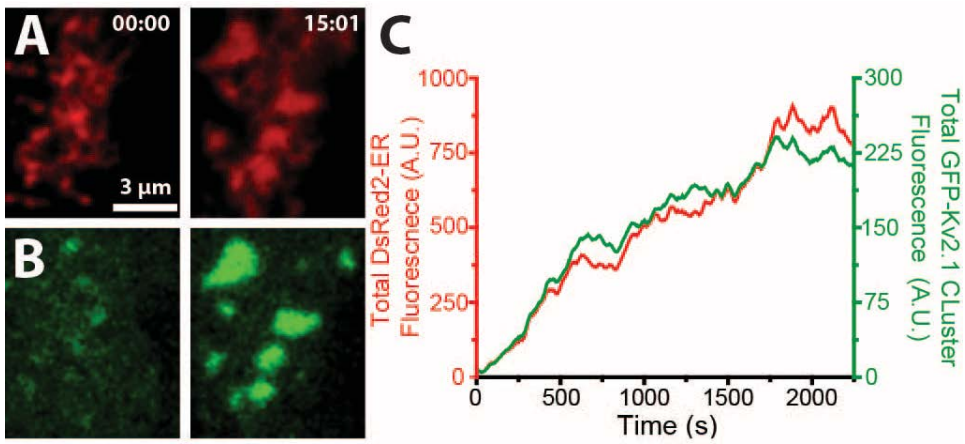

Figure 10: Clustering of Kv2.1 and formation of ER/PM junctions. Transfected HEK cells expressing DsRed2-ER (A) and GFP-Kv2.1 (B) were removed from the incubator, growth media replaced with imaging saline, and placed on a 37C incubator on the TIRF microscope stage. Frequently, cells expressing GFP-Kv2.1 initially lacked clusters (B, left panel) while the cER was largely tubular in appearance (A, Left panel). Over the next 20 minutes of imaging, Kv2.1 clusters formed (B, right panel) and the cortical ER remodeled from tubules into larger, planar structures (A, right panel). C. Mean pixel intensities from GFP-Kv2.1 clusters (green points) and bright cortical ER puncta (red points) during Kv2.1 re-clustering. Fluorescent intensities of Kv2.1 clusters and cER increase in concert with one another.

We took advantage of this dynamic to examine the temporal relationship between Kv2.1 cluster formation and cER remodeling in cells expressing both GFP-Kv2.1 and the DsRed2-ER marker. As illustrated in Figure 10A, cells showing a homogenous Kv2.1 surface expression pattern at the beginning of imaging had a tubular cER structure within the TIR illumination field similar to that observed in non-transfected cells (see Figure 8A). As Kv2.1 clusters reformed and grew over 20 min, the associated cER fluorescence increased (Figure 10B). It appeared that the cER spontaneously-forming puncta served as nucleation sites for Kv2.1 cluster formation. Figure 10C quantitates the temporal co-evolution of GFP-Kv2.1 clusters and cER fluorescence beneath these clusters. GFP-Kv2.1 cluster formation and development of the DsRed2-ER junction fluorescence occurred concurrently, suggesting that cluster formation and direct interaction of Kv2.1 with the ER membrane are closely linked processes. If Kv2.1 cluster formation was first required for the ER to be pulled into close proximity with the plasma membrane, cluster formation should have preceded the induction of the ER/PM junctions. The images presented in Figure 10 are consistent with a model in which freely diffusing Kv2.1 begins to bind the cER membrane whenever it is in close proximity with the plasma membrane. The resulting cER tethering at the plasma membrane further enhances Kv2.1 clustering which in turn leads to enhanced ER/PM junction formation.

Kv2.1 stabilizes the associated cER. From the experiment illustrated in Figure 10, it appeared that cER associated with Kv2.1 clusters was more stable than the rest of the cER, which was likely making only sporadic contact with the PM. Therefore, we next examined the effect of Kv2.1 expression on cER dynamics. HEK cells transfected with GFP-Kv2.1 and DsRed2-ER were mounted on the microscope stage and after a few minutes we searched for pairs of cells expressing DsRed2-ER (Figure 11A) but with only one of them expressing Kv2.1 (lower left, Figure 11B).

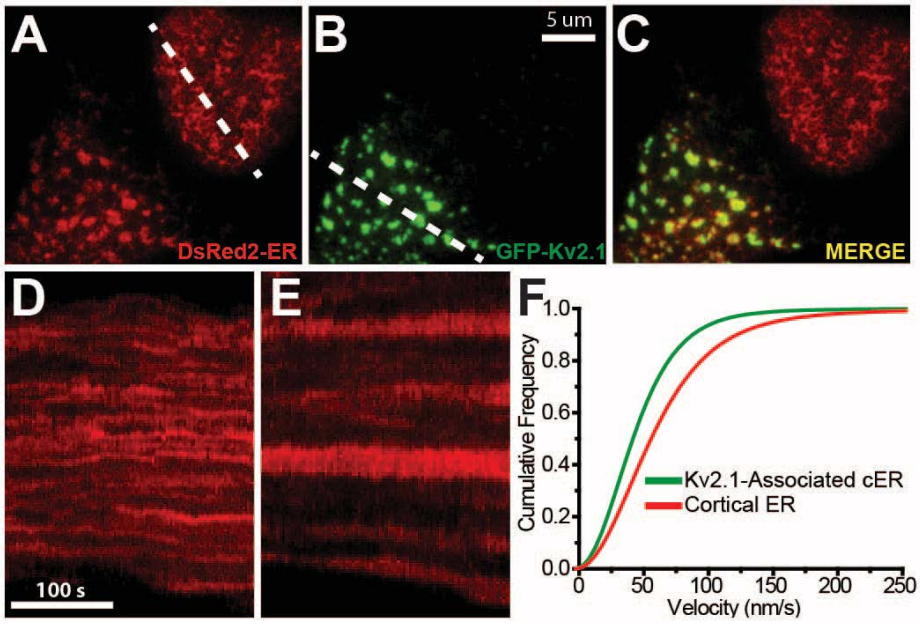

Figure 11: Kv2.1 clustering enhances the stability of underlying cER. A. Two HEK 293 cells transfected with DsRed2-ER (A) and GFP-Kv2.1 (B), imaged in TIRF. The cell on the bottom left has abundant Kv2.1 clusters while the cell on the top right is completely devoid of clustered Kv2.1. C. A merge of the two fluorescent channels in A and B, illustrating the association between Kv2.1 clusters and the remodeled cER. D Kymograph generated from the dashed white line in (B) intersecting tubular cER which shows the movement typical of cER in HEK cells (4 min total). E. Kymograph generated from the dashed white line in (B), intersecting Kv2.1-induced ER-PM junctions, which highlights the long-term stability of these junctions. F. A cumulative frequency plot of velocities from normal cER (red line) and Kv2.1-associated cER (green line) as measured by particle image velocimetry. As a population, the Kv2.1-associated cER has smaller velocities than the normal cER, hence the cER is less dynamic upon association with Kv2.1.

Figure 11A is a kymograph taken from the dashed white line in Fig. 28A, through a cell expressing only DsRed2-ER, illustrating the movement typical of the cER in HEK cells over 4 min. This is contrasted by the kymograph in Figure 11E which is taken from Kv2.1-associated cER, corresponding to the white dashed line in Figure 11B. These lines emphasize the cER edges and thus are sensitive to cER movement. As indicated in the kymographs the cER appears qualitatively more stable in the presence of Kv2.1 as might be expected for cER "spot welded" into true junctions with the plasma membrane. In contrast, the unanchored cytoplasmic cortical ER is more dynamic. In order to quantitate the cER mobility we employed particle image velocimetry (PIV) analysis (106). In cells expressing Kv2.1 clusters, the mean velocity of the cER measured within 0.32-s intervals was 50±38 nm/s (n=5 cells), while in cells expressing only DsRed2-ER the mean velocity was 69±56 nm/s (n=6). Not only are the mean velocities of unanchored cER significantly higher but their standard deviation is higher as well, which is a consequence of unanchored cER having the ability to move more freely. The cumulative distribution function (CDF) of the velocities shown in Figure 11F, i.e., the probability of the cER having velocities smaller than a given value, indicates that as a population, the cER is less dynamic upon interaction with Kv2.1. Such enhanced stability is predicted to provide a sturdy platform for the signaling events potentially occurring at the ER/PM junctions.

Kv2.1-induced ER-PM junctions are sensitive to actin depolymerization. Kv2.1 clusters tend to reside in regions absent of underlying cortical actin (Figure 13C) (15), presumably because that space is occupied by the cER. Kv2.1 clusters are also sensitive to actin depolymerization, either growing in size or disappearing entirely (15, 28). Mild actin depolymerization induced by the G-actin binding toxin latrunculin A (LatA, 10 μM) resulted in an increase in the size of Kv2.1 clusters as well as the size of the underlying cER (Figure 13D-F).

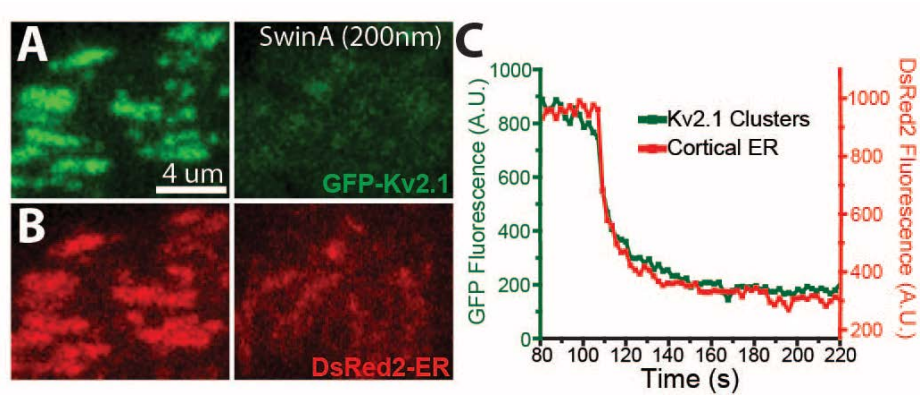

Figure 12. Obligate role of the actin cytoskeleton in Kv2.1-induced ER/PM Junctions. HEK 293 cell transfected with GFP-Kv2.1 (A) and DsRed2-ER (B) immediately before (left panel) and 5 minutes after (right panel) application of 200nM Swinholide. Kv2.1 clusters almost completely dissolved while the cER appeared to retract away from the evanescent field of the TIRF microscope. The remaining cER appeared largely tubular. C. Plot of the total fluorescence intensity of Kv2.1 clusters (green line) and cER structures (red line) following application of SwinA (black arrow).

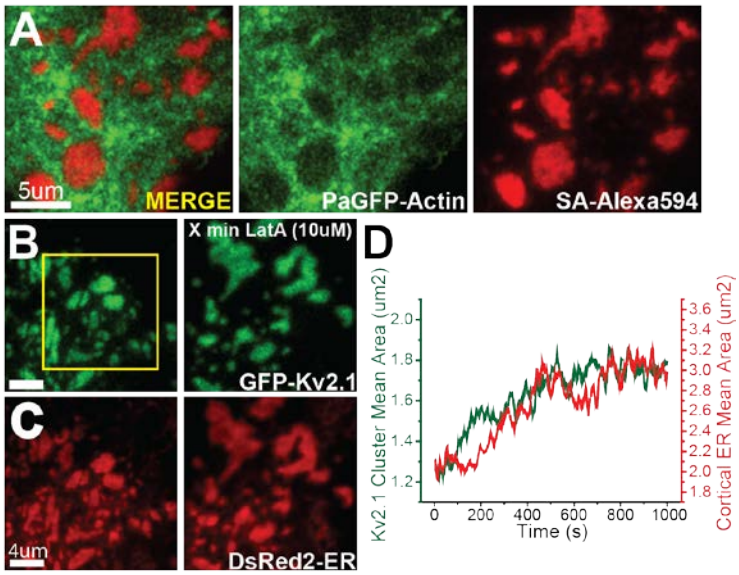

Figure 13. Cortical actin bounds Kv2.1 cluster-induced ER/PM junctions. A. HEK 293 cell transfected with paGFP-Actin (middle panel) and Kv2.1-LoopBad (right panel, labeled with streptavidin-AlexFluor594) and imaged using TIRF microscopy. PaGFP-Actin was activated in TIRF with a 405nm laser, producing a clear image of the underlying cortical actin cytoskeleton without interference from actin cytoskeleton from deeper within the cell. In the merged image (left panel), Kv2.1 clusters (red) localize to areas of decreased paGFP-Actin density (cortical actin holes). These cortical actin holes are occupied by Kv2.1-associated cER. B & C. HEK 293 cell transfected with GFP-Kv2.1 (B) and DsRed2-ER (C) immediately before (left panels) and 15 minutes after (right panels) application of 10uM Latrunculin A. Several Kv2.1 clusters and the associated cER structures appear to fuse together, increasing the overall area of each cluster. D. Plot of the mean area of Kv2.1 clusters (black line) or cER sturcutures (red line) immediately following application of LatA. The two structures grow in size together, although the mean area of cER structures lags with respect to Kv2.1 clusters due to the smaller non-Kv2.1 cluster associated structures. The smaller structures eventually become incorporated into the larger Kv2.1-associated cER structures.

We also examined the effect of actin depolymerization with 200 nM Swinholide A (SwinA) on the Kv2.1-induced ER/PM junctions. Swin A not only sequesters G-actin but it also severs stable filaments. Fig. 29 demonstrate that Swin A causes parallel Kv2.1 declustering (Figure 12A) and loss of the ER/PM junctions (Figure 12B). Quantitation of the relationship between the GFP-Kv2.1 cluster fluorescence with that of the underlying DsRed2-ER signal (each determined separately) is shown in Figure 12C. Following SwinA treatment, the intensity of Kv2.1 clusters decreased on average by 78±12% while the intensity of the cER decreased by 62±23% (n=6) Both fluorescent signals are lost concurrently, again supporting the idea that Kv2.1 clustering and induction of the ER/PM junction are closely linked processes in transfected HEK cells.

Glutamate excitotoxicity disrupts Kv2.1-induced ER/PM junctions. In order to address the relationship between Kv2.1 clustering and ER/PM junction formation in a physiologically relevant environment we turned to cultured rat hippocampal neurons (rHNs). Kv2.1 clusters are sensitive to stroke-related insults such as chemical ischemia and glutamate excitotoxicity, both in culture and in the intact brain (29, 30, 43, 49). Therefore, we used excitotoxic glutamate treatment to induce cluster dissolution in cultured rHNs and examine the effect of Kv2.1 declustering on the underlying cER. Cultured rHNs were transfected with GFP-Kv2.1 and DsRed2-ER, which colocalized almost perfectly when imaged in TIRF (Figure 14A, left panel). Cells were imaged for 5-10 minutes to establish a stable baseline prior to application of 20 µM glutamate, which is set as time $t = 0$. In the first few minutes following glutamate treatment, the Kv2.1 clusters dissolved almost entirely (Figure 14C). The Kv2.1-associated cER dramatically decreased in size and fluorescence intensity (Figure 14D), however this occurred more slowly and typically did not begin until after the Kv2.1 clusters were partially dissolved. This phenomenon is illustrated in Figure 14B-D which are magnified from the white box in Figure 14A.

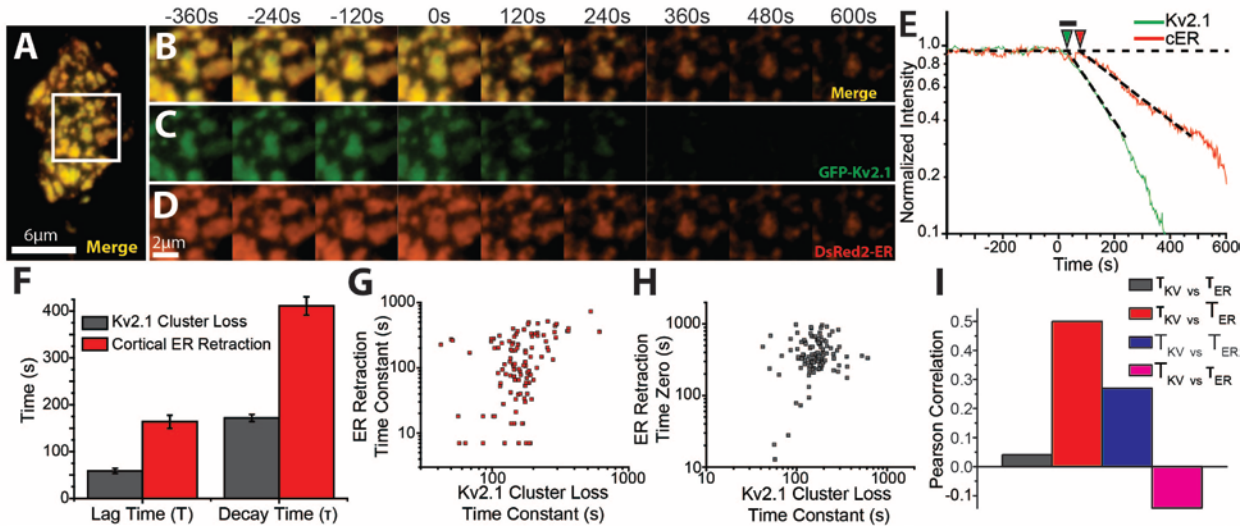

Figure 14: Kv2.1-induced ER/PM junctions are sensitive to glutamate excitotoxicity in neurons. The effect of excitotoxic glutamate (Glut, 20μM) exposure was studied in DIV 10 rat hippocampal neurons (rHNs) transfected with GFP-Kv2.1 and DsRed2-ER, and imaged in TIRF to visualize the Kv2.1-induced ER/PM junctions. A. Representative neuron illustrating perfect co-localization between GFP-Kv2.1 and DsRed2-ER. B-D. Panels are magnified from the white box (A) and contain a series of images over the course of glutamate exposure (beginning at 0 seconds). GFP is lost from clusters following glutamate exposure as channels diffuse out of the clusters, while DsRed2-ER signal is lost as the cER moves away from the PM towards the interior of the cell. E. A representative trace of the fluorescence intensity of an individual cER/Kv2.1-cluster pair, normalized to the max and min values and plotted on a log10 scale. The black bar indicates the duration of 20μM glutamate perfusion and the green (Kv2.1) and red (ER) arrowheads denote the time difference between glutamate perfusion and the initial decrease in fluorescence (lag times, T_{KV} and T_{ER}). The dashed lines denote the area of each trace used for a linear fit with a slope of (e^[-(t-T/τ)] from which we extracted characteristic fluorescence decay times (τ_{KV} and τ_{ER}). F. Bar graphs summarizing the lag times (T_{KV} and T_{ER}), and the decay times (τ_{KV} and τ_{ER}), (mean±SEM, n = 115 clusters, from 9 cells). G. Scatter chart illustrating the positive correlation between T_{ER} and τ_{KV}. H. Scatter chart illustrating the low correlation between τ_{KV} and τ_{ER}. I. Bar graph illustrating the Pearson's correlations between the lag times and the decay times (τ).

Given that the concentration of DsRed2 fluorophores within the ER lumen is not expected to change, the decrease of the fluorescence intensity suggests the cER moves away from the TIRF evanescence excitation field by retracting away from the PM. Thus, the loss of Kv2.1 channels from the clusters appears to be correlated to a retraction of the cER.

To analyze the temporal relationship between Kv2.1 cluster dissolution and cER retraction we measure the fluorescent intensity of 115 clusters and the underlying ER structures in 9 different neurons. For intensity measurements the locations of Kv2.1 clusters are automatically tracked using a centroid-based algorithm implemented in LabView. Figure 14E shows a trace from a single cluster taken from the cell shown in Figure 14A. The beginning of glutamate perfusion occurs at time $t = 0$ and the duration is indicated as a black bar (glutamate perfusion lasted 45 s). The loss in fluorescence of Kv2.1 clusters and cER is observed to start a lag time T_{KV} and T_{ER} after the beginning of glutamate treatment, which is indicated in the figure by the green and red arrowheads, respectively. After the onset of fluorescence loss, the intensity of both Kv2.1 clusters and cER follows a single-exponential decay for several minutes. Thus, the rate of fluorescence loss is characterized by a single parameter τ, which is found from an exponential fit, as shown in the figure,

$$I(t) = \exp[-(t-T)/\tau] \qquad (1)$$

where T is the lag time and τ the characteristic fluorescence decay time for either Kv2.1 or ER. Equation (1) holds for both Kv2.1 and ER, albeit with different parameters. Figure 14F shows the means and standard errors of the lag times (T_{KV} and T_{ER}) and the decay times (τ_{KV} and τ_{ER}). Kv2.1 clusters began dissolving an average of T_{KV} =59±58 s after the initial glutamate application, while the associated cER began losing fluorescence consistently later, with an average lag time of T_{ER} = 164±147 s. The rate at which Kv2.1 cluster fluorescence decreased was also consistently faster than the associated cER (τ_{KV} = 172±81 s, τ_{ER} = 411±209 s). If the retraction of the cER from the

PM was the result of Kv2.1 unbinding from a cER component, we would expect there to be some correlation between the loss of Kv2.1 cluster fluorescence and the retraction of the associated cER. Figure 14G shows a scatter plot of T_{ER} against τ_{KV} where each individual point is a Kv2.1 cluster/cER pair. Here, a positive correlation is found, which is confirmed by the Pearson's correlation coefficient r = 0.5 (Figure 14I). A calculation of the significance of the correlation between T_{ER} and τ_{KV} yields a p-value of 10^{-8} (99). Thus, the time it takes after glutamate application for the cER to begin retracting is clearly correlated to the rate at which Kv2.1 clusters dissolve. A shorter lag time between Kv2.1 cluster dissolution and cER retraction is linked to a more rapid loss of Kv2.1 cluster fluorescence. Figure 14H displays a scatter plot of τ_{KV} vs. τ_{ER} where there is no evident correlation between Kv2.1 and cER decay times. This observation is also confirmed by computing the Pearson's correlation coefficient (Figure 14I), which yields r = 0.04. Thus the rate of Kv2.1 cluster dissolution does not affect the rate of Kv2.1-associated cER retraction. This is perhaps not surprising since loss of Kv2.1 fluorescence is due to channel diffusion out of the cluster, while loss of cER fluorescence is due to the movement of the cER away from the PM, which are very different processes. These data suggest that glutamate excitotoxicity results in a dramatic retraction of the cER with a starting point that depends on the rate of the loss of Kv2.1 clusters.

Discussion

Although an association between Kv2.1 clusters and the ER has been established (18, 19, 103), the results presented above indicate that Kv2.1 plays an active role in forming a MCS composed of the cER and PM. Using both live cell TIRF imaging and immuno-gold electron microscopy we show that Kv2.1 expression in HEK cells dramatically increases the amount of cER membrane in close (<20nm) proximity to the cell surface. This induction of micron-sized ER/PM junctions occurs at rest, in the absence of ER Ca^{2+} depletion. Analysis of the temporal relationship between Kv2.1

clustering and cER remodeling, as illustrated in Figure 10 and 12, suggests that channel clustering and cER interaction are closely linked processes, for we did not observe Kv2.1 cluster formation preceding ER/PM junction formation.

Although the existence of the unique Kv2.1 clusters has been known for a long time, the mechanism underlying Kv2.1 clustering has been elusive, especially with the unique behavior of channels within the clusters. Clustered channels are essentially free to diffuse within the border of the clusters, but are confined to the cluster for long times. Non-clustered channels are free to diffuse through the clusters without any apparent obstruction (17) (16). We postulate that the critical factor in Kv2.1 cluster localization is binding to an unknown ER factor, whether it be protein or lipid, which is mobile within the ER membrane. Since the clustering of Kv2.1 is dependent upon the phosphorylation state of a 26-amino acid sequence on the intracellular C-terminus called the proximal restriction and clustering (PRC) domain (26), it is likely that channels with the proper combination of phosphorylated residues bind to this ER factor which in turn prevents them from diffusing away from the cER positioned below. Channels lacking the proper combination of phosphorylation will move through the cluster without hindrance. Indeed, removal of the majority of the C-terminus causes a complete abrogation of clustering (27), as do individual serine point mutations in the PRC (26). Figure 15A & B illustrate that two such point mutants (S583A and S586A) within the PRC eliminate Kv2.1 clustering and leave the cER with a tubular, mesh-like pattern typical of untransfected HEK cells. Mutation of a single serine residue just outside the PRC (S603A, Figure 15C) does not abrogate clustering entirely, but fails to remodel the cER as dramatically as wild-type Kv2.1, suggesting a weakened interaction with the cER. Removal of a syntaxin binding domain (ΔSBD) on the proximal C-terminus does not drastically alter Kv2.1 clustering (Figure 15D). The glutamate induced declustering in Figure 14 is therefore likely due to Ca^{2+} influx induced dephosphorylation (49), which frees the Kv2.1 C-terminus from the cER membrane, allowing channels to diffuse out of the cluster. The time lag between declustering and

cER retraction likely results from only a fraction of the clustered channels being required to hold the cER membrane at the cell surface.

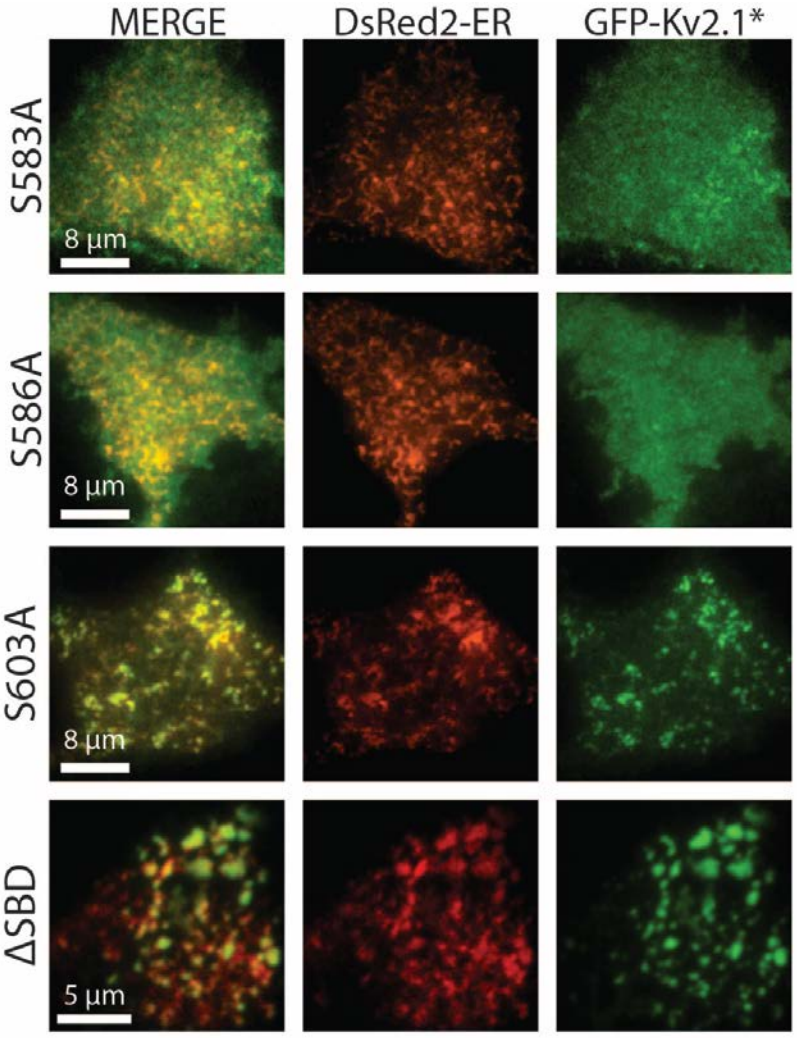

Figure 15. Kv2.1 clustering and remodeling of the cER are disrupted by C-terminal mutations. HEK 293 cells transfected with DsRed2-ER (right panel) and GFP-fused Kv2.1 mutants (middle panel), imaged in TIRF. S583A (top row) and S586A (middle row) are phosphorylated serine residues located in the proximal regulation of clustering (PRC) domain. These mutants have no effect on the cER and display no clustering. S603A is a phosphorylated residue just outside the PRC and displays smaller clusters then wild-type Kv2.1 and doesn't remodel the cER as drastically. ΔSBD is missing the Kv2.1 syntaxin binding domain (SBD, Δ411-522). ΔSBD appears to form nearly WT clusters and remodels the cER. (*Kv2.1 mutants)

Other ER/PM junction inducing proteins. The discovery of STIM1 led to a newfound interest in the physiological role of inter-organelle junctions formed between the ER and PM (65). Recently, another family of mammalian proteins named the extended syntaxins (E-Syt) were discovered which possess similar attributes (68). Both families include members who form junctions in response to a decrease in ER Ca^{2+} concentration and members who localize to junctions under resting conditions (61). Furthermore, both are ER resident proteins which induce the formation of ER-PM junctions through interactions of their cytoplasmic poly-basic motifs with anionic phospholipids on the inner leaflet of the PM (68, 107). There are other ER proteins which have been implicated in the formation and maintenance of ER/PM junctions, such as the junctophilins, junctate, and RYR (61), but only the junctophilins remodel the cER as dramatically as that observed with STIM1 or E-Syt1 (108). Thus the Kv2.1-induced ER/PM junctions are notable in that they occur by a PM protein interacting with the ER, a different mechanism than those induced by ER resident proteins, exist under resting conditions in a wide variety of neuronal cell types, and they are sensitive to neurotoxic insults.

Function of neuronal ER/PM junctions. Although ER/PM junctions possess several physiologically relevant functions, most frequently the junctions are implicated in Ca^{2+} signaling. In many cell types, STIM1 translocates to and enlarges ER/PM junctions in response to a drop in ER Ca^{2+}. Activated STIM1 in turn binds and gates PM Ca^{2+} channels including Orai1 and members of the transient receptor potential C (TRPC) family, leading to Ca^{2+} flux, ER Ca^{2+} store refilling and transcription factor activation (93). In the presence of Kv2.1-clusters, activated STIM1 molecules translocate to the Kv2.1-induced ER/PM junctions where they bind and localize Orai1 (Figure 16). Thus, Kv2.1 clusters could be sites of ER Ca^{2+} store or agonist operated Ca^{2+} entry. Furthermore, previous reports indicate that activated STIM1 binds to, and inhibits, L-type Ca^{2+} channels (LTCC) (104, 109). In rHNs expressing Kv2.1 and the LTCC Cav1.2, both proteins localize to surface clusters (Figure 17), suggesting that regulation of LTCC activity can occur here.

Ryanodine receptors partially colocalize with Kv2.1 clusters in neurons, on the soma (19) and the AIS (20), and it has been suggested that Kv2.1 may interact directly with RYRs. We observe almost perfect colocalization between Kv2.1 clusters and DsRed2-ER at the AIS (Figure 18), making it likely that RYRs localization here is a result of Kv2.1-induction of ER/PM junctions. Thus, multiple proteins involved in Ca^{2+} signaling localize to Kv2.1-induced ER/PM junctions, suggesting that Ca^{2+} signaling or homeostasis may be a primary function of these junctions in neurons.

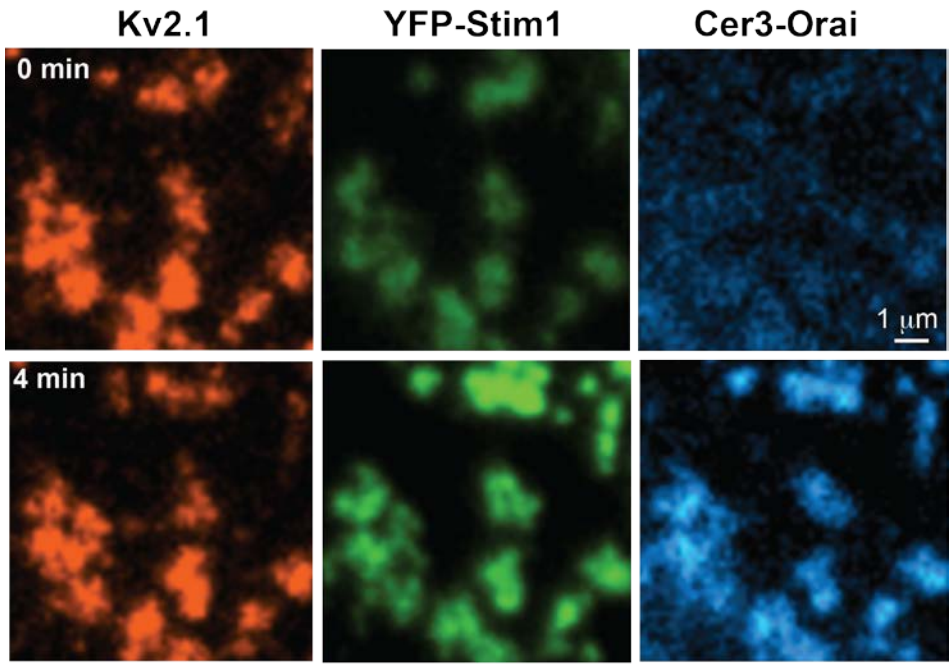

Figure 16: STIM1 and Orai1 assemble at Kv2.1-induced ER-PM junctions (clusters) following ER Ca^{2+} depletion. Zoomed-in images of the basal surface of an HEK 293 cell transfected with Kv2.1-HA (left panels, labeled with anti-HA-AlexaFluor594), YFP-STIM1 (middle panels) and Cerulean3-Orai1 (right panels) imaged using TIRF microscopy. The top row of images are taken from just before the application of 2uM thapsigargian (TG) and the bottom row is four minutes after TG. The YFP-STIM1 and Kv2.1 clusters co-localize initially due to the presence of STIM1 in the ER, while CER3-Orai1 is evenly distributed over the basal surface. After four minutes of TG, YFP-STIM had translocated to the Kv2.1-induced ER-PM junctions, increasing the YFP signal. CER3-Orai1 became localized to Kv2.1 and STIM1 containing junctions presumably by direct interaction with STIM1.

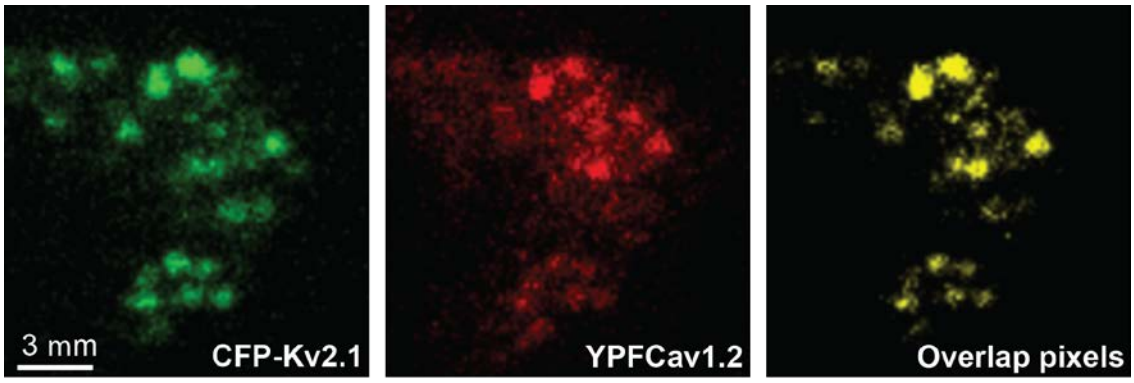

Figure 17: Cav1.2 localizes to Kv2.1 clusters in cultured rat hippocampal neurons. DIV 7 rHN transfected with CFP-Kv2.1 (left panel) and YFP-Cav1.2 (middle panel) and imaged using TIRF microscopy.

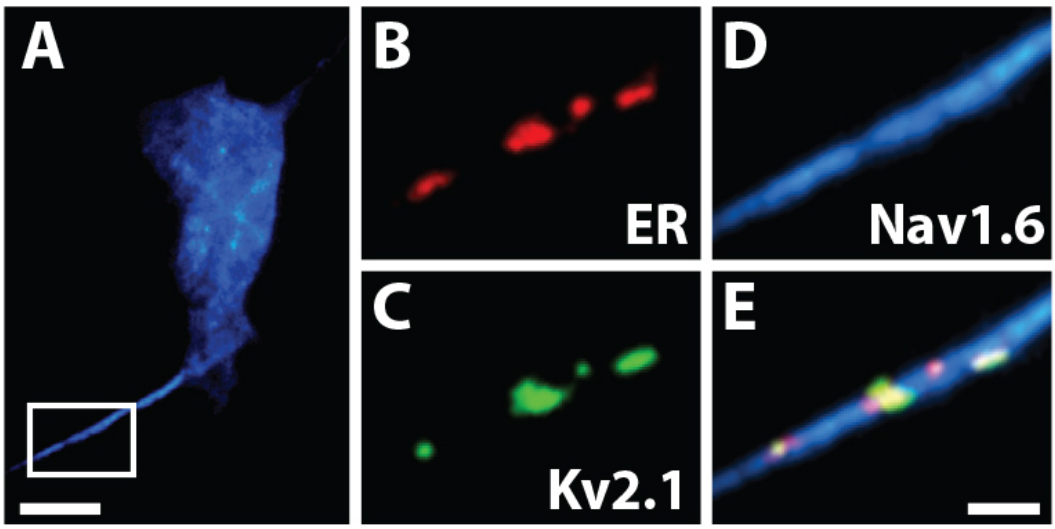

Figure 18. Kv2.1 induced ER/PM junctions are present at the axon initial segment (AIS) of cultured hippocampal neurons. A. Representative DIV 12 rHN imaged in TIRF, transfected with GFP-Kv2.1, DsRed2-ER, and Nav1.6-Cerulean3 (Scale bar = 5 µm). (B-E) Magnification of the AIS (white box). The ER (B, red) co-localizes with Kv2.1 clusters (C, green) in the AIS, which is denoted by the accumulation of Nav1.6-cerulean3 (D) (Scale bar = 2 µm).

Chapter 4: Plasma membrane domains enriched in cortical endoplasmic reticulum function as membrane protein trafficking hubs

Introduction

Trafficking of integral membrane proteins involves two separate but complementary processes; exocytosis mediated through SNARE complexes and endocytosis predominantly mediated by clathrin-coated pits (CCPs) (110, 111). In neuronal pre- and post-synaptic membranes these processes are tightly localized to allow for rapid neurotransmitter release and activity dependent synaptic plasticity (112-115). However, in other cell types the localization of both processes has been debated. While studies in BSC-1 cells suggested CCP initiation was randomly distributed over the cell surface during a 7 min observation period (116), CCPs have been shown to form, internalize and reform at the same location in COS-1 cells (117). The existence of stable "hot spots" for clathrin mediated endocytosis has now been described in many cell types (118-124). There are also examples of exocytosis reoccurring at stable sites in non-neuronal cells. In adrenal chromaffin cells exocytic release occurs at specific reusable sites (125-128) and recent studies of Glut4 trafficking suggest specialized plasma membrane (PM) domains in adipose cells are used for Glut4 delivery to the cell surface (129).

Recently, we demonstrated that cell surface microdomains occupied by a voltage-gated K^+ channel, Kv2.1, function as hubs for Kv channel trafficking to and from the plasma membrane in both HEK cells and cultured hippocampal neurons (51). The delivery of Kv2.1 to the cell surface occurred at the edge of these micron-size platforms, as did endocytosis. While it was perhaps not surprising that Kv2.1 would traffic at a location defined by the channel itself, we found that a completely unrelated K^+ channel (Kv1.4) was also delivered and retrieved at the Kv2.1 cluster perimeter. This finding suggested that the Kv2.1 clusters could function as generic endo- and exocytic platforms. Since the Kv2.1 clusters have been observed to localize with sub-surface

cisternae in hippocampal and motor neurons (18, 21), and to occasionally co-localize with RyRs (26), we explored the possibility that the Kv2.1 clusters preferred to localize over the cortical endoplasmic reticulum (cER), i.e. endoplasmic reticulum that resides within 100 nm of the cell surface.

Here we demonstrate using total internal reflection fluorescence (TIRF) microscopy in combination with multiple fluorescent markers for the endoplasmic reticulum (ER) that this is indeed the case, with most of the Kv2.1 clusters residing above the cER. This result in turn raised the question of whether PM regions enriched in cER function as trafficking hubs for a variety of membrane proteins. We observed that both transferrin receptor (TfR) and Kv1.4 recycling occur immediately adjacent to regions of the PM enriched in underlying cER, suggesting stable endo- and exocytic machinery surround these domains. In addition, nascent VSVG protein just released from the Golgi apparatus is delivered to the cell surface at these locations. Thus, cER enrichment defines PM domains which function as trafficking hubs for membrane protein transport to and from the cell surface.

Materials and Methods

Plasmid constructs, cell culture and transfections. Fluorescent protein, HA epitope and biotin acceptor domain (BAD) tagged Kv channel constructs have been described previously (16, 17, 69, 71) and are based on the Living Colors vector system (Clontech). The HA epitope or BAD sequence is contained within the extracellular domain between the first and second transmembrane domains of Kv2.1 and Kv1.4 (16, 80). When necessary the BirA biotin ligase in the pSec vector was cotransfected with Kv1.4 to achieve biotinylation during channel biosynthesis, presumably within the ER lumen (16). Transferrin receptor (TfR) modified with an extracellular super-ecliptic pHluorin (SEP) has been previously described (113). The temperature sensitive Vesicular Stomatitis Virus G protein (VSV-G, ts045) fused to YFP has also been

described previously (57). Clathrin light chain (CLC) with GFP or RFP fused to the C-terminus was a gift from Dr. Santiago Di Pietro (Department of Biochemistry and Molecular Biology, Colorado State University). The luminal ER marker pDsRed2-ER was obtained from Clontech.

HEK 293 cells (American Type Culture Collection, passage 38-45) cells were transfected with 1-3 µg of Kv channel DNA, 1µg of pSec Bir A, 100ng of CLC fusions, 500ng of TfR-SEP, 200ng of DsRed2-ER or 1ug of YFP-VSVG-ts045 using a BioRad Genepulser Xcell (BioRad Laboratories, Hercules, CA) with a 0.2 cm gap cuvette and a single 110 V 25 ms pulse. Transfected cells were plated on glass-bottom 35 mm dishes (Matek, Ashland, MA) that had been previously Matrigel-coated (BD Biosciences, San Jose, CA) and covered in DMEM + 10% fetal bovine serum. HEK cells were imaged within 24 h of electroporation in HEK physiological imaging saline consisting of (in mM): 146 NaCl, 4.7 KCl, 2.5 $CaCl_2$, 0.6 $MgSO_4$, 1.6 $NaHCO_3$, 0.15 NaH_2PO_4, 0.1 ascorbic acid, 8 glucose and 20 Hepes, pH 7.4 (imaging saline).

Confocal and TIRF microscopy. HEK cells and neurons expressing fluorescent protein tagged constructs were imaged with one of two microscope systems depending on the experiment performed. Standard 3D imaging, 0.3 µm z steps, was performed with an Olympus FV1000 confocal microscope equipped with spectral detectors and the SIM scanner. GFP was excited using the 488 nm line of an argon laser and emission was collected using the variable bandpass filter set at 500-530 nm. Alexa 594 fluorophores were detected using a 543 nm HeNe laser with the variable bandpass filter set at 600-630 nm. A 60X, 1.4NA oil immersion objective was used for imaging and the pinhole diameter set for the appropriate Airy unit when using one laser. An intermediate pinhole diameter was used when two fluorophores were being detected simultaneously. For each image, the detector voltage was adjusted as necessary to utilize the full 12-bit range.

To image Qdot recycling and ER/PM junctions we used a Nikon Eclipse Ti Perfect-Focus equipped TIRF/widefield fluorescence microscope equipped with AOTF controlled 405, 488, 543 nm diode lasers, 100 mW each, and an Intensilight wide-field light source. A 100X PlanApo TIRF, 1.49 NA, objective was used for image acquisition. Emission was collected through a Sutter Lambda 10-3 filter wheel containing the appropriate band pass filters. The stage and objective are temperature controlled via a Zeiss/Pecon stage heating insert and objective heater at 37°C. This microscope is equipped with the Andor iXon EMCCD DU-897 camera, 512x512. For all imaging experiments, the cells were on the microscope stage for less than one hour.

cER domain localization. The majority of experiments used DsRed2-ER expression to illuminate the cER in TIRF with a calculated penetration depth of 63nm. The cER enriched domains were delimited by an automated object finding algorithm (Volocity, 6.1.1, Waltham, Ma) and cER perimeter calculated automatically. Neither exocytic events nor clathrin related structures were observed to localized directly over the cER, so the area occupied by the cER enriched domains was not included in the calculation of cER perimeter. For confocal imaging, cells were labeled for 10min at 37°C with ER-Tracker Green, then washed 3x with imaging saline and imaged at 37°C

Antibody and quantum dot labeling. HEK cells were labeled in imaging saline containing an anti-HA monoclonal antibody conjugated to Alexa594 (1:1000 dilution) for 5 to 10 minutes at 37°C before being rinsed and imaged at 37ºC. Quantum dot recycling assays were performed essentially as described previously (51). Briefly, cells expressing biotinylated Kv1.3 or Kv1.4 constructs were first incubated in 1% BSA (Sigma, IgG/fatty acid-free) in imaging saline for 5 min and then incubated for 5 min with 0.1 nM streptavidin-conjugated quantum dots (QD605, Invitrogen) in imaging saline containing 1% BSA. The cells were then rinsed extensively with imaging saline and returned to the tissue culture incubator. All incubations were performed at

37°C. To control for nonspecific quantum dot (Qdot) binding we imaged cells expressing GFP-Kv1.4-loopBAD that were not co-transfected with the BirA biotin ligase.

Detection of Kv1.4 recycling. The dissociation rate of biotin-streptavidin binding is relatively slow, with 4 and 25% dissociation over 1 h at 37°C for biotin-conjugates or biotin, respectively (130, 131). This slow dissociation rate, combined with the lack of photobleaching and low potential for biological degradation (132, 133), make Qdot labeling useful for tracking individual Kv channels to and from the cell surface. HEK cells expressing biotinylated Kv1.4 channels were labeled with Qdots at low efficiency as described above and then returned to the tissue culture incubator for 1-2 h to allow endocytosis and recycling to the cell surface to approach steady-state. The cells were then removed from the incubator and imaged using the TIRF system described above. Spontaneous Qdot appearance represents a cytoplasmic channel previously on the cell surface now entering the 100 nm TIRF illumination field, i.e. approaching or inserting into the membrane. Observation of the expected single channel diffusion in the membrane confirmed surface delivery (51). Spontaneous loss of a cell surface Qdot represents a channel undergoing endocytosis.

Image presentation and data analysis. Images were imported into Volocity 6.1.1 software for 3D reconstruction, object detection/tracking and quantitative analysis. Numerical data were exported into Origin Pro 8.5 for further analysis and curve fitting. Image sequences were analyzed for the location of Qdot appearance, i.e. membrane insertion, or disappearance, i.e. endocytosis, by both manual inspection and an automated analysis. In the case of the manual analysis, Qdots that appeared or disappeared within 2 µm of the cell perimeter were not counted due to concerns that they may be just entering or leaving the basal cell surface. Qdots were classified as entering or leaving the surface at the cER if the appearance or disappearance occurred within 0.15 µm of the cER perimeter. Potential dark states less than 60 s were most problematic and were dealt

with as described previously (Deutsch *et al.*, 2012). Only Qdot appearances that occurred more than 60 s following the disappearance of a Qdot within a 1 µm radius where counted as indicating surface insertion, as opposed to representing detection of the same Qdot emerging from a dark state. The same logic applied to Qdots that disappeared only to be followed by reappearance in less than 60 s less than 1 µm away, i.e. these Qdots were not counted as being internalized by the cell.

For the automated detection and tracking of Qdot labeled Kv1.4 channels we used a multiple-target tracking (MTT) approach based on the algorithm developed by Serge et al (134, 135) and described previously (51). This analysis provides the positions and intensities for each of the targets throughout the entire video duration, allowing for determination of the time and location of newly arriving channels to the cell surface. Using the results of the MTT algorithm, Qdot tagged Kv1.4 channels that arrived to the cell surface after a delay relative to the start of the image sequence (to allow for potential Qdot dark states) were categorized as arriving to the cER or not. This classification was determined by overlaying the individual Qdot tagged channel signal with the thresholded DsRed2-ER signal along with the MTT algorithm trajectories. If the channel arrived within one pixel of the cER perimeter (1 pixel = 160 nm) it was categorized as arriving to the ER, and similarly for channels not arriving to the cER. Channels that appeared to diffuse from the side of the cell to the basal surface were discarded.

TfR-SEP Exocytosis. HEK cells or neurons were transfected with TfR-SEP and DsRed2-ER 18-24 hrs prior to imaging at 37°C. Basal SEP fluorescence was bleached for 1 min in TIR using 100% 488nm laser power. SEP and DsRed fluorescence were imaged at a rate of 2hz and 0.1hz respectively until SEP fluorescence recovered to a point where additional exocytic events were masked. The center of each exocytic event, based on pixel intensity, was manually detected.

YFP-VSVG-ts045 exocytosis. HEK cells transfected w/ YFP-VSVG-ts045 and DsRed2-ER were cultured at the non-permissive temperature of 40°C for 12-16hrs prior to imaging and shift to the permissive temperature of 32°C. YFP and DsRed2 were imaged in TIR at a rate of 2 hz and 0.1 hz respectively. Vesicles were tracked manually in Volocity.

Thin-section electron microscopy. HEK cells were grown on carbon-coated glass coverslips coated with matrigel and fixed with 2.5% gluataraldehyde in 0.15M phosphate buffer, pH7.4. Coverslips were en bloc stained with aqueous uranyl acetate, postfixed with osmium tetroxide and dehydrated with ethanol before embedding in Epon. The carbon-coat affixed to the embedded cells allowed for unambiguous orientation of the basal surface of the HEK cells for ultramicrotomy. Ultra-thin sections (<100nm) were mounted on copper grids and were imaged with a JEOL 1400 TEM.

Generation of Euclidean distance maps. Locations of TfR were determined using U-track algorithm. To generate the Euclidean distance maps (EDMs), images of the ER were processed using ImageJ (National Institutes of Health, http://imagesj.nih.gov/ij/) in a two-step process that includes image segmentation followed by actual EDM transform. First, a value representing the level of extracellular background noise was subtracted from the image. Then, in order to correct for heterogeneous background arising from cellular autofluorescence, the local background was found using a 20-pixel Gaussian filter and it was subsequently subtracted from the original image. Next, images were convolved with a 5x5 Laplacian kernel which acted as an edge detector to extract ER features. Images were zoomed by a factor of 10 using bicubic interpolation, which allowed for a higher accuracy in the final EDM. The images were then converted to binary by thresholding. The EDM was generated by inverting the image and using the Distance Mapping operation in MATLAB (MathWorks, Natick, MA). We used a custom-written algorithm to extract the pixel value of the EDM at the site of TfR exocytosis. Control values were determined by

selecting all EDM values within an ROI encompassing either the entire TIRF footprint (determined using low-level TfR fluorescence as a mask for the cell region) or only the region most highly enriched in ER. For the local ER network analysis, the ROI was hand-drawn around the ER. Distances from the ER were imported into Origin 8.6 (OriginLabs, Northampton, MA) for further analysis.

Statisitics. Data are presented as the mean± sd unless otherwise indicated. Co-localization statistics were calculated in Volocity 6.1.1 (Waltham, MA) only from intensity values within thresholds using the Pearson's correlation coefficient as previously described (136). Cumulative distribution functions of the distances to the cER were generated using a bin size of 75 nm. The distributions of the EDM and the distances from the delivery locations to the cER were compared using a two sample t-test.

Results

Cell surface Kv2.1 clusters are located at sites of cER enrichment. We first sought to determine whether Kv2.1-enriched trafficking hubs, that are specialized sites for Kv channel exo- and endocytosis (51), are associated with specific intracellular structures, especially since previous studies suggested that Kv2.1 was often localized near sub-surface cisternae (18). We therefore tested whether surface Kv2.1 clusters co-localized with peripheral ER projections. Figure 19A shows the relationship between surface Kv2.1 channel aggregates, detected via AlexaFluor 594 conjugated antibody binding to an extracellular epitope inserted into Kv2.1 (red), and the ER as detected with ER-Tracker Green. This confocal section of a transfected HEK cell suggests a relationship between the surface clusters and the ER, with the clusters appearing at the end of finger-like projections of the cortical ER network as highlighted by the yellow arrows in Figure 19B. To confirm cER proximity at sites of Kv2.1, we used TIRF-based imaging to selectively visualize surface Kv2.1 and cER.

HEK cells were transfected with GFP-Kv2.1 and DsRed2-ER to highlight the ER lumen and the representative images shown in Figures 19C-F indicate that the majority of the Kv2.1 clusters colocalized with the ER marker within the TIR illumination field. Figure 19F is derived from only pixels with overlapping Kv2.1 and ER fluorescence and illustrates the surface distribution of the Kv2.1-cortical ER interface. Kv2.1/ER colocalization was also observed when ER membrane proteins such as YFP-Stim1 were used to illuminate the ER (data not shown). Figure 20 shows that this Kv2.1 cluster localization over the ER is also observed in cultured hippocampal neurons. Since we had previously shown that Kv2.1 surface clusters are sites for the exo- and endocytosis of Kv channels, we next asked whether cER enrichment defined PM domains that function as generic hubs for the trafficking of membrane proteins.

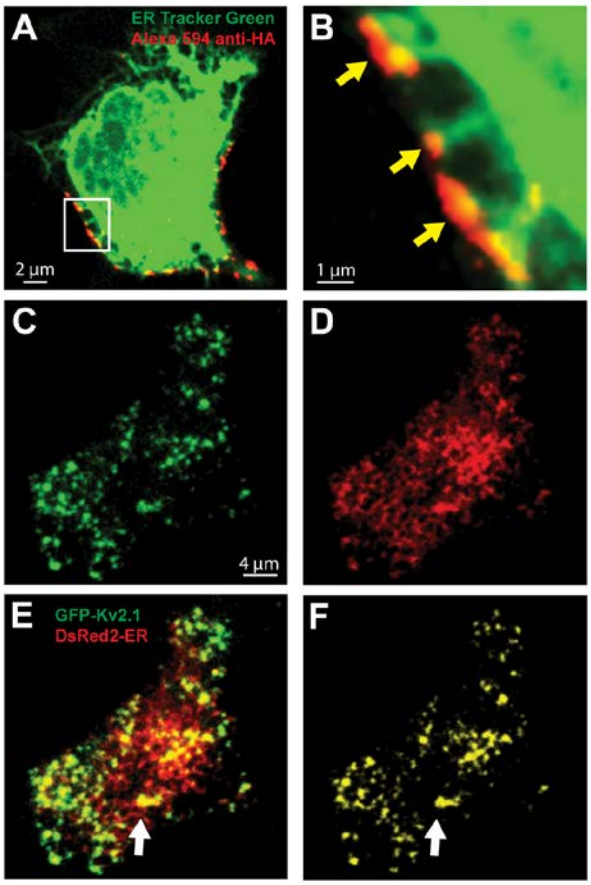

Figure 19. Kv2.1 cell surface clusters colocalize with the ER at the cell surface. (A) Confocal based detection of Kv2.1-ER colocalization. Shown is a single confocal plane through the middle of a HEK cell transfected with Kv2.1HA. The ER was stained with ER Tracker Green and the red shows Alexa594-conjugated anti-HA labeling of live cells to detect only surface Kv2.1 channels. (B) Enlargement of the boxed region in Panel A illustrating the association of the Kv2.1 surface clusters (arrows) with cortical ER finger-like projections. (C-E) TIRF based detection of Kv2.1-cER colocalization. HEK cells were transfected with GFP-Kv2.1 and DsRed2-ER and the corresponding fluorescence patterns illustrated in panels C and D, respectively. (F) Pixels containing both fluorescence signals. The thresholded Pearson's correlation coefficient for the cell in panels C-F was 0.61. For eight similar cells examined in TIRF, the correlation coefficient was 0.71± 0.07 (mean± sd).

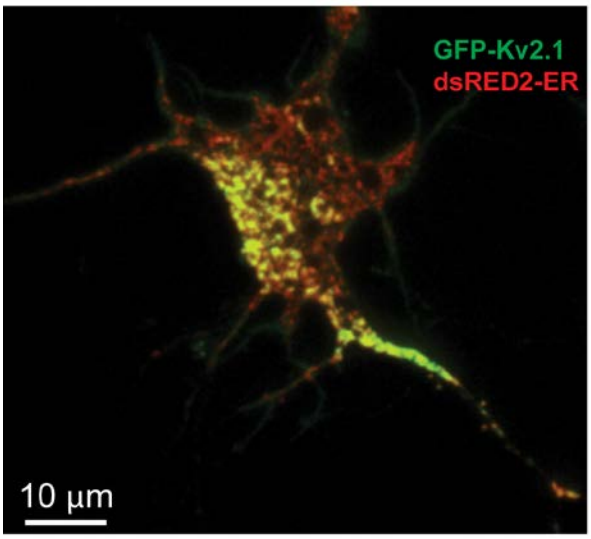

Figure 20. TIRF based detection of Kv2.1-ER colocalization in cultured hippocampal neurons. Cells were transfected with GFP-Kv2.1 and DsRed2-ER. The yellow represents pixels containing both the green and red fluorescence.

cER enriched PM domains are the preferred site of transferrin receptor exocytosis. In order to observe exocytosis of a prototypical recycling membrane protein we expressed the transferrin receptor (TfR) fused to the pH-sensitive GFP variant superecliptic pHluorin (TfR-SEP) in HEK cells (113, 137). The SEP protein is attached to the extracellular domain of the TfR so that its fluorescence is quenched by the low pH of the endosome lumen. Trafficking vesicle fusion with the plasma membrane generates a burst of SEP fluorescence as the acidic pH is neutralized by the extracellular solution. This event is followed by lateral TfR diffusion in the plasma membrane and dispersal from the site of exocytosis. An example of one such exocytic event is shown in Figure 21A. A bright punctum suddenly appears adjacent to the cER (marked by DsRed2-ER) and disperses as the TfR-SEP diffuses away from the exocytic site over the next 1-2 s. To enhance the signal to noise ratio of delivered TfR-SEP, the basal membrane was first bleached with high power TIR illumination to reduce membrane fluorescence derived from cell surface TfR-SEP. Figure 21B, left panel, shows a TIRF image of TfR-SEP and DsRed2-ER prior to TIR-based photobleaching. The next three panels show individual bright puncta (yellow arrows) representing trafficking vesicles arriving post bleach. The right panel of Figure 21B summarizes the location of the delivery events over the 6 min imaging session.

In this example, 93% of the exocytic events occurred within 0.3 μm (2 pixels) of the cER perimeter. Overall, 82±12% (mean±sd, n=560, from 21 cells) of the TfR-SEP exocytosis events were adjacent to the cER near the plasma membrane. Exocytic events occurred either adjacent to or away from the cER enriched regions, but never directly over the cER. For this reason, we measured the area occupied by only the perimeter of the cER, including a 0.3 μm zone outside the perimeter. The cER perimeter (0.3 μm) in these cells accounted for only 28±8% of the cell footprint.

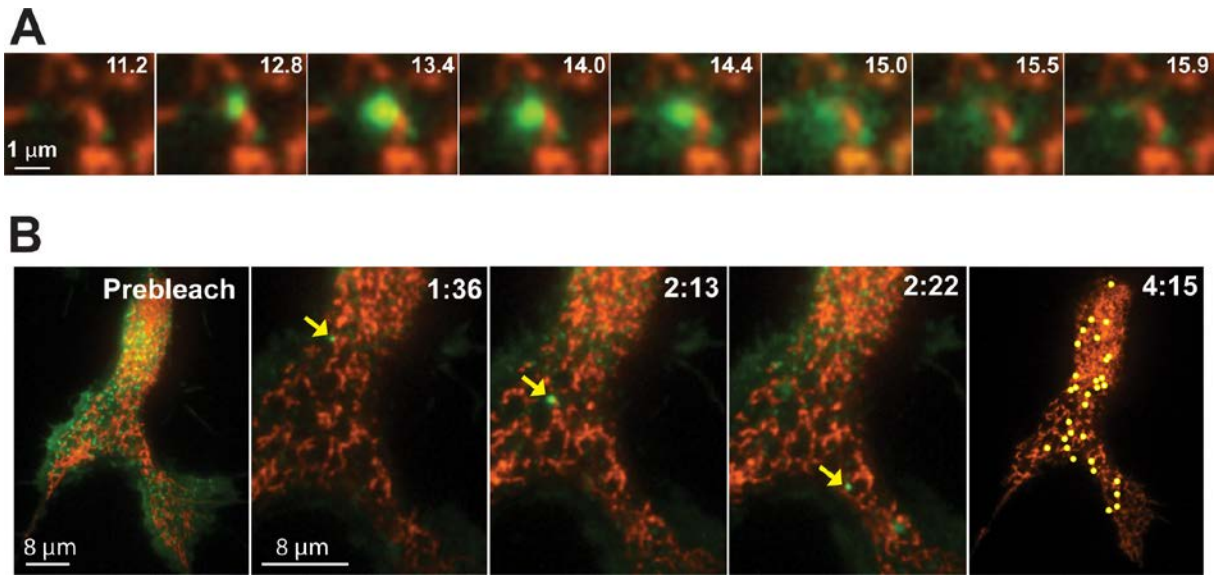

Figure 21. TfR exocytosis occurs at cER enriched domains. (A) Time course of a single TfR-SEP exocytic event. Shown are TIRF images acquired over the indicated time series. (B) Localization of TfR-SEP exocytosis sites. Left panel shows a TIRF image with the TfR-SEP localized to both the cER-associated puncta and the general plasma membrane. In order to enhance the signal to noise ratio of delivered TfR-SEP the basal membrane was first bleached with high power TIR illumination to reduce both the puncta intensity and, most importantly, the general membrane fluorescence derived from freely diffusing TfR-SEP molecules. The next three panels show single bright puncta (yellow arrows) representing trafficking vesicles arriving post bleach. The right panel summarizes the location of the delivery events observed up until the general membrane fluorescence became too bright to detect additional delivery. Sites of exocytosis are marked by the yellow circles.

This indicates that the cER localized delivery is not simply random, i.e. the occurrence of TfR fusion is disproportionately high at PM domains that are in close apposition to the cortical ER. This observation was true not only for regions underneath the nucleus where the cER is generally located, but also for peripheral regions. In these regions, 84± 7% (n=5) of TfR-SEP delivery occurred within the cER perimeter, which only accounted for 31± 9% of the cell area. Similar findings were obtained with cultured hippocampal neurons as illustrated in Figure 23A. As an additional control for random association with the cER perimeter we expressed biotinylated Kv1.3 K^+ channels in HEK cells with the DsRed2-ER marker and labeled single channels with Qdots. Kv1.3 shows an evenly distributed localization on the cell surface and rapidly diffuses throughout the TIRF footprint. As illustrated in Figure 22, Qdot-labeled Kv1.3 channels have a random distribution with no relationship to the cER. Importantly, using our counting method, 42±14% of Qdot labeled Kv1.3 channels were located within 0.3 μm of the cER which occupied 41±5% of the cell footprint (n=779 Qdots in 6 cells). Together these data suggest that cER enriched domains coordinate exocytosis machinery involved in surface protein delivery. Indeed, syntaxin 4 (Syx4), which is involved in neuronal exocytosis (113), favors areas near the cortical ER as illustrated in Figure 24. In 13 cells co-expressing Syx4-HA and DsRed2-ER, 68±11% of stable Syx4 clusters were located within 0.3 μm of the cER perimeter while the cER perimeter represented 35± 8% of the cell footprint.

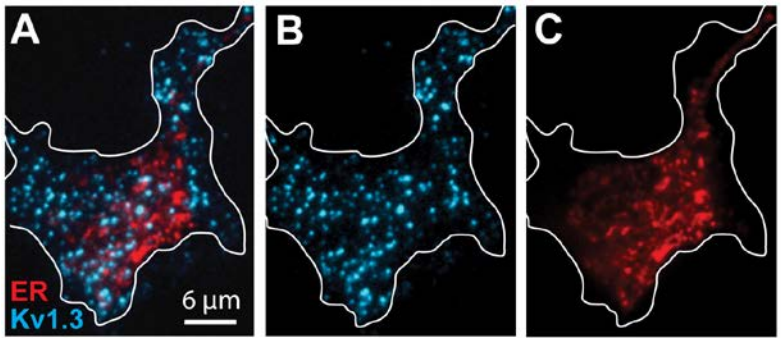

Figure 22. Distribution of individual Qdot-labeled Kv1.3 channels relative to cER perimeter labeled with DsRed2-ER. (A) TIRF image of Qdot labeled Kv1.3 channels (blue) and DsRed2-ER fluorescence. (B and C) Individual cER and Kv1.3 fluorescent patterns, respectively. The cell perimeter is outlined. In this cell 31% of the Qdot labeled Kv1.4 were at the cER perimeter which accounted for 29.8% of the cell footprint. Overall, the area of a 0.3 μm cER perimeter occupied 40±5% of the cell footprint, while 42±14% Kv1.3 Qdots were found at this region (n=779, in 6 cells).

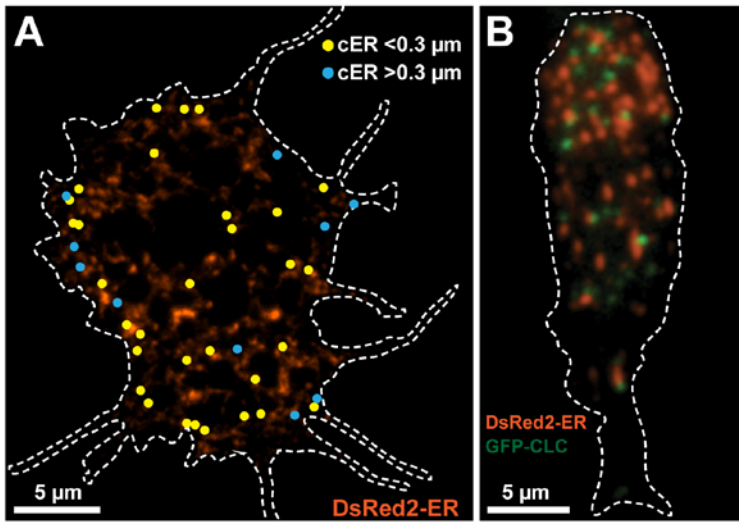

Figure 23. TfR exocytosis and GFP-CLC in hippocampal neurons. Rat hippocampal neuron cultures were transfected on DIV 4-5 and imaged via TIRF on DIV 6-8 with either DsRed2-ER and TfR-SEP (A) or DsRed2-ER and GFP-CLC (B). (A) Summary figure of TfR-SEP exocytic events. Yellow dots mark events occurring within 0.3µm of the cER perimeter and blue dots mark events occurring outside of the cER perimeter. Red indicates DsRed2-ER fluorescence from a single frame. In this cell, 41 out of 51 events occurred within 0.3µm of the cER perimeter, which accounted for 25% of the footprint of the cell. Overall, 70±11% of events (n=386, from 8 cells) occurred within 0.3µm of the cER perimeter, which accounted for an average of 34±15% of the cell footprint. (B) Representative image of the association between GFP-CLC puncta and the cortical ER. Overall, 83±4% of CLC puncta (n=515, in 7 cells) were located within 0.3µm of the cER perimeter which accounted for 32±8% of the TIRF footprint.

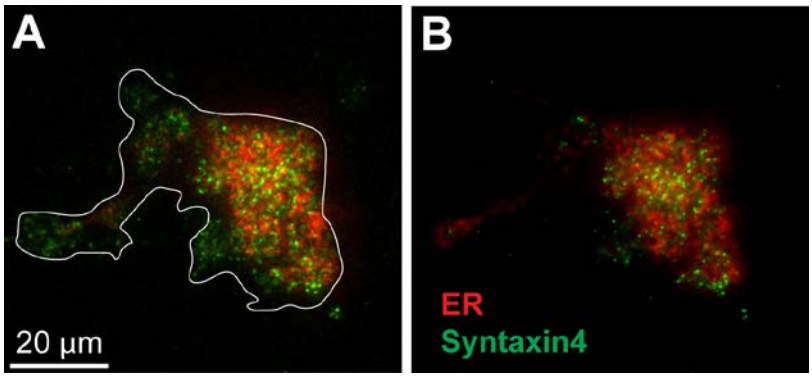

Figure 24. Syntaxin4 clusters favor the cortical ER. HEK cells were transfected with Syntaxin4-HA and DsRed-ER and 12-18 hrs later labeled with AlexaFluor488-conjugated anti-HA monoclonal antibody. (A) A single TIRF image shows green puncta representing concentrations of syntaxin4 molecules that are present both near the cortical ER and in places where cER is absent. These puncta were observed with and without prior fixation indicating they do not represent antibody-induced clustering. Time-lapse imaging showed that there were two populations of syntaxin4 puncta, one highly mobile and the other relatively static. (B) Time compression indicates stable syntaxin4 localization favors the cortical ER. A 200 frame time series from the cell in (A) was compressed into a single image plane (average intensity). The highest syntaxin4 intensity is now associated with locations where there is the least movement as mobile syntaxin4 does not remain in place long enough to appear in the thresholded compression. In 13 cells co-expressing syntaxin4-HA and DsRed2-ER 68±11 % of the stable syntaxin4 clusters were within 0.3 µm of the ER while the ER perimeter represented 35±8 % of the cell footprint.

TfR exocytosis adjacent to the cER is statistically significant. In order to generate quantitative statistics demonstrating that the TfR exocytic sites are truly associated with the location of the cortical ER we adopted the use of Euclidean distance maps (EDM) (138). To our knowledge this is the first application of this image processing approach to cell biology. EDMs are generated from a binary image such that the features of interest, in our case cER structure, have a value of 0 ("off") and all other pixels have a value of 1 ("on"). The binary images were generated from filtered, thresholded, and zoomed TIRF images similar to those illustrated in Figure 21B. The Euclidean distance mapping operation starts at the 0 values and sets all unassigned neighboring pixels to 1. The process then repeats iteratively, setting all unassigned neighbors of the pixels with a value of 1 to 2, their unassigned neighbors of pixels with a value of 2 to 3, and so on, until all pixels in the image have been assigned a value. This simple operation results in a new image where each pixel value is the distance of that pixel to the nearest image feature, i.e. the distance to the cER. TfR puncta were detected and localized at the moment of appearance using the U-track algorithm (139). Each delivery event was manually checked to ensure that only true exocytosis (as illustrated in Figure 21A) was analyzed. In addition, the selection was done without prior knowledge of cER location to avoid introducing human bias. The distance between delivery localization and the cER was then computed from the EDM and the distribution of delivery distances from the cER was built.

If delivery to the plasma membrane occurred at random locations, independent of the ER, the distribution of distances between delivery location and cER would be, within statistical error, indistinguishable from the distribution of the EDM. This is a consequence of the EDM being the distribution of distances to the cER as computed for the pixels in the whole membrane image. Figure 25A shows the cumulative distribution function (CDF) of the distance between delivery and the cER as compared to the CDF of the distances of random pixels as obtained when the EDM of the entire TIRF footprint was used.

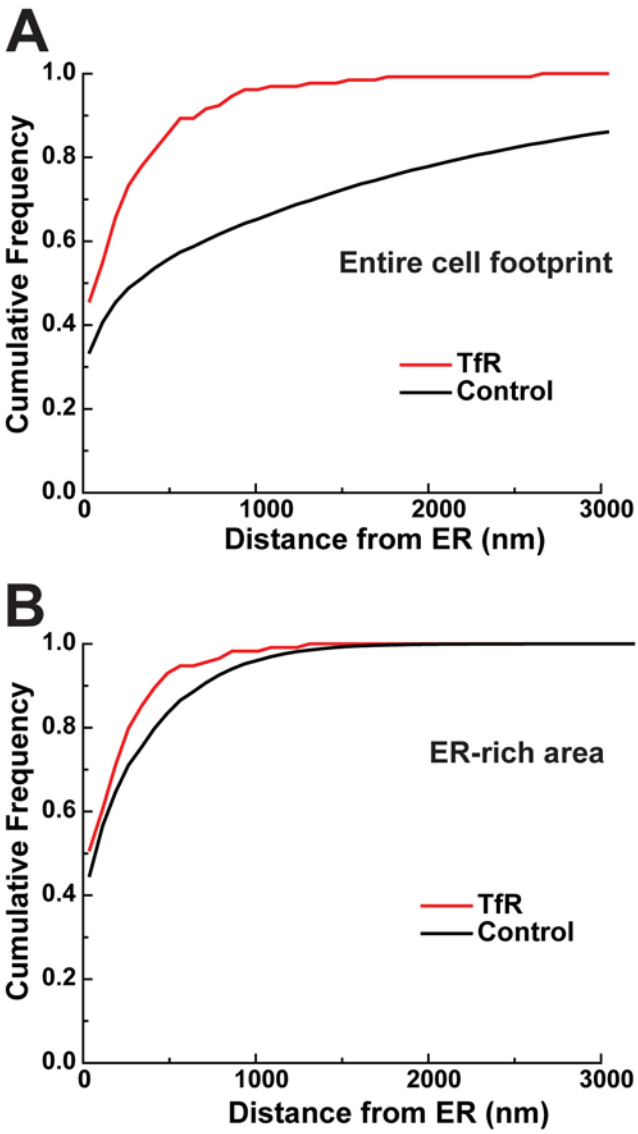

Figure 25. Euclidean distance mapping analysis of the sites of TfR exocytosis relative to the cER perimeter. Cumulative distribution functions (CDFs) comparing the distance of TfR exocytic sites from the cER (red) to the control case (black). Distances from the cER were determined by Euclidean distance maps (EDMs) generated from images of the cER. (A) Summary data obtained using the entire TIRF footprint as determined from the low-level TfR fluorescence. The curve for the TfR plots the cumulative individual distances between the ER and exocytic locations. The control curve summarizes the distance to the ER for all the pixels present. The mean distance from the ER for TfR delivery was 0.25± 0.38 μm (mean± sd, n=131, from 5 cells) while for the control pixels the distance was 1.5± 2.6 μm, $p<0.0001$. (B) Results derived from the region of the cell footprints highly enriched in cER. The mean distance from the cER for TfR delivery was 0.17±0.24 μm (n=114, from 5 cells) while for the control pixels the distance averaged 0.25 ± 0.33 μm ($n=1.1 \times 10^7$ pixels), $p<0.05$ assuming equal variance. The image crop forces the two curves together since now all pixels are relatively close to the ER.

The separation of the experimental and control curves indicates a clear preference for exocytosis at the cER, with 75% of the delivery events occurring within 0.25 μm of the cER perimeter while the control curve generated from all the pixels in the footprint shows 75% of these pixels were within 1.75 μm of the ER. The mean distance from the ER for TfR delivery was 0.25± 0.38 μm (mean± sd, n=131, from 5 cells) while for the control pixels the distance was 1.5 ± 2.6 μm, $p<0.0001$. The control curve was generated from 1.05×10^7 pixels. However, one could argue that delivery simply preferred the general region of the basal cell surface that was enriched in cER with no direct association with the cER itself. Therefore, we repeated this EDM analysis on regions of interest highly enriched in cortical ER (Figure 25B). The results in cER-dense regions again indicate a preference for the cER. The separation between the curves is naturally reduced since the control pixels are now on average closer to the ER in the cropped images. The mean distance from the cER for TfR delivery was 0.17±0.24 μm (mean±sd, n=114, from 5 cells) while for the control pixels the distance was 0.25 ± 0.33 μm, $p<0.01$ assuming equal variance.

TfR is preferentially endocytosed at cER enriched PM microdomains. When TfR-SEP was used to monitor exocytosis we noticed it formed small puncta which frequently associated with the cER (Figure 26A & B). These puncta are likely on the cell surface, since the SEP fluorophore is pH-sensitive. Overall 88.7±5.5%, n=2609 from 21 cells, of the TfR puncta were within 0.3 μm of the cER perimeter as detected with DsRed2-ER. The cER perimeter occupied 29±8% of the cell footprint in these cells. Figure 26C illustrates the dynamics of the TfR-SEP puncta, where these structures repeatedly form in the same surface region before suddenly disappearing due to endocytosis and removal from the TIR illumination. All puncta in Figure 26C are TfR aggregates.

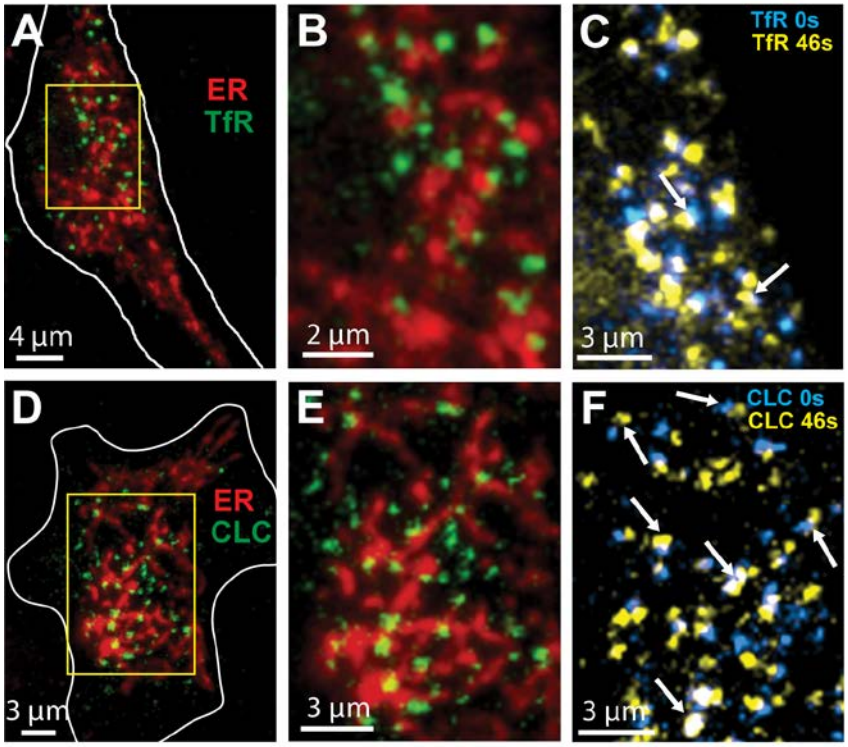

Figure 26. TfR and clathrin puncta localize adjacent to cER enriched domains. (A) HEK cells were transfected with TfR-SEP and DsRed2-ER and then imaged using TIRF optics. The green TfR puncta are most often seen adjacent to, but not overlapping with, the cER marker. (B) Enlargement of the boxed region in panel A. (C) TfR puncta present at two time points 46 s apart. Puncta present at 0 time are cyan while those visible 46 s later are in yellow. The arrows point to puncta that either did not change or diffused a short distance (White). However, most puncta disappeared only to reform nearby over the 46 sec. (D) HEK cells were transfected with GFP-clathrin light chain and DsRed2-ER prior to TIRF imaging. (E) Enlargement of the boxed region in panel D. (F) CLC puncta detected 46 s apart as described for (C).

The cyan and yellow puncta are derived from two video frames separated by 46 s. In most cases adjacent blue and yellow puncta represent distinct TfR populations that disappeared and then reappeared in the same general region. When appearance was exactly in the same position the color overlay is white. However, puncta lifetimes were variable as was puncta mobility and the white arrows denote puncta that did not disappear during the 46 s, sometimes moving and sometimes remaining stable.

Endocytosis of TfR is clathrin dependent and TfR clustering in CCPs has been observed in numerous cell types (122, 140-142). This led us to examine the relationship between CCPs and the cER. When GFP-clathrin light chain (GFP-CLC) was expressed in HEK cells with DsRed2-ER, diffraction-limited GFP-CLC puncta were frequently associated with the perimeter of the cER, reminiscent of the localization of TfR-SEP puncta (Figure 26D and E). The GFP-CLC puncta had lifetimes ranging from 5-100s, were mobile within a small radius and often reformed within the same membrane region as illustrated in Figure 26F, consistent with previously published reports of CCP behavior (116, 117, 119, 143). Overall, 88±5% of the GFP-CLC puncta were within 0.3 μm of the cER perimeter (range 80-94%, n = 1445 from 10 cells). In these cells the area encompassing the 0.3 μm surrounding the cER perimeter represented 44±9% of the cell area suggesting a robust preference for the cER enriched domains. A similar relationship was observed in cultured hippocampal neurons (Figure 23B). When TfR-SEP and RFP-CLC were cotransfected, the TfR-SEP puncta often colocalized with RFP-clathrin (Figures 27A-D), confirming that many of the TfR-SEP puncta represent clathrin-based endocytic sites as described in other cell types (117, 121). Even though the absolute intensities varied between puncta containing both TfR-SEP and RFP-CLC, the ratio of TfR-SEP to RFP-CLC fluorescence was relatively constant at 2.3 ± 0.4 (Figure 27E), consistent with previous reports demonstrating that CCPs grow as they accumulate cargo (143-145). Taken together, the data presented in Figures 26 and 27 strongly suggest TfR endocytosis occurs at stable, reusable sites adjacent to cER enriched domains.

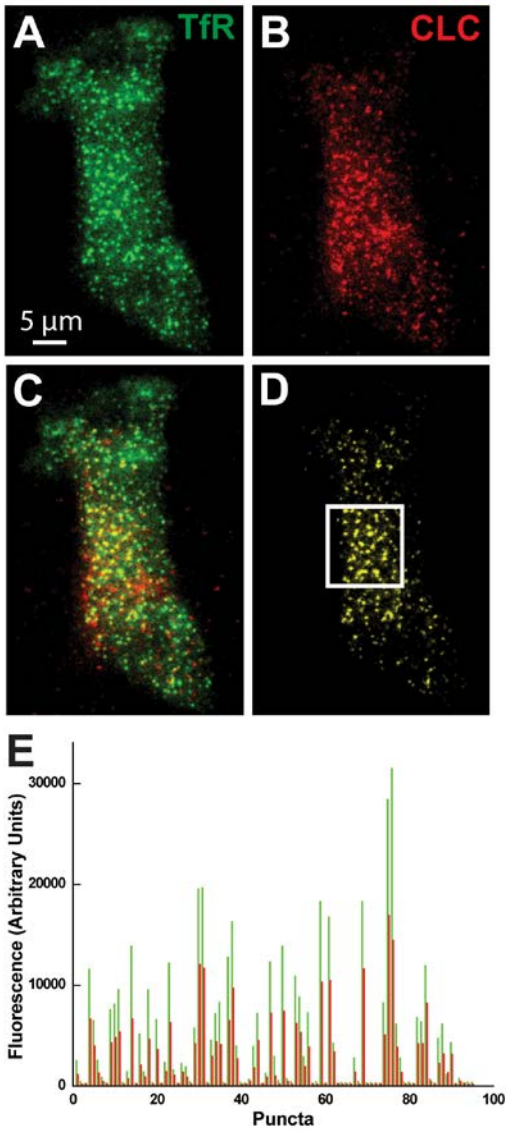

Figure 27. TfR-SEP and GFP-CLC puncta colocalize. (A and B) TIRF fluorescence pattern following transfection with TfR-SEP and RFP-CLC, respectively. (C) Traditional overlay of the TfR and CLC fluorescent signals. (D) Pixels containing only both fluorescence signals. (E) Ratio of TfR-SEP and RFP-CLC fluorescence of the puncta contained within the boxed region of panel D.

Delivery of post-Golgi carriers to the plasma membrane occurs at the perimeter of cER enriched PM domains. In the case of the TfR, the measured exocytosis reflects the delivery of a recycling membrane protein as opposed to a nascent protein trafficking directly from the Golgi to the cell surface. Thus, the vesicles harboring these two different cargoes may be delivered to different microdomains on the cell surface. To examine the exocytic location of newly synthesized membrane proteins we expressed a YFP-tagged, temperature-sensitive mutant of the vesicular stromatitis virus G-protein (YFP-VSVG-ts045) which remains unfolded in the ER at 40°C. Upon switch to the permissive temperature (32°C) VSVG-ts045 can traffic through the Golgi network where it buds off into vesicles, which ultimately fuse with the plasma membrane (57, 123, 124). This creates a large number of exocytotic events against a relatively non-fluorescent background enabling the identification of the site of exocytosis even without the aid of a pH-sensitive fluorescent protein. Exocytosis was examined in HEK cells expressing both DsRed2-ER and YFP-VSVG-ts045 following the shift to the permissive temperature. Figure 28A shows a HEK cell with blue dots marking the exocytic events which occurred within 0.3µm of the cER perimeter and yellow dots marking exocytic delivery >0.3µm from the cER perimeter. Figure 28B summarizes the location of exocytosis over time. Out of 52 exocytic events recorded in this cell, 46 of them occurred within 0.3µm of the cER perimeter (only the first 33 events are illustrated in Figures 28A & B). The majority of vesicles in this cell (36 of 52) appeared first at the cER perimeter, immediately followed by fusion at the cER or transient docking prior to fusion. However, in 9 of 52 of these exocytic events, the vesicle appeared first at one cER perimeter before moving to a distant cER perimeter to fuse. This behavior is illustrated in Figures 28C which shows a vesicle track (yellow line) following arrival at the cER perimeter (white circle). The fusion or delivery site is indicated by a red X. Together, these behaviors indicate that vesicles destined for fusion first appear in the TIRF field adjacent to cER enriched domains.

Generally, vesicles undergo fusion near the same cER domain where they first appeared. Vesicles which do not undergo fusion at the cER domain where they first appeared undergo fusion at a distant cER domain. Overall, 84±12% of exocytic events (n=213, from 7 cells) occurred within 0.3µm of the cER indicating a high degree of association between exocytosis and cER enriched domains. The cER perimeter (0.3µm) in these cells was 28±8% of the area of the TIRF footprint, again indicating that the cER localized delivery is not simply random.

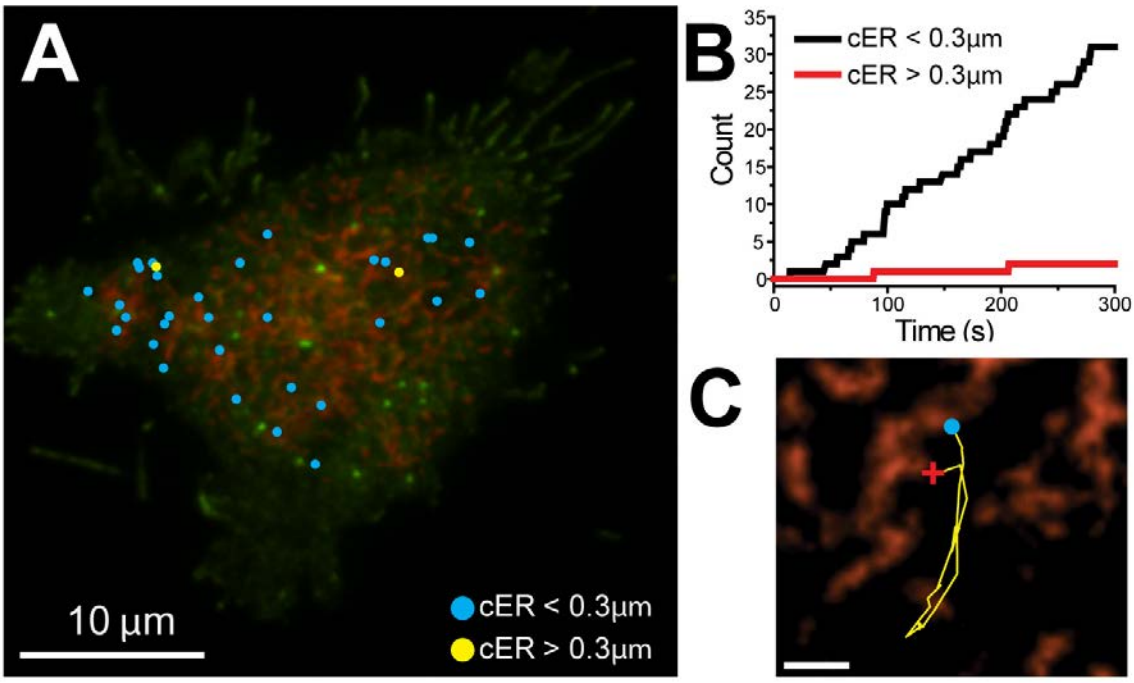

Figure 28. Exocytosis of VSVG-ts045 occurs predominantly at the cER perimeter. (A) HEK cell transfected with YFP-VSVG-ts045 and DsRed2-ER and imaged via TRIF microscopy at the permissive temperature (32°C). Yellow dots mark exocytic events which occurred ≤0.3µm from the cER perimeter and blue dots mark events which occurred >0.3µm from the cER perimeter. Out of 52 exocytic events recorded in this cell, 46 of them occurred within 0.3µm of the cER perimeter (only the first 33 events are illustrated in Figures 28A & B). (B) Summary of the location of YFP-VSVG-ts045 vesicle fusion over time. Same cell as in (A). Overall, 84±12% of exocytic events (n=213, from 7 cells) occurred within 0.3µm of the cER perimeter. The cER perimeter (0.3µm) in these cells was 28±8% of the area of the TIRF footprint. (C) Magnification of DsRed2-ER fluorescence from Figure 28A overlaid with a track of vesicular movement (yellow line). Appearance of the vesicle at the PM is marked with a white circle and exocytosis within 0.3µm of the cER perimeter is marked with a red X.

Recycling Kv1.4 potassium channels are both delivered to and retrieved from the cell surface near cER enriched PM regions. We previously demonstrated that the Kv1.4 channel was delivered to, and retrieved from, the PM at the perimeter of Kv2.1 clusters (51). To determine whether cER enriched PM domains would still be the preferred site for Kv1.4 delivery and retrieval in the absence of Kv2.1 expression we used a single molecule, Qdot-based assay to track both exo- and endocytosis of recycling Kv1.4 channels. HEK cells expressing surface biotinylated CFP-Kv1.4-loopBAD and DsRed2-ER were briefly incubated with a low concentration of Qdots to label a small fraction of the surface Kv1.4 channels.

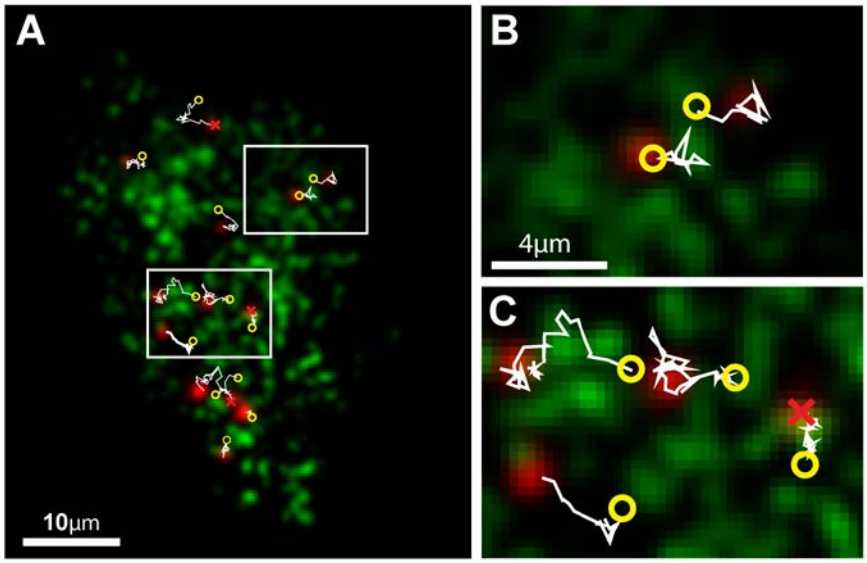

Figure 29. Exo and endocytosis of Kv1.4. HEK cells expressing biotinylated Kv1.4 were labeled at low efficiency with 605Qdots and then imaged via TIRF microscopy to observe delivery and retrieval at the cell surface. (A) The location where the Qdot first appears is marked by the yellow circle and disappearance with the red X. Note that the appearing Qdot in the top center of panel A most likely diffused into the TIR field from the side of the cell since it was first detected at the edge of the cell. Trajectories from 292 frames are shown, and the length of the track is representative of the amount of time each Qdot was present during the movie. (B&C) Enlargements of the top and bottom boxed regions in panel A, respectively. Kv1.4 exocytosis preferred plasma membrane sites within 0.15 μm of the cER perimeter with 78± 3% (n=176 events, 4 cells) of Qdots spontaneously appearing in these regions. Kv1.4 endocytosis also preferred these regions with 77± 3% (n=176, 4 cells) of Qdots spontaneously disappearing adjacent to the cER. In these cells the cER perimeter (0.15 μm) accounted for only 21±4% of the cell footprint.

The cells were then imaged via TIRF and the appearance and disappearance of Qdots were analyzed with custom tracking algorithms (134). As previously described (51), the spontaneous disappearance of a Qdot for >60 s represents endocytosis as non-fluorescent Qdot states are unlikely to occur for this amount of time. Similarly, the sudden appearance of a Qdot in the TIR field >60 s after the beginning of imaging represents membrane delivery of a previously internalized surface channel. Figure 29 illustrates the Kv1.4 insertion and retrieval sites mapped over 2 min and 42 s sec. The location where each Qdot first appears is marked by a yellow circle and disappearance with a red X. Trajectories from 292 frames are shown, and the length of the track is representative of the amount of time each Qdot was present during the movie. Almost 80% of the Kv1.4 exocytosis (78±3%, n=176 events, 4 cells) occurred at plasma membrane sites within 0.15 μm of the cER perimeter. Nearly the same percentage of delivery events occurred at the perimeter of Kv2.1 clusters (51). Kv1.4 endocytosis also preferred these regions with 77±3% (n=176, 4 cells) of Qdots spontaneously disappearing adjacent to the cER. In these cells the cER perimeter (0.15 μm) accounted for only 21±4% of the cell footprint.

Thin-section electron microscopy analysis of cER in HEK cells. The cER as viewed with TIRF-based light microscopy appeared as both tubular and punctate structures. At an ultra structural level we expected to see a similar pattern of ER running underneath plasma membrane. Our data also suggested that we would find both vesicular and endosomal structures near the cER. We analyzed the cER in glutaraldehyde-fixed HEK cells using thin-section electron microscopy. In order to observe EM thin sections that most closely relate to our TIRF images, we began sectioning at the basal surface of the cells. Figure 30A gives us a TIRF-like snapshot of the basal membrane of the cell.

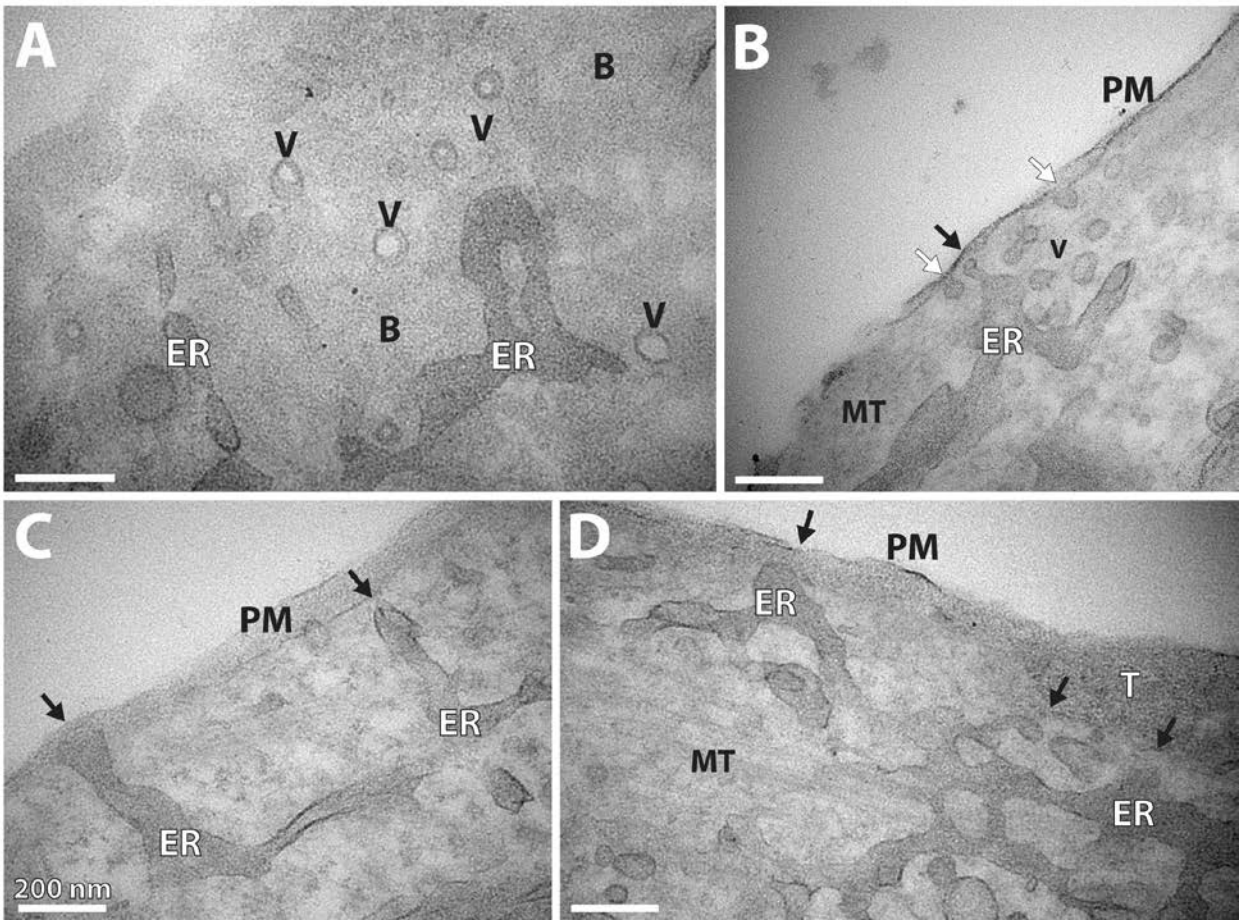

Figure 30. Thin-section electron microscopy of cER in HEK cells. (A) EM micrograph of an ultrathin section (<100nm) through the basal membrane (B) of the cell. Within 200nm of the ER (ER) on the right there are 4 vesicular structures (V) which are likely docked at the PM. (B) EM micrograph illustrates ER making a small contact point (black arrow) with the PM (PM) in this section. Endocytic structures (white arrows) and possible vesicular structures are within 200nm of the ER-PM contact point. (C) This EM micrograph illustrates a typical region of cortical ER. Here, the ER runs parallel to the PM but at a distance >100nm from the PM. The ER turns to make perpendicular contacts with PM (black arrows). (D) This micrograph illustrates a similar situation as in C, with the ER running parallel to and making contacts with the PM. Microtubules (MT) run underneath the cortical ER at a distance far out of the TIRF field. All micrograph were acquired at 100,000x magnification. All scale bars are 200nm. (B=basal membrane, V=vesicular structure, ER=endoplasmic reticulum, PM=cross sectioned plasma membrane, MT=microtubules, T=transverse sectioned plasma membrane, black arrows=ER-PM contacts, white arrows=endocytic structures).

Here we see ER which is likely within 100nm of the plasma membrane since it occupies the same plane as the sectioned basal membrane (B). Within 200nm of the ER perimeter we see 4 vesicular structures (V) which seem to be docked at the PM. These structures appear less dense in the center, suggesting they may be continuous with the extracellular space and thus in the process of exo- or endoxytosis. Figure 30B is a deeper section in which the ER makes a very small point of contact (black arrow) with the plasma membrane. Here we observed both endocytic structures (white arrows) and vesicular structures in the immediate vicinity of the ER. The EM micrograph in Figure 30C illustrates a typical region of cortical ER. Here, the ER runs parallel to the plasma membrane at a distance >100nm away, likely not within the field of view that can be imaged by TIRF microscopy. The ER turns outwards to make occasional perpendicular contacts (black arrows) with PM. Figure 30D illustrates a similar situation, with the ER running parallel to the transversely sectioned plasma membrane (T) and occasionally making close contact with the PM. Here, some of the tubular ER running parallel to the plasma membrane is close enough (<100nm) to be observed in the TIR imaging plane. This is consistent with the often tubular appearance of the cER in TIRF. Microtubules run underneath the ER at a distance far beyond TIR imaging plane. Distinct ER/PM junctions like those found in sub-surface cisterns in neurons (63) or induced by STIM1 in response to ER Ca^{2+} depletion (105) were rarely observed in our HEK cells.

Our ultrastructural study of cortical ER in HEK cells shows that some of the cER we observe in TIRF indeed forms close physical contact with the plasma membrane. To study these apparent connections in greater detail with TIRF microscopy we expressed YFP-STIM1, which is a well characterized marker for ER-PM contacts, along with DsRed2-ER. YFP-STIM1 is distributed throughout the ER under normal resting conditions, but displays a remarkable translocation to sites of contact between the ER and PM under conditions of ER Ca^{2+} depletion (146).

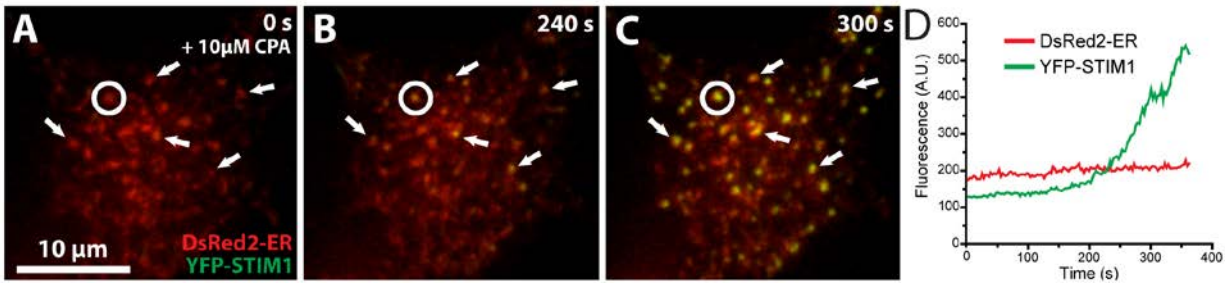

Figure 31. Translocation of STIM1 to pre-existing cER domains following ER Ca^{2+} depletion. (A-C) TIRF images of a HEK cell expressing DsRed2-ER and YFP-STIM1 at the time of cyclopiazonic acid (CPA, 10µM) addition (A), 240 seconds after CPA addition (B) and 300 seconds after CPA addition (C). White arrows point to cER domains which remain stable throughout the experiment and accumulate YFP-STIM1 following CPA addition. (D) Graph of DsRed2-ER and YFP-STIM fluorescence from the cER domain within the white circular ROI during the first 360 seconds following CPA addition. Note the dramatic increase in YFP-STIM1 fluorescence compared to the relatively stable DsRed2-ER fluorescence.

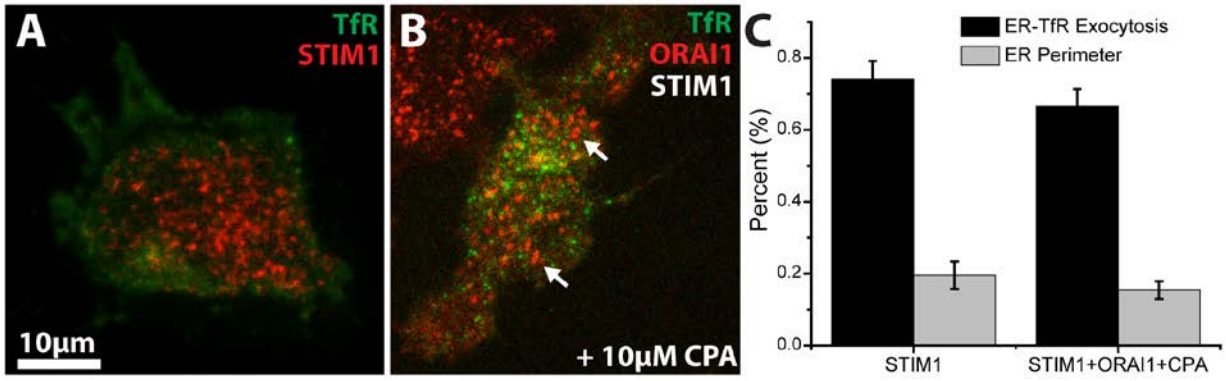

Figure 32. TfR-SEP exocytosis in relation to cER containing STIM1 or STIM1 and Orai1. (A) HEK cells expressing CFP-STIM1 (pseudo-colored red) and TfR-SEP (green) imaged via TIRF microscopy. In the absence of ER Ca^{2+} depletion, STIM1 imaged in TIRF serves as a cER marker. (B) HEK cells expressing STIM1 (not shown), CFP-Orai1 (red) and TfR-SEP (green) following ER Ca^{2+} depletion with 10µM CPA. Orai1 expression is apparent from the diffuse membrane localized fluorescence (yellow arrow) and STIM1 activation is apparent from the fluorescent Orai1 puncta (white arrows). (C) Bar graph illustrating the percentage of TfR-SEP exocytosis events which occur within 2 pixels of the cER (black bar) and the percentage of the cell footprint that is occupied by the cER perimeter (grey bar) based on STIM1 or STIM1-Orai1 fluorescence.

We observed that YFP-STIM1 translocated to a subset of discrete cER enriched domains, consistent with our ultrastructural analysis (Figure 31). To determine if ER-PM contacts are involved in the localization of trafficking events near the cER perimeter, we repeated our TfR exocytosis study using Orai1 as a marker for ER-PM contacts. Orai1 is a PM Ca^{2+} channel which is physically gated by interactions with activated STIM1 in the ER. Orai1 typically has a diffuse PM localization and only localizes to ER-PM contacts following physical interaction with STIM1 (Figure 32B). When we used Orai1 puncta as a marker of ER-PM contacts we observed 67 ± 5% (n=5, 150 events) of TfR exocytic events occurred within 2 pixels of the Orai1 puncta while the puncta only accounted for only 15 ± 3% of the cell footprint (Figure 32C). These data indicate that a subset of the cER localized TfR exocytosis occurs in the vicinity of "classic" ER-PM contacts.

Discussion

The previously described function for cER largely involves regulation of Ca^{2+} homeostasis. In the plasma membrane, voltage-gated Ca^{2+}, Orai and Trp channels are localized to these microdomains along with ER proteins involved in Ca^{2+} regulation such as the ryanodine receptor, IP3 receptor and STIM1 (66). The data presented above indicate that an additional role for these membrane domains is to serve as localized trafficking hubs for endo/exocytosis. Not only are the relatively abundant transferrin receptors trafficked at these locations but also sparse membrane proteins such as the Kv1.4 K^+ channel. In addition, this localized trafficking extends beyond recycling membrane proteins since nascent VSVG traveling to the surface for the first time is delivered here. While the work presented here is derived from HEK cells the data are likely of general relevance to other cell types, especially neurons. HEK cells express a large number of neuronal genes and are actually of neuronal origin despite the fact that they were derived from a kidney homogenate (73). Since HEK cells express almost no voltage-gated ion channels they are

best viewed as immature neurons. Furthermore, a recent publication describes a strikingly similar relationship between the cortical ER and endocytic traffic in yeast, where the cortical ER extends across the majority of the PM (147).

Advantages of localized trafficking hubs. Research over the past decade has increasingly demonstrated that numerous plasma membrane functions are highly organized, often due to the existence of specific sub-membrane scaffolding structures. The use of stable, reusable sites for endo/exocytosis outside of the neuronal synapse is now becoming a commonly accepted idea (122, 125-129). Membrane protein trafficking hubs as described here and in our previous work, have obvious advantages. Specialized domains are more energy efficient than constantly reassembling trafficking machinery and trafficking vesicles can be delivered along relatively static microtubules. Such localization also provides for enhanced regulation since signaling molecules can be stably localized at the trafficking sites.

Why cER enriched PM domains as a trafficking hub? Using this cellular organelle as a trafficking hub has two obvious advantages. First, many trafficking vesicles delivering cargo to the cell surface move via kinesin motors along microtubule tracks. The ER network is rich in microtubles, with microtubule dynamics responsible for defining cytoplasmic ER morphology (148-150). Thus, the ER surface itself may serve as a template for microtubule orientation towards the cell surface. Second, since the cER plays a major role in Ca^{2+} homeostasis, trafficking here could place endo/exocytosis under direct control of Ca^{2+} within this microdomain. In support of this idea, ER-derived Ca^{2+} regulates exocytosis in astrocytes (151). While this study specifically examined glutamate release from these cells, this effect of localized Ca^{2+} on exocytosis may have general relevance.

Relationship between the cytoskeleton, cortical ER and exocytosis. An obvious concern is that cER reaches the plasma membrane in regions where cortical actin is sparse and these just

happen to be areas where exocytic/endocytic vesicles can get access to the PM (152). We have addressed this possibility in two ways. First, as illustrated in Figure 33, we disrupted f-actin with latrunculin A (100nM, 30 minutes) and observed the ER present at the cell surface decreasing to 77±12% of control (n=12). If the ER, and trafficking vesicles, reach the surface just where cortical actin is sparse then actin depolymerization should have increased the amount of ER visible within the TIR-field.

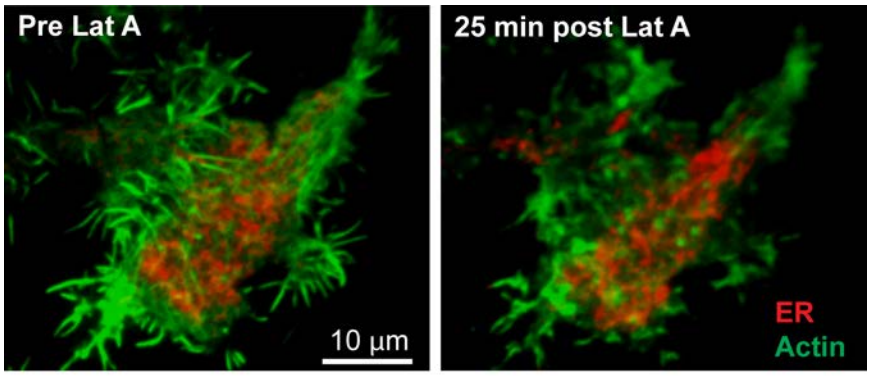

Figure 33. Actin depolymerization does not enhance cortical ER. HEK cells expressing GFP-CB5 to mark the ER (pseudo-colored red) and RubyRed-Lifeact to bind f-actin (pseudo-colored green) were imaged at 1 Hz in TIRF following the addition of 100 nM latrunculin A. By 25 min the cortical ER present as defined by the DsRed2-ER fluorescence in the TIR-field decrease to 77±12% (mean± sd) of control (n=12). Similar results were obtained with 200 nM Swinholide A.

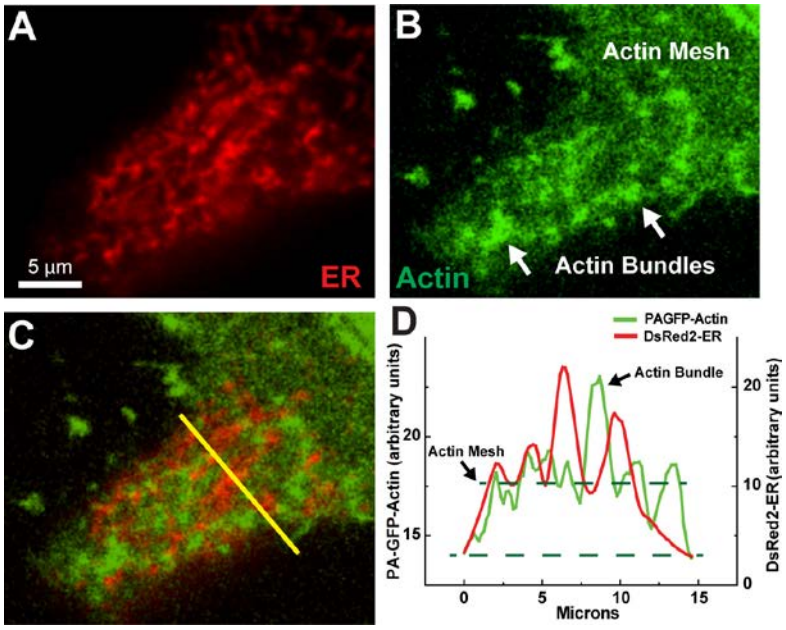

Figure 34. Relationship between actin and ER at the cell surface. HEK cells expressing DsRed2-ER and photoactivatable GFP-actin (PA-GFP-actin) were imaged in TIRF. (A and B) DsRed2-ER and GFP fluorescence 22 sec post photo-activation via 405 nm illumination in TIRF. At this time PA-GFP-actin monomers have diffused out of the TIR-field leaving behind only f-actin. (C) Image overlay. Note that the f-actin bundles and ER occupy distinct areas. (D) Profile intensity of the line shown in C. A one µm line width was used. Here the ER distribution is unrelated to the fine cortical actin distribution (top dashed line) while the ER appears to avoid areas containing actin bundles. The background GFP fluorescence is indicated by the lower dashed line.

Actin depolymerization caused a decrease in the percentage of TfR exocytosis events occurring at the ER perimeter, from 82±12% (mean ±sd, n=560, from 21 cells) under control conditions to 76± 9% (mean ±sd, n=97, from 4 cells). However, it is difficult to conclude that f-actin is involved in coupling exocytosis to the ER perimeter since this change could be due to non-specific effects derived from cell shape changes following loss of the cytoskeleton. In our second attempt to relate cortical ER and actin we imaged photoactivatable GFP-actin and DsRed2-ER in TIRF and found that while large actin bundles appear to direct the cER morphology, fluctuations in the fluorescent intensity of the finer cortical actin mesh, which cannot be resolved by light microscopy, show no apparent relation to ER positioning (Figure 34). Additional research is required to determine the role, if any, of actin in the localization of exocytosis near the cortical ER.

On the other hand, microtubules play a role in both the organization of the ER and vesicular transport. This led us to investigate whether tubulin disruption with colchicine alters the cortical ER or the location of TfR exocytosis. While the cytoplasmic ER is disrupted following microtubule depolymerization with colchicine (2.5 μM, 20 minutes, n=5) as expected (data not shown), the ER in the TIR field is unaffected as illustrated in Figure 35, suggesting tubulin does not play a tethering role for the cortical ER. After 40 min in colchicine the percentage of TfR exocytosis occurring within 0.3 μm of the cER perimeter is reduced to 47±18% (n=9) compared to 82±5% under control conditions, with the cER perimeter representing 24±7% of the cell area. Whether this is meaningful or just an indication of poor cell health, as suggested by the morphology changes, is unclear. Unfortunately, we have found no interventions that selectively remove the cortical ER, for this would be a convincing means of linking this structure to exocytosis.

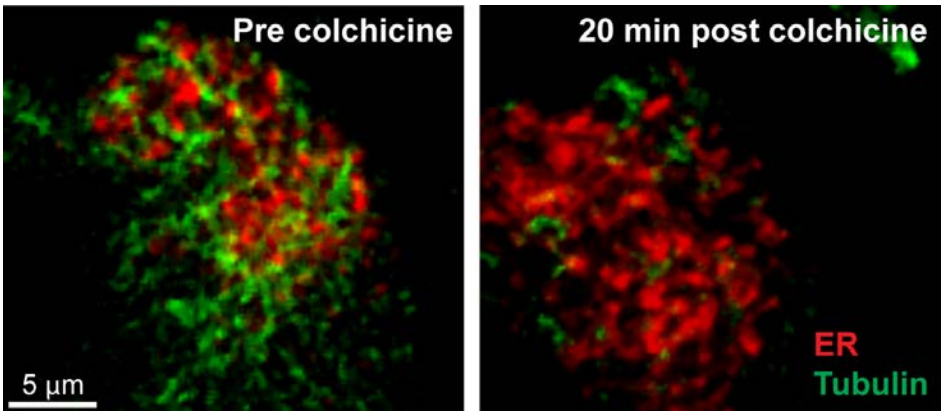

Figure 35. Tubulin depolymerization does not alter the cortical ER. HEK cells expressing GFP-CB5 to mark the ER (pseudo-colored red) and mCherry-tubulin (pseudo-colored green) were imaged in TIRF before and 20 min after the addition of 2.5µM colchicine. After colchicine addition the cER area visible in the TIR-illumination field was 100.5±18.7% (mean±sd) of that prior to treatment in the 5 cells examined. The standard deviation reflects the ER dynamics seen under control conditions.

Conclusion. We have discovered a new cellular microdomain that directs membrane protein trafficking to and from the cell surface. Exocytosis of both recycling and nascent membrane proteins preferentially occurs adjacent to sites of close apposition between the cER and the PM. Furthermore, endocytic components such as clathrin light chain and TfR cargo preferentially accumulate adjacent to cER enriched PM domains. This spatial arrangement suggests that factors important for the localization and regulation of exo/endocytic machinery are enriched in the vicinity of the cER.

Chapter 5: Summary and Perspective

Kv2.1 channel function in HEK cells is in many ways identical to the Kv2.1 current in neurons, both in kinetics and in magnitude (27). In HEK cells, Kv2.1 channels exist in one of two functional states, either conducting or non-conducting. Conducting channels can be activated by depolarization of the membrane potential allowing them to pass K+ ions. Non-conducting channels sense membrane potential through S4 movement and either cannot be activated by S4 movement, or switch to an open state with a minimal K+ conductance (69). Kv2.1 channels also exist in one of two localization states, either clustered or non-clustered. Channels localized to large dense clusters tend to be fully non-conducting, while channels diffusely localized at the PM tend to be largely conducting. Despite this tendency towards localization-dependent activity, the non-conducting state is experienced by both clustered and non-clustered channels. The probability of a non-clustered channel being in the non-conducting state goes up as the density of non-clustered channels increases (97). This argues that the channel modification which results in cluster localization is not the same modification which leads to non-conductance. Instead, a possible explanation is that the non-conducting state is regulated by the local density of the channel. Within clusters, the density is typically great enough for 99% of the channels to be non-conducting. Outside the clusters, channels become increasingly non-conducting as the density of channels increases. Even though phosphorylation controls both clustering and the midpoint of voltage dependent activation of Kv2.1 (49), the modification which makes the channel non-conducting is unlikely to be phosphorylation, as complete dephosphorylation with alkaline phosphatase does not increase current density (69). Instead, to achieve density dependent regulation, channels could be competing for a limited resource, in the cytoplasm or the membrane.

The presence of so many non-conducting Kv2.1 channels in neurons argues that those channels serve some other crucial function, which likely revolves around the largely non-conducting

clusters (97). One function is to direct vesicular traffic to the perimeter of the Kv2.1 clusters. Another function of the clusters is to localize exo- and endocytic machinery at the perimeter of the cluster (51). Thus the Kv2.1 clusters marks hotspots for trafficking and potentially secretion at the neuronal soma. This remarkable effect is a result of the co-localization between the Kv2.1 clusters and underlying cER (94). In the absence of Kv2.1 clusters, the cER alone marks hotspots of vesicular traffic and endocytosis. This is true for a variety of cargo proteins, beyond Kv channels, and is potentially a generalizable phenomenon. Thus the cER directs vesicular traffic at the cell cortex, which in turn regulates the localization of membrane proteins on the PM. Meanwhile, Kv2.1 remodels the cER into close junctions between the ER and PM. The existence of Kv2.1 clusters are a result of the channel binding to an unknown, mobile ER membrane factor. Thus the clustering of Kv2.1 alters the shape and position of the cER which in turn localizes the trafficking landscape around the cluster. Kv2.1 clustering stabilizes the underlying cER and potentially facilitates alterations to the lipid composition of the PM by bringing ER enzymes involved in lipid metabolism into close proximity to the PM. Thus the clustering of Kv2.1 channels actually creates a new PM domain, which likely contains a unique combination of proteins and lipids. This specialized PM domain is dismantled in response to stroke-like insults such as glutamate excitotoxicity, raising the question of whether this is a neurotoxic or neuroprotective event.

ER/PM tethering proteins. ER/PM junctions are probably best studied in yeast, where 30-40% of the PM has ER associated (64). Here, the junctions have clear roles in lipid metabolism and synthesis (58, 153, 154), and affect the general viability of the cell (155). In order to meaningfully disrupt junctions in yeast, six genes must be deleted, indicating that there is functional overlap and compensation between tethering proteins (64). A similar situation is likely to exist in mammals. It is notable that all of the ER/PM tethers previously described in yeast and mammals have some distinct commonalities. Without exception, the ER/PM tethers are anchored

in the ER membrane and bind to phospholipid head groups on the inner leaflet of the PM, either directly, or indirectly through another protein (61). Thus, Kv2.1 is the first ER/PM tether that is anchored in the PM. If Kv2.1 interacts with a protein that is anchored in the ER membrane, that would be the first descripting of ER/PM tethering involving two membrane anchored proteins. Likewise, if Kv2.1 binds to an ER lipid, it would be a unique protein-lipid interaction, since the ER is devoid of the phosphatidylinositol phosphate species for which there are well described binding domains in proteins (58). Understanding the full mechanism of Kv2.1 clustering and ER remodeling is likely to uncover other biological firsts.

Future Directions. It is likely that the Kv2.1 clusters serve other functions than the ones demonstrated in this work. There is currently no direct evidence of localized lipid metabolism or enhance signal transduction occurring at the Kv2.1 clusters, but there is good evidence of these reactions taking place at ER/PM junctions in general (92, 153, 154). Although there is currently no information about the effect of Kv2.1 clustering on neuronal excitability, it is likely that the ER/PM junctions formed by Kv2.1 participate in Ca^{2+} signaling, as they do in all other cell types (66). Given the role of Kv2.1 in localizing membrane protein trafficking to the perimeter of the Kv2.1-induced ER/PM junctions (51) (94), a possible role for the clusters is to bring lipid and Ca^{2+} signaling in close proximity to the trafficking hub, potentially allowing for Ca^{2+} and lipid regulation of vesicular release and protein internalization. Finding the molecule in the ER membrane that Kv2.1 interacts with will shed more light on the functions of the neuronal ER/PM junctions that Kv2.1 helps to create. Indeed, the functional role that ER/PM junctions play in neurons is completely unknown and is an important avenue of future research.

References

1. Alberts B*, et al.* (2008) *Molecular Biology of the Cell* (Garland Science) 4th Ed.

2. Singer SJ & Nicolson GL (1972) The fluid mosaic model of the structure of cell membranes. *Science* 175(4023):720-731.

3. Engelman DM (2005) Membranes are more mosaic than fluid. *Nature* 438(7068):578-580.

4. Hille B (2001) *Ion Channels of Excitable Membranes* (Sinauer Associates) 3rd Ed.

5. Catterall WA, Chandy KG, & Giutman GA eds (2002) *The IUPHAR Compendium of Voltage-gated Ion Channels* (IUPHAT Media, Leeds, UK).

6. Kihira Y, Hermanstyne TO, & Misonou H (2010) Formation of heteromeric Kv2 channels in mammalian brain neurons. *The Journal of biological chemistry* 285(20):15048-15055.

7. Guan D, Horton LR, Armstrong WE, & Foehring RC (2011) Postnatal development of A-type and Kv1- and Kv2-mediated potassium channel currents in neocortical pyramidal neurons. *Journal of neurophysiology* 105(6):2976-2988.

8. Liu PW & Bean BP (2014) Kv2 channel regulation of action potential repolarization and firing patterns in superior cervical ganglion neurons and hippocampal CA1 pyramidal neurons. *The Journal of neuroscience : the official journal of the Society for Neuroscience* 34(14):4991-5002.

9. Malin SA & Nerbonne JM (2002) Delayed rectifier K+ currents, IK, are encoded by Kv2 alpha-subunits and regulate tonic firing in mammalian sympathetic neurons. *The Journal of neuroscience : the official journal of the Society for Neuroscience* 22(23):10094-10105.

10. Murakoshi H & Trimmer JS (1999) Identification of the Kv2.1 K+ channel as a major component of the delayed rectifier K+ current in rat hippocampal neurons. *The Journal of neuroscience : the official journal of the Society for Neuroscience* 19(5):1728-1735.

11. Du J, Haak LL, Phillips-Tansey E, Russell JT, & McBain CJ (2000) Frequency-dependent regulation of rat hippocampal somato-dendritic excitability by the K+ channel subunit Kv2.1. *The Journal of physiology* 522 Pt 1:19-31.

12. Scannevin RH, Murakoshi H, Rhodes KJ, & Trimmer JS (1996) Identification of a cytoplasmic domain important in the polarized expression and clustering of the Kv2.1 K+ channel. *The Journal of cell biology* 135(6 Pt 1):1619-1632.

13. Sarmiere PD, Weigle CM, & Tamkun MM (2008) The Kv2.1 K+ channel targets to the axon initial segment of hippocampal and cortical neurons in culture and in situ. *BMC neuroscience* 9:112.

14. Jensen CS*, et al.* (2014) Specific sorting and post-Golgi trafficking of dendritic potassium channels in living neurons. *The Journal of biological chemistry* 289(15):10566-10581.

15. Nakada C*, et al.* (2003) Accumulation of anchored proteins forms membrane diffusion barriers during neuronal polarization. *Nature cell biology* 5(7):626-632.

16. Tamkun MM, O'Connell K M, & Rolig AS (2007) A cytoskeletal-based perimeter fence selectively corrals a sub-population of cell surface Kv2.1 channels. *Journal of cell science* 120(Pt 14):2413-2423.

17. O'Connell KM, Rolig AS, Whitesell JD, & Tamkun MM (2006) Kv2.1 potassium channels are retained within dynamic cell surface microdomains that are defined by a perimeter fence. *The Journal of neuroscience : the official journal of the Society for Neuroscience* 26(38):9609-9618.

18. Du J, Tao-Cheng JH, Zerfas P, & McBain CJ (1998) The K+ channel, Kv2.1, is apposed to astrocytic processes and is associated with inhibitory postsynaptic membranes in hippocampal and cortical principal neurons and inhibitory interneurons. *Neuroscience* 84(1):37-48.

19. Mandikian D*, et al.* (2014) Cell type-specific spatial and functional coupling between mammalian brain Kv2.1 K channels and ryanodine receptors. *The Journal of comparative neurology*.

20. King AN, Manning CF, & Trimmer JS (2014) A unique ion channel clustering domain on the axon initial segment of mammalian neurons. *The Journal of comparative neurology* 522(11):2594-2608.

21. Muennich EAL & Fyffe REW (2004) Focal aggregation of voltage-gated, Kv2.1 subunit-containing, potassium channels at synaptic sites in rat spinal motoneurones. *J Physiol (Lond)* 554(Pt 3):673-685.

22. Shi G, Kleinklaus AK, Marrion NV, & Trimmer JS (1994) Properties of Kv2.1 K+ channels expressed in transfected mammalian cells. *The Journal of biological chemistry* 269(37):23204-23211.

23. Kerschensteiner D, Soto F, & Stocker M (2005) Fluorescence measurements reveal stoichiometry of K+ channels formed by modulatory and delayed rectifier alpha-subunits. *Proceedings of the National Academy of Sciences of the United States of America* 102(17):6160-6165.

24. Mohapatra DP, Siino DF, & Trimmer JS (2008) Interdomain cytoplasmic interactions govern the intracellular trafficking, gating, and modulation of the Kv2.1 channel. *The Journal of neuroscience : the official journal of the Society for Neuroscience* 28(19):4982-4994.

25. Singer-Lahat D*, et al.* (2007) K+ channel facilitation of exocytosis by dynamic interaction with syntaxin. *The Journal of neuroscience : the official journal of the Society for Neuroscience* 27(7):1651-1658.

26. Lim ST, Antonucci DE, Scannevin RH, & Trimmer JS (2000) A novel targeting signal for proximal clustering of the Kv2.1 K+ channel in hippocampal neurons. *Neuron* 25(2):385-397.

27. Mohapatra DP & Trimmer JS (2006) The Kv2.1 C terminus can autonomously transfer Kv2.1-like phosphorylation-dependent localization, voltage-dependent gating, and muscarinic modulation to diverse Kv channels. *The Journal of neuroscience : the official journal of the Society for Neuroscience* 26(2):685-695.

28. Park KS, Mohapatra DP, Misonou H, & Trimmer JS (2006) Graded regulation of the Kv2.1 potassium channel by variable phosphorylation. *Science* 313(5789):976-979.

29. Misonou H, Mohapatra DP, Menegola M, & Trimmer JS (2005) Calcium- and metabolic state-dependent modulation of the voltage-dependent Kv2.1 channel regulates neuronal excitability in response to ischemia. *The Journal of neuroscience : the official journal of the Society for Neuroscience* 25(48):11184-11193.

30. Misonou H, Thompson SM, & Cai X (2008) Dynamic regulation of the Kv2.1 voltage-gated potassium channel during brain ischemia through neuroglial interaction. *The Journal of neuroscience : the official journal of the Society for Neuroscience* 28(34):8529-8538.

31. Redman PT*, et al.* (2007) Apoptotic surge of potassium currents is mediated by p38 phosphorylation of Kv2.1. *Proceedings of the National Academy of Sciences of the United States of America* 104(9):3568-3573.

32. Plant LD, Dowdell EJ, Dementieva IS, Marks JD, & Goldstein SA (2011) SUMO modification of cell surface Kv2.1 potassium channels regulates the activity of rat hippocampal neurons. *The Journal of general physiology* 137(5):441-454.

33. Consiglio JF & Korn SJ (2004) Influence of permeant ions on voltage sensor function in the Kv2.1 potassium channel. *The Journal of general physiology* 123(4):387-400.

34. Immke D, Wood M, Kiss L, & Korn SJ (1999) Potassium-dependent changes in the conformation of the Kv2.1 potassium channel pore. *The Journal of general physiology* 113(6):819-836.

35. Cotella D*, et al.* (2012) Toxic role of K+ channel oxidation in mammalian brain. *The Journal of neuroscience : the official journal of the Society for Neuroscience* 32(12):4133-4144.

36. Dallas ML*, et al.* (2011) Carbon monoxide protects against oxidant-induced apoptosis via inhibition of Kv2.1. *FASEB journal : official publication of the Federation of American Societies for Experimental Biology* 25(5):1519-1530.

37. Hulme JT, Coppock EA, Felipe A, Martens JR, & Tamkun MM (1999) Oxygen sensitivity of cloned voltage-gated K(+) channels expressed in the pulmonary vasculature. *Circulation research* 85(6):489-497.

38. Baranauskas G, Tkatch T, & Surmeier DJ (1999) Delayed rectifier currents in rat globus pallidus neurons are attributable to Kv2.1 and Kv3.1/3.2 K(+) channels. *The Journal of neuroscience : the official journal of the Society for Neuroscience* 19(15):6394-6404.

39. Baver SB*, et al.* (2014) Leptin modulates the intrinsic excitability of AgRP/NPY neurons in the arcuate nucleus of the hypothalamus. *The Journal of neuroscience : the official journal of the Society for Neuroscience* 34(16):5486-5496.

40. Dufour MA, Woodhouse A, & Goaillard JM (2014) Somatodendritic ion channel expression in substantia nigra pars compacta dopaminergic neurons across postnatal development. *Journal of neuroscience research* 92(8):981-999.

41. Amberg GC & Santana LF (2006) Kv2 channels oppose myogenic constriction of rat cerebral arteries. *American journal of physiology. Cell physiology* 291(2):C348-356.

42. MacDonald PE*, et al.* (2002) Synaptosome-associated protein of 25 kilodaltons modulates Kv2.1 voltage-dependent K(+) channels in neuroendocrine islet beta-cells through an interaction with the channel N terminus. *Molecular endocrinology* 16(11):2452-2461.

43. Mulholland PJ*, et al.* (2008) Glutamate transporters regulate extrasynaptic NMDA receptor modulation of Kv2.1 potassium channels. *The Journal of neuroscience : the official journal of the Society for Neuroscience* 28(35):8801-8809.

44. Pal S, Hartnett KA, Nerbonne JM, Levitan ES, & Aizenman E (2003) Mediation of neuronal apoptosis by Kv2.1-encoded potassium channels. *The Journal of neuroscience : the official journal of the Society for Neuroscience* 23(12):4798-4802.

45. McCord MC*, et al.* (2014) Syntaxin-binding domain of Kv2.1 is essential for the expression of apoptotic K+ currents. *The Journal of physiology*.

46. Speca DJ*, et al.* (2014) Deletion of the Kv2.1 delayed rectifier potassium channel leads to neuronal and behavioral hyperexcitability. *Genes, brain, and behavior* 13(4):394-408.

47. Feinshreiber L*, et al.* (2010) Non-conducting function of the Kv2.1 channel enables it to recruit vesicles for release in neuroendocrine and nerve cells. *Journal of cell science* 123(Pt 11):1940-1947.

48. Surmeier DJ & Foehring R (2004) A mechanism for homeostatic plasticity. *Nature neuroscience* 7(7):691-692.

49. Misonou H*, et al.* (2004) Regulation of ion channel localization and phosphorylation by neuronal activity. *Nature neuroscience* 7(7):711-718.

50. Shi G & Trimmer JS (1999) Differential asparagine-linked glycosylation of voltage-gated K+ channels in mammalian brain and in transfected cells. *The Journal of membrane biology* 168(3):265-273.

51. Deutsch E*, et al.* (2012) Kv2.1 cell surface clusters are insertion platforms for ion channel delivery to the plasma membrane. *Molecular biology of the cell* 23(15):2917-2929.

52. Manganas LN & Trimmer JS (2000) Subunit composition determines Kv1 potassium channel surface expression. *The Journal of biological chemistry* 275(38):29685-29693.

53. Weigel AV, Tamkun MM, & Krapf D (2013) Quantifying the dynamic interactions between a clathrin-coated pit and cargo molecules. *Proceedings of the National Academy of Sciences of the United States of America* 110(48):E4591-4600.

54. English AR, Zurek N, & Voeltz GK (2009) Peripheral ER structure and function. *Current opinion in cell biology* 21(4):596-602.

55. Porter KR & Palade GE (1957) Studies on the endoplasmic reticulum. III. Its form and distribution in striated muscle cells. *The Journal of biophysical and biochemical cytology* 3(2):269-300.

56. Lavoie C & Paiement J (2008) Topology of molecular machines of the endoplasmic reticulum: a compilation of proteomics and cytological data. *Histochemistry and cell biology* 129(2):117-128.

57. Presley JF*, et al.* (1997) ER-to-Golgi transport visualized in living cells. *Nature* 389(6646):81-85.

58. Fagone P & Jackowski S (2009) Membrane phospholipid synthesis and endoplasmic reticulum function. *Journal of lipid research* 50 Suppl:S311-316.

59. Lioudyno M*, et al.* (2004) A "synaptoplasmic cistern" mediates rapid inhibition of cochlear hair cells. *The Journal of neuroscience : the official journal of the Society for Neuroscience* 24(49):11160-11164.

60. Helle SC*, et al.* (2013) Organization and function of membrane contact sites. *Biochimica et biophysica acta* 1833(11):2526-2541.

61. Prinz WA (2014) Bridging the gap: Membrane contact sites in signaling, metabolism, and organelle dynamics. *The Journal of cell biology* 205(6):759-769.

62. Franzini-Armstrong C & Jorgensen AO (1994) Structure and development of E-C coupling units in skeletal muscle. *Annual review of physiology* 56:509-534.

63. Rosenbluth J (1962) Subsurface cisterns and their relationship to the neuronal plasma membrane. *The Journal of cell biology* 13:405-421.

64. Stefan CJ, Manford AG, & Emr SD (2013) ER-PM connections: sites of information transfer and inter-organelle communication. *Current opinion in cell biology* 25(4):434-442.

65. Roos J*, et al.* (2005) STIM1, an essential and conserved component of store-operated Ca2+ channel function. *The Journal of cell biology* 169(3):435-445.

66. Carrasco S & Meyer T (2011) STIM proteins and the endoplasmic reticulum-plasma membrane junctions. *Annual review of biochemistry* 80:973-1000.

67. Feske S*, et al.* (2006) A mutation in Orai1 causes immune deficiency by abrogating CRAC channel function. *Nature* 441(7090):179-185.

68. Giordano F*, et al.* (2013) PI(4,5)P(2)-dependent and Ca(2+)-regulated ER-PM interactions mediated by the extended synaptotagmins. *Cell* 153(7):1494-1509.

69. O'Connell KM, Loftus R, & Tamkun MM (2010) Localization-dependent activity of the Kv2.1 delayed-rectifier K+ channel. *Proceedings of the National Academy of Sciences of the United States of America* 107(27):12351-12356.

70. Guan D, Tkatch T, Surmeier DJ, Armstrong WE, & Foehring RC (2007) Kv2 subunits underlie slowly inactivating potassium current in rat neocortical pyramidal neurons. *The Journal of physiology* 581(Pt 3):941-960.

71. O'Connell KM & Tamkun MM (2005) Targeting of voltage-gated potassium channel isoforms to distinct cell surface microdomains. *Journal of cell science* 118(Pt 10):2155-2166.

72. Kole MH*, et al.* (2008) Action potential generation requires a high sodium channel density in the axon initial segment. *Nature neuroscience* 11(2):178-186.

73. Shaw G, Morse S, Ararat M, & Graham FL (2002) Preferential transformation of human neuronal cells by human adenoviruses and the origin of HEK 293 cells. *FASEB journal : official publication of the Federation of American Societies for Experimental Biology* 16(8):869-871.

74. Tseng-Crank J, Yao JA, Berman MF, & Tseng GN (1993) Functional role of the NH2-terminal cytoplasmic domain of a mammalian A-type K channel. *The Journal of general physiology* 102(6):1057-1083.

75. Ulbrich MH & Isacoff EY (2007) Subunit counting in membrane-bound proteins. *Nature methods* 4(4):319-321.

76. Sugiyama Y, Kawabata I, Sobue K, & Okabe S (2005) Determination of absolute protein numbers in single synapses by a GFP-based calibration technique. *Nature methods* 2(9):677-684.

77. Gentet LJ, Stuart GJ, & Clements JD (2000) Direct measurement of specific membrane capacitance in neurons. *Biophysical journal* 79(1):314-320.

78. Yang J, Thio LL, Clifford DB, & Zorumski CF (1993) Electrophysiological properties of identified postnatal rat hippocampal pyramidal neurons in primary culture. *Brain research. Developmental brain research* 71(1):19-26.

79. Leake MC*, et al.* (2006) Stoichiometry and turnover in single, functioning membrane protein complexes. *Nature* 443(7109):355-358.

80. Weigel AV, Simon B, Tamkun MM, & Krapf D (2011) Ergodic and nonergodic processes coexist in the plasma membrane as observed by single-molecule tracking. *Proceedings of the National Academy of Sciences of the United States of America* 108(16):6438-6443.

81. Mashanov GI, Tacon D, Knight AE, Peckham M, & Molloy JE (2003) Visualizing single molecules inside living cells using total internal reflection fluorescence microscopy. *Methods* 29(2):142-152.

82. Trapani JG, Andalib P, Consiglio JF, & Korn SJ (2006) Control of single channel conductance in the outer vestibule of the Kv2.1 potassium channel. *The Journal of general physiology* 128(2):231-246.

83. Islas LD & Sigworth FJ (1999) Voltage sensitivity and gating charge in Shaker and Shab family potassium channels. *The Journal of general physiology* 114(5):723-742.

84. Stuhmer W*, et al.* (1989) Molecular basis of functional diversity of voltage-gated potassium channels in mammalian brain. *The EMBO journal* 8(11):3235-3244.

85. Pardo LA*, et al.* (1992) Extracellular K+ specifically modulates a rat brain K+ channel. *Proceedings of the National Academy of Sciences of the United States of America* 89(6):2466-2470.

86. Baver SB & O'Connell KM (2012) The C-terminus of neuronal Kv2.1 channels is required for channel localization and targeting but not for NMDA-receptor-mediated regulation of channel function. *Neuroscience*.

87. Honore E*, et al.* (1992) Different types of K+ channel current are generated by different levels of a single mRNA. *The EMBO journal* 11(7):2465-2471.

88. Guillemare E*, et al.* (1992) Effects of the level of mRNA expression on biophysical properties, sensitivity to neurotoxins, and regulation of the brain delayed-rectifier K+ channels Kv1.2. *Biochemistry* 31(49):12463-12468.

89. Fujiwara Y & Kubo Y (2004) Density-dependent changes of the pore properties of the P2X2 receptor channel. *The Journal of physiology* 558(Pt 1):31-43.

90. Coppock EA & Tamkun MM (2001) Differential expression of K(V) channel alpha- and beta-subunits in the bovine pulmonary arterial circulation. *American journal of physiology. Lung cellular and molecular physiology* 281(6):L1350-1360.

91. English AR & Voeltz GK (2013) Endoplasmic reticulum structure and interconnections with other organelles. *Cold Spring Harbor perspectives in biology* 5(4):a013227.

92. Schauder CM*, et al.* (2014) Structure of a lipid-bound extended synaptotagmin indicates a role in lipid transfer. *Nature* 510(7506):552-555.

93. Hogan PG, Lewis RS, & Rao A (2010) Molecular basis of calcium signaling in lymphocytes: STIM and ORAI. *Annual review of immunology* 28:491-533.

94. Fox PD*, et al.* (2013) Plasma membrane domains enriched in cortical endoplasmic reticulum function as membrane protein trafficking hubs. *Molecular biology of the cell* 24(17):2703-2713.

95. Nagy JI, Yamamoto T, & Jordan LM (1993) Evidence for the cholinergic nature of C-terminals associated with subsurface cisterns in alpha-motoneurons of rat. *Synapse* 15(1):17-32.

96. Muennich EA & Fyffe RE (2004) Focal aggregation of voltage-gated, Kv2.1 subunit-containing, potassium channels at synaptic sites in rat spinal motoneurones. *The Journal of physiology* 554(Pt 3):673-685.

97. Fox PD, Loftus RJ, & Tamkun MM (2013) Regulation of Kv2.1 K(+) conductance by cell surface channel density. *The Journal of neuroscience : the official journal of the Society for Neuroscience* 33(3):1259-1270.

98. Kaczmarek LK (2006) Non-conducting functions of voltage-gated ion channels. *Nature reviews. Neuroscience* 7(10):761-771.

99. Press WH, Teukolsky SA, Vetterling WT, & Flannery BP (2007) *Numerical Recipes 3rd Edition: The Art of Scientific Computing* (Cambridge University Press Cambridge, MA).

100. Cardona A*, et al.* (2012) TrakEM2 software for neural circuit reconstruction. *PloS one* 7(6):e38011.

101. Schneider CA, Rasband WS, & Eliceiri KW (2012) NIH Image to ImageJ: 25 years of image analysis. *Nature methods* 9(7):671-675.

102. Carter BC, Shubeita GT, & Gross SP (2005) Tracking single particles: a user-friendly quantitative evaluation. *Physical biology* 2(1):60-72.

103. Antonucci DE, Lim ST, Vassanelli S, & Trimmer JS (2001) Dynamic localization and clustering of dendritic Kv2.1 voltage-dependent potassium channels in developing hippocampal neurons. *Neuroscience* 108(1):69-81.

104. Wang Y*, et al.* (2010) The calcium store sensor, STIM1, reciprocally controls Orai and CaV1.2 channels. *Science* 330(6000):105-109.

105. Orci L*, et al.* (2009) From the Cover: STIM1-induced precortical and cortical subdomains of the endoplasmic reticulum. *Proceedings of the National Academy of Sciences of the United States of America* 106(46):19358-19362.

106. Raffel M, Willert CE, Wereley ST, & J. K (2007) *Particle Image Velocimetry: A Practical Guide.* (Springer Berlin Heidelberg).

107. Liou J, Fivaz M, Inoue T, & Meyer T (2007) Live-cell imaging reveals sequential oligomerization and local plasma membrane targeting of stromal interaction molecule 1 after Ca2+ store depletion. *Proceedings of the National Academy of Sciences of the United States of America* 104(22):9301-9306.

108. Takeshima H, Komazaki S, Nishi M, Iino M, & Kangawa K (2000) Junctophilins: a novel family of junctional membrane complex proteins. *Molecular cell* 6(1):11-22.

109. Park CY, Shcheglovitov A, & Dolmetsch R (2010) The CRAC channel activator STIM1 binds and inhibits L-type voltage-gated calcium channels. *Science* 330(6000):101-105.

110. McMahon HT & Boucrot E (2011) Molecular mechanism and physiological functions of clathrin-mediated endocytosis. *Nature reviews. Molecular cell biology* 12(8):517-533.

111. Jahn R & Sudhof TC (1999) Membrane fusion and exocytosis. *Annual review of biochemistry* 68:863-911.

112. Sudhof TC & Rizo J (2011) Synaptic vesicle exocytosis. *Cold Spring Harbor perspectives in biology* 3(12).

113. Kennedy MJ, Davison IG, Robinson CG, & Ehlers MD (2010) Syntaxin-4 defines a domain for activity-dependent exocytosis in dendritic spines. *Cell* 141(3):524-535.

114. Petrini EM*, et al.* (2009) Endocytic Trafficking and Recycling Maintain a Pool of Mobile Surface AMPA Receptors Required for Synaptic Potentiation. *Neuron* 63(1):92-105.

115. Sudhof TC (2004) The synaptic vesicle cycle. *Annual review of neuroscience* 27:509-547.

116. Ehrlich M*, et al.* (2004) Endocytosis by random initiation and stabilization of clathrin-coated pits. *Cell* 118(5):591-605.

117. Gaidarov I, Santini F, Warren RA, & Keen JH (1999) Spatial control of coated-pit dynamics in living cells. *Nature cell biology* 1(1):1-7.

118. Cao H, Krueger EW, & McNiven MA (2011) Hepatocytes internalize trophic receptors at large endocytic "Hot Spots". *Hepatology* 54(5):1819-1829.

119. Saffarian S, Cocucci E, & Kirchhausen T (2009) Distinct dynamics of endocytic clathrin-coated pits and coated plaques. *PLoS biology* 7(9):e1000191.

120. Nunez D*, et al.* (2011) Hotspots organize clathrin-mediated endocytosis by efficient recruitment and retention of nucleating resources. *Traffic* 12(12):1868-1878.

121. Rappoport JZ, Kemal S, Benmerah A, & Simon SM (2006) Dynamics of clathrin and adaptor proteins during endocytosis. *American journal of physiology. Cell physiology* 291(5):C1072-1081.

122. Bellve KD*, et al.* (2006) Plasma membrane domains specialized for clathrin-mediated endocytosis in primary cells. *The Journal of biological chemistry* 281(23):16139-16146.

123. Keller P, Toomre D, Diaz E, White J, & Simons K (2001) Multicolour imaging of post-Golgi sorting and trafficking in live cells. *Nature cell biology* 3(2):140-149.

124. Toomre D, Steyer JA, Keller P, Almers W, & Simons K (2000) Fusion of constitutive membrane traffic with the cell surface observed by evanescent wave microscopy. *The Journal of cell biology* 149(1):33-40.

125. Wick PF, Trenkle JM, & Holz RW (1997) Punctate appearance of dopamine-beta-hydroxylase on the chromaffin cell surface reflects the fusion of individual chromaffin granules upon exocytosis. *Neuroscience* 80(3):847-860.

126. Robinson IM, Yamada M, Carrion-Vazquez M, Lennon VA, & Fernandez JM (1996) Specialized release zones in chromaffin cells examined with pulsed-laser imaging. *Cell calcium* 20(2):181-201.

127. Robinson IM, Finnegan JM, Monck JR, Wightman RM, & Fernandez JM (1995) Colocalization of calcium entry and exocytotic release sites in adrenal chromaffin cells. *Proceedings of the National Academy of Sciences of the United States of America* 92(7):2474-2478.

128. Schroeder TJ, Jankowski JA, Senyshyn J, Holz RW, & Wightman RM (1994) Zones of exocytotic release on bovine adrenal medullary cells in culture. *The Journal of biological chemistry* 269(25):17215-17220.

129. Stenkula KG, Lizunov VA, Cushman SW, & Zimmerberg J (2010) Insulin controls the spatial distribution of GLUT4 on the cell surface through regulation of its postfusion dispersal. *Cell metabolism* 12(3):250-259.

130. Chivers CE*, et al.* (2010) A streptavidin variant with slower biotin dissociation and increased mechanostability. *Nature methods*:1-6.

131. Howarth M*, et al.* (2006) A monovalent streptavidin with a single femtomolar biotin binding site. *Nature methods* 3(4):267-273.

132. Jaiswal JK & Simon SM (2004) Potentials and pitfalls of fluorescent quantum dots for biological imaging. *Trends in Cell Biology* 14(9):497-504.

133. Jaiswal JK, Goldman ER, Mattoussi H, & Simon SM (2004) Use of quantum dots for live cell imaging. *Nature methods* 1(1):73-78.

134. Sergé AB, Nicolas; Rigneault, Hervé; and Marguet, Didier (2008) Multiple-target tracing (MTT) algorithm probes molecular dynamics at cell surface. *Protocol Exchange*.

135. Serge A, Bertaux N, Rigneault H, & Marguet D (2008) Dynamic multiple-target tracing to probe spatiotemporal cartography of cell membranes. *Nature methods* 5(8):687-694.

136. Barlow AL, Macleod A, Noppen S, Sanderson J, & Guerin CJ (2010) Colocalization analysis in fluorescence micrographs: verification of a more accurate calculation of pearson's correlation coefficient. *Microscopy and microanalysis : the official journal of Microscopy Society of America, Microbeam Analysis Society, Microscopical Society of Canada* 16(6):710-724.

137. Miesenbock G, De Angelis DA, & Rothman JE (1998) Visualizing secretion and synaptic transmission with pH-sensitive green fluorescent proteins. *Nature* 394(6689):192-195.

138. Russ JC (2007) *The Image Processing Handbook Fifth Edition* (CRC Press, Boca Raton, FL).

139. Jaqaman K*, et al.* (2008) Robust single-particle tracking in live-cell time-lapse sequences. *Nature methods* 5(8):695-702.

140. Motley A, Bright NA, Seaman MN, & Robinson MS (2003) Clathrin-mediated endocytosis in AP-2-depleted cells. *The Journal of cell biology* 162(5):909-918.

141. Jing SQ, Spencer T, Miller K, Hopkins C, & Trowbridge IS (1990) Role of the human transferrin receptor cytoplasmic domain in endocytosis: localization of a specific signal sequence for internalization. *The Journal of cell biology* 110(2):283-294.

142. Hopkins CR (1985) The appearance and internalization of transferrin receptors at the margins of spreading human tumor cells. *Cell* 40(1):199-208.

143. Loerke D*, et al.* (2009) Cargo and dynamin regulate clathrin-coated pit maturation. *PLoS biology* 7(3):e57.

144. Mettlen M, Loerke D, Yarar D, Danuser G, & Schmid SL (2010) Cargo- and adaptor-specific mechanisms regulate clathrin-mediated endocytosis. *The Journal of cell biology* 188(6):919-933.

145. Miller K, Shipman M, Trowbridge IS, & Hopkins CR (1991) Transferrin receptors promote the formation of clathrin lattices. *Cell* 65(4):621-632.

146. Liou J*, et al.* (2005) STIM is a Ca2+ sensor essential for Ca2+-store-depletion-triggered Ca2+ influx. *Current biology : CB* 15(13):1235-1241.

147. Stradalova V*, et al.* (2012) Distribution of cortical endoplasmic reticulum determines positioning of endocytic events in yeast plasma membrane. *PloS one* 7(4):e35132.

148. Waterman-Storer CM & Salmon ED (1998) Endoplasmic reticulum membrane tubules are distributed by microtubules in living cells using three distinct mechanisms. *Current biology : CB* 8(14):798-806.

149. Klopfenstein DR, Kappeler F, & Hauri HP (1998) A novel direct interaction of endoplasmic reticulum with microtubules. *The EMBO journal* 17(21):6168-6177.

150. Terasaki M, Chen LB, & Fujiwara K (1986) Microtubules and the endoplasmic reticulum are highly interdependent structures. *The Journal of cell biology* 103(4):1557-1568.

151. Marchaland J*, et al.* (2008) Fast subplasma membrane Ca2+ transients control exo-endocytosis of synaptic-like microvesicles in astrocytes. *The Journal of neuroscience : the official journal of the Society for Neuroscience* 28(37):9122-9132.

152. Orci L, Gabbay KH, & Malaisse WJ (1972) Pancreatic beta-cell web: its possible role in insulin secretion. *Science* 175(4026):1128-1130.

153. Tavassoli S*, et al.* (2013) Plasma membrane--endoplasmic reticulum contact sites regulate phosphatidylcholine synthesis. *EMBO reports* 14(5):434-440.

154. Stefan CJ*, et al.* (2011) Osh proteins regulate phosphoinositide metabolism at ER-plasma membrane contact sites. *Cell* 144(3):389-401.

155. Manford AG, Stefan CJ, Yuan HL, Macgurn JA, & Emr SD (2012) ER-to-plasma membrane tethering proteins regulate cell signaling and ER morphology. *Developmental cell* 23(6):1129-1140.